Submerged Photo-synthesis of ZnO Nanorods and their Opto-electrical Properties

Zn0 ナノロッドの水中結晶光合成と光・電子特性

Melbert Jeem

Hokkaido University

September 2017

TABLE OF CONTENTS

CHAPTER 1

General Introduction

1.1 Nanomaterials

Nanomaterials are defined scientifically as the materials whose structural elements, e.g., clusters, crystallites, or molecules, have one of the dimensions in range of 1 to 100 nm. For the past decades, nanomaterials have greatly attracted attention and developed for interdisciplinary fields, beneficial for nanoscience and nanotechnology.[1] The flourishing application of these materials both in academic and industries are due to their astounding variations in corresponding characteristics. Here, nanomaterials can be constructed from zero-dimensional (0-D) nanoparticles to three-dimensional (3-D) hierarchical nanostructures through variety of synthesis approaches. In particular, nanomaterials with controlled size and shape are important because their electrical, optical, and magnetic properties depend strongly on their size and shape.[2] Focusing on the synthesis approaches, this chapter will highlight and introduce zinc oxide (ZnO) nanomaterials as one of attractive semiconductor materials.

1.2 ZnO nanomaterials

1.2.1 Introduction

Zinc oxide (ZnO) nanomaterials has attracted many interest due to their well-known performance in optics and electronics. In fact, synthesis of ZnO nanostructures has been an active field since the 1960s, which their applications as sensors, transducers, and catalysts have been studied by many researchers. In the last few decades, the study of one-dimensional (1D) materials has become a leading edge in science and technology. The materials size reduction introduced novel electrical, mechanical, chemical and opto-electrical properties as a result of surface and quantum confinement effects.

Nanowire or nanorod-like structures are the ideal system for studying those effects in 1D confined object. On the other hand, ZnO is a key technological material. It is a wide bandgap (3.37 eV) semiconductor that is suitable for short wavelength opto-electronic applications. In addition, the high exciton binding energy (60 meV) in ZnO crystal can ensure efficient excitonic emission at room temperature or room temperature ultraviolet (UV) emission. Futhermore, ZnO is a versatile functional material that its nanosize morphology can be tuned into nanobelts,[3] nanocages,[4] nanocombs,[5] nanorings,[6] nanohelix,[7, 8] and nanosprings.[6]

1.2.2 1-D to 3-D nanostructures

One-dimensional (1-D) metal oxides nanostructures such as nanorods, nanowires, and nanotubes being ordered to functional network and oriented 3-D periodic arrays are in high demand. This is due to as many techniques are available to produce metal oxide 1D nanostructures but only a few of them can generate anisotropic 1D nanomaterials assembled as 3D arrays.

The goal of generating 3D arrays is to develop practical devices such as chemical, gas, and bio-sensors[9] as well as opto-electronic devices, such as lasers,[10-12] photodetectors,[13-16] optical switches,[17, 18] photovoltaics,[19-21] and photo-catalytic cells.[22, 23] Besides ZnO, together with TiO_2, they are by far the most representative 1D nano-materials produced to date due to their established importance as underlying materials for catalysis and large bandgap semiconducting properties. Table 1.1 summarizes the dimensions, synthesis techniques, and type of oriented arrays of 1D nanostructures that have been produced so far.

Table 1.1 – Oriented 3D arrays consisting of 1D TiO_2 and ZnO nanostructures.

Material	Morphology	Dimension (D*L)	Synthetic method	Reference
TiO_2	Nanowire	10-40 nm * 2-10 µm	Electrodeposition in alumina membrane	24
		15 nm * 6 µm	Alumina membrane	25
	Nanorod	40-50 nm * 140 nm	Photoelectrochemical etching	26
	Nanowire	125-200 nm * 10 µm	Sol-gel electrophoresis in	27

			polycarbonate membrane	
		200 nm * 2 μm 500 nm * 8 μm	Magnetron sputtering	28
		15 nm * 30 μm	Alumina membrane	29
	Nanotube	2.5-5 nm inner diameter 20-40 nm outer diameter 0.3-0.9 μm in length		30
		200 nm outer diameter 50 μm in length		31
		25–60 nm inner diameter 250 nm in length	Anodic oxidation	32
		50–70 nm inner diameter 120 nm outer diameter Several μm in length	Electrodeposition in polymer-coated alumina membrane	33
		170–180 nm inner diameter 200–233 nm outer diameter 3 μm in length	Alumina membrane	34
ZnO	Nanowire	15-40 nm * 1 μm	Molecular beam epitaxy	35
	Nanorod	20 nm * 400 nm	Pulsed laser deposition	36
		25 nm * 800 nm	Metallorganic vapor-phase epitaxy	37
		45 nm * 200 nm 70 nm * 600 nm	Chemical vapor deposition	38, 39
		85-95 nm * 500 nm	Epitaxial electrodeposition	40
	Nanowire	55 nm * 2.6 μm 190 nm * 15 μm	Metal vapor deposition	41
		90 nm * 1 μm	Electrodeposition in alumina membrane	42
		150-250 nm * 2 μm	Electrodeposition	43
		100-200 nm several μm in length	Aqueous chemical growth	44
		10-200 nm * 2-20 μm	Vapor-liquid-solid growth	45, 46

		20-120 nm * 5-20 μm		
		15-90 nm * few μm	Alumina membrane	47
		200 nm * 50 μm		29
	Nanotube	150 nm inner diameter 200 nm outer diameter 60 μm in length		48
	Microtube	1 μm inner diameter 1 μm outer diameter 1 μm in length	Aqueous chemical growth	49

1.2.3 Crystal structure and polar surfaces of ZnO

ZnO has a hexagonal structure (space group *P63mc*) with lattice parameters a = 3.25 Å and c = 5.12 Å. The structure of ZnO can be simply described as a number of alternating planes composed of tetrahedrally coordinated O^{2-} and Zn^{2+} ions, stacked alternatively along the c-axis. The tetrahedral coordination in ZnO results in non-central symmetric structure and piezoelectricity. Another important characteristic of ZnO is the polar surfaces. The most common polar surface is the basal plane. The oppositely charged ions produce positively charged Zn-(0001) and negatively charged O-$(000\bar{1})$ polar surfaces (Figure 1.1b), resulting in a normal dipole moment and spontaneous polarization

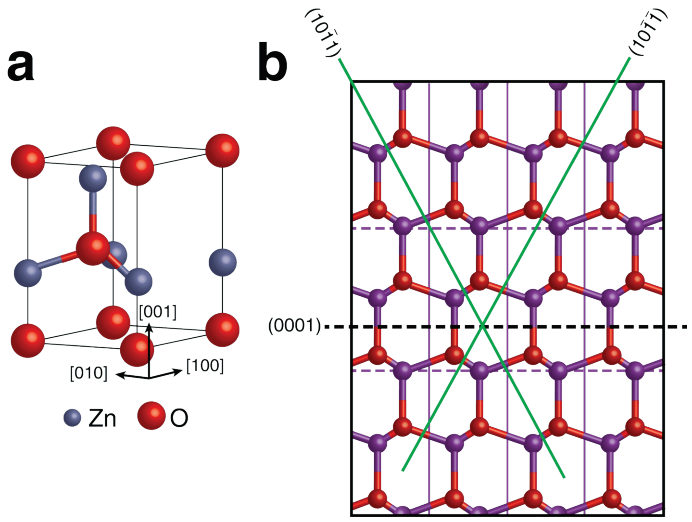

Figure 1.1 – (a) Wurtzite structure model of ZnO. The tetrahedral coordination of ZnO is shown. (b) The structure model of ZnO projected along $[2\bar{1}\bar{1}0]$, displaying the ±(0001), ±$(10\bar{1}\bar{1})$ and ±$(10\bar{1}\bar{1})$ polar surfaces [Ref. 50].

along the c-axis. Another polar surface is the $\{01\bar{1}1\}$. By projecting the structure along $[2\bar{1}\bar{1}0]$, as shown in Figure 1.1b, beside the most typical ±(0001) polar surfaces that are terminated with Zn and oxygen, respectively, $\pm(10\bar{1}\bar{1})$ and $\pm(10\bar{1}1)$ are also polar surfaces. The $\{01\bar{1}1\}$ type surfaces are not common for ZnO, but they have been observed in a nanohelical structure.[7] The charges on the polar surfaces are ionic charges, which are non-transferable and non-flowable. Because the interaction energy among the charges depends on the distribution of the charges, the structure is arranged in such a configuration to minimize the electrostatic energy. This is the main driving force for growing the polar surface dominated nanostructures.

1.2.4 ZnO optical properties

The optical properties of ZnO are heavily influenced by the energy band structure and lattice dynamics. Photoluminescence and cathodoluminescence methods are two common approaches being utilized to investigate the ZnO optical properties, which is known driven by excitonic recombinations in the crystal lattice. The obtained excitonic spectra can be assigned to many defects related spectral features, as well as donor-acceptor pair (DAP) emission.

A broad defect related peak extending from ~1.9 eV to ~2.8 eV is also a common feature of ZnO. Known as the green band, the origin of its luminescence is still not well understood and has in the past been attributed to a variety of different impurities and defects. In terms of the more fundamental optical properties of ZnO, there have been a number of comprehensive studies to determine the refractive index and dielectric constants of this material.[51-53] The measurements were all carried out using spectroscopic

Table 1.2 – Static (ϵ_0) and high frequency dielectric constant (ϵ_∞) data for ZnO.[51, 52]

		Film[52]	Bulk[52]	Bulk[51]
ϵ_0	E⊥*c*	7.46	7.77	
	E∥*c*	8.59	8.91	
ϵ_∞	E⊥*c*	3.7	3.6	3.68
	E∥*c*	3.78	3.66	3.72

ellipsometry. The values determined for the dielectric constants of ZnO area shown in Table 1.2. The refractive index of wurtzite ZnO is commonly given as $n_w = 2.008$ and $n_e = 2.029$.[54]

1.2.5 ZnO electrical properties

The electrical properties of ZnO are hard to quantify due to large variance of the quality of samples available. The background carrier concentration varies a lot according to the quality of the layers but is usually ~10^{16} cm^{-3}. The largest reported *n*-type doping is ~10^{20} electrons cm^{-3} and largest reported *p*-type doping is ~10^{19} holes cm^{-3}. However, such high levels of p-conductivity are questionable and have not been experimentally verified.[55] The exciton binding energy is 60 meV at 300 K, and is one of the reasons why ZnO is so attractive for opto-electronic devices applications.

1.2.6 Conventional growth mechanism

ZnO is an amphoteric oxide with an isoelectric point value of about 95.[56] In general, ZnO will crystallize by the hydrolysis of Zn salts in a basic solution that can be formed using strong or weak alkalis. This process is generally known to occur as hydrothermal reactions. The common used alkali compound for this reactions are KOH and NaOH.

Zn^{2+} is known to coordinate in tetrahedral complexes. Depending on the given pH

and temperature,[57] Zn^{2+} is able to exist in a series of intermediates, and ZnO can be formed by the dehydration of these intermediates:[58, 59]

$$Zn^{2+} + 2OH^- \leftrightarrow Zn(OH)_2 \quad (1.1)$$

$$Zn(OH)_2 + 2OH^- \leftrightarrow [Zn(OH)_4]^{2-} \quad (1.2)$$

$$[Zn(OH)_4]^{2-} \leftrightarrow ZnO_2^{2-} + 2H_2O \quad (1.3)$$

$$ZnO_2^{2-} + H_2O \leftrightarrow ZnO + 2OH^- \quad (1.4)$$

An alkaline solution is essential because normally divalent ions do not hydrolyze in acidic environments.[60-62] As the concentration and temperature of alkaline solution increase, ZnO solubility also will increase. In this manner, the actual scenario of ZnO formation is more complicated than as described in equations (1.1)-(1.4). For example, oxygen molecules have not been considered at all, but in reality, dissolved O_2 concentration in the solution plays a significant role for final ZnO crystal.

1.3 Light-assisted ZnO nanostructures fabrication

1.3.1 Effect of light irradiation

As been mentioned in section 1.2.5, ZnO has a direct bandgap of 3.37 eV and exciton binding energy of 60 meV at room temperature. These properties are useful for the development of many opto-electronic devices. In particular, ZnO has a very sharp photoluminescence emission peaks at near band edge energy of 3.37 eV due to the

excitonic radiative recombination processes. This is usually achieved by ultraviolet light illumination on ZnO, where pair of free electrons and holes are created. The 60 meV exciton binding energy gives the stability against thermal dissociation of exciton (26 meV) at room temperature.

This means that there is a significant advantage to operate excitonic light action at room temperature. To further lower this threshold energy than 60 meV, fabrication of nanoscale size of ZnO is essential. Then, quantum size effects will give rise to substantial density of states at the band edges and enhance radiative recombination due to carrier concentration. Another particular photoluminescence emission of ZnO can be observed through broad peak at visible light region, where yellow emission at 600 nm highest peak is usually related to defect in ZnO crystal lattice. Evaluation of ZnO nanostructure formation through those two perspectives will be discussed in the next section.

1.3.2 Mechanism

It is known that ZnO nanostructures grown by the solution method present a large number of defects, i.e., oxygen vacancies, oxygen interstitials, Zn vacancies, and Zn interstitials.[63-65] In the case of broad yellow photoluminescence spectrum, the emission is attributed to oxygen vacancies.[66-68] Formation of $Zn(OH)_2$ in equation (1.1) gives the oxygen vacancy state. Conventional hydrothermal reactions principal explain that

$Zn(OH)_2$ dehydrate to form ZnO and finally reduce the oxygen vacancy. In the case of light-assisted formation, when ultraviolet light interacts with $Zn(OH)_2$, it causes promotion of electron from ground state to a high-energy state. $Zn(OH)_2$ further dissociates into Zn^{2+} and OH^- ions by UV-assisted thermal decomposition to form ZnO and water (equation 1.5).[63]

$$Zn^{2+} + 2OH^- \rightarrow ZnO + H_2O \quad (1.5)$$

Then, H_2O in equation (1.5) will dissociate again and adsorbed onto oxygen bridging vacancies to form $[Zn(OH)_4]^{2-}$ and ZnO_2^{2-}. Finally, reduction of water molecules will reduce the concentration of oxygen defects. Oxygen defects act as non-radiative center to suppress the band-edge emission of ZnO.[69] The lower the concentration of oxygen defects, the better enhancement of ZnO band edge emission.

1.4 Problem

Now we have grasped the understanding in ZnO formation mechanism through hydrothermal reactions and light irradiation scenario. Both conclude that alkaline solution is essential for ZnO formation and lattice defects are responsible for ZnO opto-electrical properties. However, there is no framework that has been dedicated to study the ZnO formation starting from UV irradiation in pure, neutral water. Further, there is no concrete data showing local crystal lattice defects influencing the changing opto-electrical

properties and subsequently the ZnO morphology.

1.5 Objective

Based on the given problems, this thesis will focus on facile fabrication of ZnO nanocrystallites using UV irradiation in a pure, neutral water. Further, by detection and study in their local crystal defects, the nanocrystallites formation mechanism and evaluation of their opto-electrical properties will be explained.

1.6 Dissertation organization

Chapter 1 gives a brief introduction of TiO_2 and ZnO in their 1-D to 3-D nanomaterials processing. Here, the fundamental of this thesis is established. The potential of ZnO nanocrystallites in opto-electronic devices application is discussed. Conventional formation mechanism regards crystals defect in alkaline solution influencing the morphology change of ZnO nanocrystallites. The issue is no framework have been dedicated to study local crystal defects occurred by light irradiation in pure, neutral water. Thus, the objective of the thesis is to implement light irradiation effect to ZnO nanocrystallites formation and study their opto-electrical properties.

Chapter 2 introduces submerged liquid plasma as a facile method to fabricate crystal seeds (nanobumps), which are the localized oxide nanoparticles on a metal plate surface. The target material is set as cathode, while a platinum wire bended into mesh is

set as anode. There are two types of plasma discharge: glow-discharge and arc-discharge. The initiation control of both is essential in order to get the nanobumps surface and preventing the electrode from getting burned. A typical voltage and current ranges during glow-discharge on a Zn plate is 130 – 140 V and 1.9 – 2.0 A, respectively. Nanobumps are the nanosized metal oxide (ZnO) particles. Their transformation in construction of nanocrystallites later is a proof that we could take advantage of their modified band energy structure. This is highlighted in photochemical reactions when we implemented an ultraviolet (UV, λ = 365 nm) irradiation on the nanobumps.

Chapter 3 introduces the production of ZnO nanorods forming into nanoflowers and dendrites by using submerged photosynthesis (SPSC) technique. Other than ZnO, SPSC technique also can be utilized to fabricate CuO nanoflowers, CeO_2 dendrites, and WO_3 nanorods. In particular, the ZnO nanorods are shown to grow at the protruded surfaces (nanobumps) when illuminated by ultraviolet (UV, λ = 365 nm) in pure, neutral water. The process is photocatalytic, with hydroxyl radical via water splitting and hydrogen gas were detected. *Ab initio* calculation was conducted to verify high electron density at nanobumps surfaces. This is essential to enable water splitting occurrence at low dissociation energy.

Chapter 4 highlights the apical characteristic control on ZnO nanorods, which

evolves from tapered to capped shape after continuous 72h UV irradiation. Then, the capped shape will reconstruct again into tapered shape after UV re-irradiation in fresh ultrapure water. In this morphology control, crystal defects change in ZnO nanorods need to be investigated. They are key factors for indirect, interband transitions of ZnO opto-electronic devices in visible light range. Taking their high energy and spatial resolution, using photoluminescence analysis and valance electron energy-loss spectroscopy in scanning transmission electron microscopy (STEM-VEELS), oxygen vacancy point defects are detected on the tip-edge of a tapered nanorod. They serve as an opto-electrical hotspot for the light-driven formation and tunability of the opto-electrical properties. A double increase of electron energy absorption on near band edge energy of ZnO was observed near the tip-edge of tapered nanorod.

Chapter 5 concludes with lessons learned in this thesis. Additional future work is presented: nanorods patterning, optical properties study by cathodoluminescence, and antimicrobial effects by CuO nanoflowers. While advances in this thesis have opened new perspective of transition metal oxide crystallites fabrication using SPSC, there is still much more to learn in these fields.

References

[1] D. R. Baer, P. E. Burrows, A. A. El-Azab, Enhancing coating functionality using nanoscience and nanotechnology. *Progress in Organic Coatings* **47** (2003) 342-356.

[2] D. Yu, V. W.-W. Yam, Controlled synthesis of monodisperse silver nanocubes in water. *Journal of the American Chemical Society* **126** (2004) 13200-13201.

[3] Z. W. Pan, Z. R. Dai, Z. L. Wang, Nanobelts of semiconducting oxides. *Science* **291** (2001) 1947-1949.

[4] P. X. Gao, Z. L. Wang, Mesoporous polyhedral cages and shells formed by textured self-assembly of ZnO nanocrystals. *Journal of the American Chemical Society* **125** (2003) 11299-11305.

[5] Z. L. Wang, X. Y. Kong, J. M. Zuo, Induced growth of asymmetric nanocantilever arrays on polar surfaces. *Physical Review Letters* **91** (2003) 185502.

[6] X. Y. Kong, Y. Ding, R. Yang, Z. L. Wang, Single-crystal nanorings formed by epitaxial self-coiling of polar nanobelts. *Science* **303** (2004) 1348-1351.

[7] R. Yang, Y. Ding, Z. L. Wang, Deformation-free single-crystal nanohelixes of polar nanowires. *Nano Letters* **4** (2004) 1309-1312.

[8] P. X. Gao, Y. Ding, W. Mai, W. L. Hughes, C. Lao, Z. L. Wang, Conversion of zinc oxide nanobelts into superlattice-structured nanohelices. *Science* **309** (2005) 1700-1704.

[9] N. Karimian, L. Moretto, P. Ugo, Nanobiosensing with arrays and ensembles of nanoelectrodes. *Sensors (Basel)* **17** (2017) 65.

[10] J. Yeo, S. Hong, M. Wanit, H. W. Kang, D. Lee, C. P. Grigoropoulos, H. J. Sung, S. H. Ko, Rapid, one-step, digital selective growth of ZnO nanowires on 3d structures using laser induced hydrothermal growth. *Advanced Functional Materials* **23** (2013) 3316-3323.

[11] J. Y. Suh, C. H. Kim, W. Zhou, M. D. Huntington, D. T. Co, M. R. Wasielewski, T. W. Odom, Plasmonic bowtie nanolaser arrays. *Nano Letters* **12** (2012) 5769-5774.

[12] A. N. Giakoumaki, G. Kenanakis, A. Klini, M. Androulidaki, Z. Viskadourakis, M. Farsari, A. Selimis, 3d micro-structured arrays of znomicron nanorods. *Scientific Reports* **7** (2017) 2100.

[13] X. Chen, S. Pan, P. J. Feng, H. Bian, X. Han, J. H. Liu, X. Guo, D. Chen, H. Ge, Q. D. Shen, Bioinspired ferroelectric polymer arrays as photodetectors with signal transmissible to neuron cells. *Advanced Materials* **28** (2016) 10684-10691.

[14] P. Senanayake, C. H. Hung, A. Farrell, D. A. Ramirez, J. Shapiro, C. K. Li, Y. R. Wu, M. M. Hayat, D. L. Huffaker, Thin 3d multiplication regions in plasmonically enhanced nanopillar avalanche detectors. *Nano Letters* **12** (2012) 6448-6452.

[15] J. Lu, H. Liu, M. Zheng, H. Zhang, S. X. Lim, E. S. Tok, C. H. Sow, Laser modified ZnO/cdsse core-shell nanowire arrays for micro-steganography and improved photoconduction. *Scientific Reports* **4** (2014) 6350.

[16] J. F. Song, X. S. Luo, X. G. Tu, L. X. Jia, Q. Fang, T. Y. Liow, M. B. Yu, G. Q. Lo, Three-dimensional (3d) monolithically integrated photodetector and wdm receiver based on bulk silicon wafer. *Optics*

Express **22** (2014).

[17] T. Yamamoto, J. Yamaguchi, N. Takeuchi, A. Shimizu, R. Sawada, E. Higurashi, Y. Uenishi, A three-dimensional micro-electro-mechanical system (mems) optical switch module using low-cost highly accurate polymer components. *Japanese Journal of Applied Physics Part 1-Regular Papers Brief Communications & Review Papers* **43** (2004) 5824-5827.

[18] R. Dehmel, A. Nicolas, M. R. J. Scherer, U. Steiner, 3d nanostructured conjugated polymers for optical applications. *Advanced Functional Materials* **25** (2015) 6900-6905.

[19] Y. Yu, J. Li, D. Geng, J. Wang, L. Zhang, T. L. Andrew, M. S. Arnold, X. Wang, Development of lead iodide perovskite solar cells using three-dimensional titanium dioxide nanowire architectures. *ACS Nano* **9** (2015) 564-572.

[20] J. Shi, Y. Hara, C. Sun, M. A. Anderson, X. Wang, Three-dimensional high-density hierarchical nanowire architecture for high-performance photoelectrochemical electrodes. *Nano Letters* **11** (2011) 3413-3419.

[21] K. J. Williams, W. A. Tisdale, K. S. Leschkies, G. Haugstad, D. J. Norris, E. S. Aydil, X. Y. Zhu, Strong electronic coupling in two-dimensional assemblies of colloidal pbse quantum dots. *ACS Nano* **3** (2009) 1532-1538.

[22] S. Sadhu, P. Gupta, P. Poddar, Physical mechanism behind enhanced photoelectrochemical and photocatalytic properties of superhydrophilic assemblies of 3d-TiO2 microspheres with arrays of oriented, single-crystalline TiO2 nanowires as building blocks deposited on fluorine-doped tin oxide. *ACS Appl Mater Interfaces* **9** (2017) 11202-11211.

[23] S. Farsinezhad, S. P. Banerjee, B. Bangalore Rajeeva, B. D. Wiltshire, H. Sharma, A. Sura, A. Mohammadpour, P. Kar, R. Fedosejevs, K. Shankar, Reduced ensemble plasmon line widths and enhanced two-photon luminescence in anodically formed high surface area au-TiO2 3d nanocomposites. *ACS Appl Mater Interfaces* **9** (2017) 740-749.

[24] Z. Miao, D. Xu, J. Ouyang, G. Guo, X. Zhao, Y. Tang, Electrochemically induced sol−gel preparation of single-crystalline TiO_2 nanowires. *Nano Letters* **2** (2002) 717-720.

[25] X. Y. Zhang, L. D. Zhang, W. Chen, G. W. Meng, M. J. Zheng, L. X. Zhao, F. Phillipp, Electrochemical fabrication of highly ordered semiconductor and metallic nanowire arrays. *Chemistry of Materials* **13** (2001) 2511-2515.

[26] H. Masuda, K. Kanezawa, M. Nakao, A. Yokoo, T. Tamamura, T. Sugiura, H. Minoura, K. Nishio, Ordered arrays of nanopillars formed by photoelectrochemical etching on directly imprinted TiO_2 single crystals. *Advanced Materials* **15** (2003) 159-161.

[27] S. J. Limmer, S. Seraji, Y. Wu, T. P. Chou, C. Nguyen, G. Z. Cao, Template-based growth of various oxide nanorods by sol–gel electrophoresis. *Advanced Functional Materials* **12** (2002) 59-64.

[28] J. Rodríguez, M. Gómez, J. Lu, E. Olsson, C. G. Granqvist, Reactively sputter-deposited titanium oxide coatings with parallel penniform microstructure. *Advanced Materials* **12** (2000) 341-343.

[29] B. B. Lakshmi, P. K. Dorhout, C. R. Martin, Sol−gel template synthesis of semiconductor nanostructures. *Chemistry of Materials* **9** (1997) 857-862.

[30] S. M. Liu, L. M. Gan, L. H. Liu, W. D. Zhang, H. C. Zeng, Synthesis of single-crystalline TiO_2 nanotubes. *Chemistry of Materials* **14** (2002) 1391-1397.

[31] P. Hoyer, Formation of a titanium dioxide nanotube array. *Langmuir* **12** (1996) 1411-1413.

[32] S.-Z. Chu, K. Wada, S. Inoue, S.-i. Todoroki, Synthesis and characterization of titania nanostructures on glass by al anodization and sol−gel process. *Chemistry of Materials* **14** (2002) 266-272.

[33] J. Bao, C. Tie, Z. Xu, Q. Ma, J. Hong, H. Sang, D. Sheng, An array of concentric composite nanostructures of zirconia nanotubules/cobalt nanowires: Preparation and magnetic properties. *Advanced Materials* **14** (2002) 44-47.

[34] J. Bao, D. Xu, Q. Zhou, Z. Xu, Y. Feng, Y. Zhou, An array of concentric composite nanostructure of metal nanowires encapsulated in zirconia nanotubes: Preparation, characterization, and magnetic properties. *Chemistry of Materials* **14** (2002) 4709-4713.

[35] Y. W. Heo, V. Varadarajan, M. Kaufman, K. Kim, D. P. Norton, F. Ren, P. H. Fleming, Site-specific growth of ZnO nanorods using catalysis-driven molecular-beam epitaxy. *Applied Physics Letters* **81** (2002) 3046-3048.

[36] S. V. Prasad, S. D. Walck, J. S. Zabinski, Microstructural evolution in lubricious ZnO films grown by pulsed laser deposition. *Thin Solid Films* **360** (2000) 107-117.

[37] W. I. Park, D. H. Kim, S.-W. Jung, G.-C. Yi, Metalorganic vapor-phase epitaxial growth of vertically well-aligned ZnO nanorods. *Applied Physics Letters* **80** (2002) 4232-4234.

[38] S.-C. Liu, J.-J. Wu, Low-temperature and catalyst-free synthesis of well-aligned ZnO nanorods on si (100). *Journal of Materials Chemistry* **12** (2002) 3125-3129.

[39] J.-J. Wu, S.-C. Liu, Low-temperature growth of well-aligned ZnO nanorods by chemical vapor deposition. *Advanced Materials* **14** (2002) 215-218.

[40] R. Liu, A. A. Vertegel, E. W. Bohannan, T. A. Sorenson, J. A. Switzer, Epitaxial electrodeposition of zinc oxide nanopillars on single-crystal gold. *Chemistry of Materials* **13** (2001) 508-512.

[41] S. C. Lyu, Y. Zhang, H. Ruh, H.-J. Lee, H.-W. Shim, E.-K. Suh, C. J. Lee, Low temperature growth and photoluminescence of well-aligned zinc oxide nanowires. *Chemical Physics Letters* **363** (2002) 134-138.

[42] M. J. Zheng, L. D. Zhang, G. H. Li, W. Z. Shen, Fabrication and optical properties of large-scale uniform zinc oxide nanowire arrays by one-step electrochemical deposition technique. *Chemical Physics Letters* **363** (2002) 123-128.

[43] L. Dloczik, R. Engelhardt, K. Ernst, S. Fiechter, I. Sieber, R. Könenkamp, Hexagonal nanotubes of ZnS by chemical conversion of monocrystalline ZnO columns. *Applied Physics Letters* **78** (2001) 3687-3689.

[44] L. Vayssieres, Growth of arrayed nanorods and nanowires of ZnO from aqueous solutions. *Advanced*

Materials **15** (2003) 464-466.

[45] Y. Wu, H. Yan, P. Yang, Semiconductor nanowire array: Potential substrates for photocatalysis and photovoltaics. *Topics in Catalysis* **19** (2002) 197-202.

[46] P. Yang, H. Yan, S. Mao, R. Russo, J. Johnson, R. Saykally, N. Morris, J. Pham, R. He, H. J. Choi, Controlled growth of ZnO nanowires and their optical properties. *Advanced Functional Materials* **12** (2002) 323-331.

[47] Y. Li, G. W. Meng, L. D. Zhang, F. Phillipp, Ordered semiconductor ZnO nanowire arrays and their photoluminescence properties. *Applied Physics Letters* **76** (2000) 2011-2013.

[48] Z. Wang, H. L. Li, Highly ordered zinc oxide nanotubules synthesized within the anodic aluminum oxide template. *Applied Physics A* **74** (2002) 201-203.

[49] L. Vayssieres, K. Keis, A. Hagfeldt, S.-E. Lindquist, Three-dimensional array of highly oriented crystalline ZnO microtubes. *Chemistry of Materials* **13** (2001) 4395-4398.

[50] Z. L. Wang, Chapter 10 - novel nanostructures and nanodevices of ZnO. In *Zinc oxide bulk, thin films and nanostructures*. (Elsevier Science Ltd, Oxford, 2006), pp. 339-370.

[51] H. Yoshikawa, S. Adachi, Optical constants of ZnO. *Japanese Journal of Applied Physics Part 1-Regular Papers Short Notes & Review Papers* **36** (1997) 6237-6243.

[52] N. Ashkenov, B. N. Mbenkum, C. Bundesmann, V. Riede, M. Lorenz, D. Spemann, E. M. Kaidashev, A. Kasic, M. Schubert, M. Grundmann, G. Wagner, H. Neumann, V. Darakchieva, H. Arwin, B. Monemar, Infrared dielectric functions and phonon modes of high-quality ZnO films. *Journal of Applied Physics* **93** (2003) 126-133.

[53] X. W. Sun, H. S. Kwok, Optical properties of epitaxially grown zinc oxide films on sapphire by pulsed laser deposition. *Journal of Applied Physics* **86** (1999) 408-411.

[54] S. J. Pearton, D. P. Norton, K. Ip, Y. W. Heo, T. Steiner, Recent progress in processing and properties of ZnO. *Progress in Materials Science* **50** (2005) 293-340.

[55] D. C. Look, B. Claflin, Y. I. Alivov, S. J. Park, The future of ZnO light emitters. *physica status solidi (a)* **201** (2004) 2203-2212.

[56] J. Zang, C. M. Li, X. Cui, J. Wang, X. Sun, H. Dong, C. Q. Sun, Tailoring zinc oxide nanowires for high performance amperometric glucose sensor. *Electroanalysis* **19** (2007) 1008-1014.

[57] J. D. Sunandan Baruah, pH-dependent growth of zinc oxide nanorods. *Journal of Crystal Growth* **311** (2009) 6.

[58] L. N. Demianets, D. V. Kostomarov, Mechanism of zinc oxide single crystal growth under hydrothermal conditions. *Annales de Chimie Science des Matériaux* **26** (2001) 193-198.

[59] P. D. Agnieszka Kawska, Oliver Hochrein, and Dirk Zahn, Atomistic mechanisms of ZnO aggregation from ethanolic solution: Ion association, proton transfer, and self-organization

Nano Letters **8** (2008) 5.

[60] R. A. Laudise, A. A. Ballman, Hydrothermal synthesis of zinc oxide and zinc sulfide1. *The Journal of*

Physical Chemistry **64** (1960) 688-691.

[61] W.-J. Li, E.-W. Shi, W.-Z. Zhong, Z.-W. Yin, Growth mechanism and growth habit of oxide crystals. *Journal of Crystal Growth* **203** (1999) 186-196.

[62] L. N. Demianets, D. V. Kostomarov, I. P. Kuz'mina, S. V. Pushko, Mechanism of growth of ZnO single crystals from hydrothermal alkali solutions. *Crystallography Reports* **47** (2002) S86-S98.

[63] J. M. Wu, Y. R. Chen, Ultraviolet-light-assisted formation of ZnO nanowires in ambient air: Comparison of photoresponsive and photocatalytic activities in zinc hydroxide. *The Journal of Physical Chemistry C* **115** (2011) 2235-2243.

[64] Y. H. Yang, X. Y. Chen, Y. Feng, G. W. Yang, Physical mechanism of blue-shift of UV luminescence of a single pencil-like ZnO nanowire. *Nano Letters* **7** (2007) 3879-3883.

[65] J. H. Choy, E. S. Jang, J. H. Won, J. H. Chung, D. J. Jang, Y. W. Kim, Soft solution route to directionally grown ZnO nanorod arrays on si wafer; room-temperature ultraviolet laser. *Advanced Materials* **15** (2003) 1911-+.

[66] X. Q. Meng, D. Z. Shen, J. Y. Zhang, D. X. Zhao, Y. M. Lu, L. Dong, Z. Z. Zhang, Y. C. Liu, X. W. Fan, The structural and optical properties of ZnO nanorod arrays. *Solid State Communications* **135** (2005) 179-182.

[67] H. T. Ng, B. Chen, J. Li, J. Han, M. Meyyappan, J. Wu, S. X. Li, E. E. Haller, Optical properties of single-crystalline ZnO nanowires on m-sapphire. *Applied Physics Letters* **82** (2003) 2023-2025.

[68] A. B. Djurisic, Y. H. Leung, K. H. Tam, Y. F. Hsu, L. Ding, W. K. Ge, Y. C. Zhong, K. S. Wong, W. K. Chan, H. L. Tam, K. W. Cheah, W. M. Kwok, D. L. Phillips, Defect emissions in ZnO nanostructures. *Nanotechnology* **18** (2007).

[69] Z. Q. Chen, S. Yamamoto, M. Maekawa, A. Kawasuso, X. L. Yuan, T. Sekiguchi, Postgrowth annealing of defects in ZnO studied by positron annihilation, x-ray diffraction, rutherford backscattering, cathodoluminescence, and hall measurements. *Journal of Applied Physics* **94** (2003) 4807-4812.

CHAPTER 2

Submerged liquid plasma and metal oxides surfaces

2.1 Submerged liquid plasma

2.1.1 Mechanism of submerged liquid plasma

Plasma creation is generated when ionization of molecules or atoms in gas takes place when heat energy is applied externally or through collisions.[1-4] A submerged liquid plasma is a plasma evolution in a liquid/gas dual phase while electrolysis process takes place.[5-7] If high voltage (>100V) is applied, spark of light ignited on the surface of the electrode. Figure 2.1 shows current-voltage curve of Ni during plasma electrolysis. It is defined regions 4 and 5 as the plasma regions[5]: (1) conventional region, (2) breakdown point, (3) transitional region, (4) partial plasma region, and (5) full plasma region. In general, a medium structure of electrons population is indispensable to sustain the discharge.

Type of discharge during the evolution of plasma is classified to two types.[8-10] glow-discharge and arc-discharge. Arc-discharge is a state when the plasma becomes highly conductive and a rapid drop in voltage with increasing current occurs. This mode is widely used in welding, cutting, and plasma spraying. On the other hand, glow-discharge produces a volume of stable plasma.[11] High voltage promotes reactions of

energetic electrons. Collision of energetic electrons with neutrals can cause ionization and collisions with less energetic electrons can produce electrically excited species. Some will emit energy photons as visible light when they decay to their ground state. The phenomena gave rise to the term “glow discharge”. The emitted light can be used to perform optical emission spectroscopy, which can identify excited species based on the wavelength of the emitted light. Figure 2.2 illustrates generation of vapor/gas sheath on the electrode’s surface during plasma electrolysis.

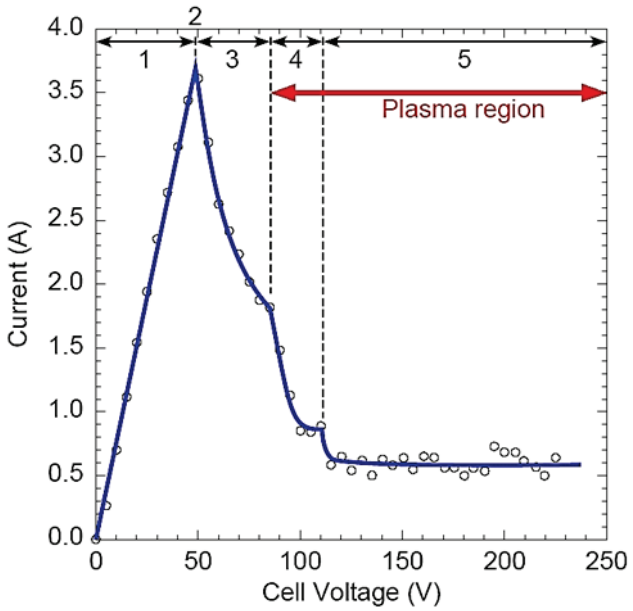

Figure 2.1 – V-I curve characteristic of plasma electrolysis.[5]

At the time the electrode’s surface temperature exceeded the electrolyte boiling point, sheath of gas layer consist of water vapor and hydrogen gas will form. If the applied voltage is sufficiently high, ions can be accelerated across the sheath, producing energetic ions bombardment of the surface and give rise to the occurring of glow-discharge. If the

cell voltage is low, the electrolyte's voltage will only encourage electrolysis reaction on the electrode's surface where hydrogen gas is generated at the cathode. In this research's experiment system, the discharge electrode is not the anode, but cathode, which anode's surface is larger than the cathodes to concentrate the voltage drop at the cathode over the electrolyte interface. When the cell voltage increases gradually, power deposition occurs in the cathode fall by collisions with hot electrons, making the electrode's temperature exceeds the electrolyte's temperature and finally the vapor/gas layer sheath is formed.

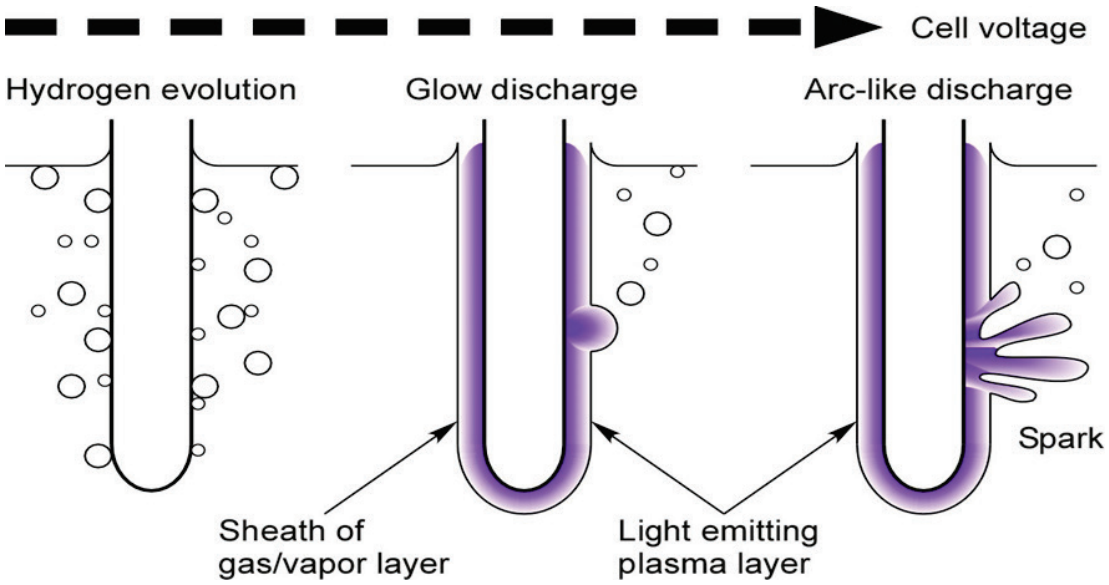

Figure 2.2 - Illustration of vapor/gas sheath generation of electrode's surface during plasma electrolysis.[5]

At this time, the buildup of hydrogen gas covering the electrode detaches its contact with the electrolyte whereas current marginally increases. With further increase of voltage, the gas layer and glow discharge expands to the whole electrode's area, thereby

the current drop starts rapidly in region 5. This satisfies the first important condition to sustain glow-discharge that in atmospheric low voltage, the electrode's surface is fully covered by the gas layer and at this time, if the cell voltage is sufficiently high, it satisfies the second important condition that the emitting of light is confirmed. The origin of electric currents in the vapor/gas layer comes from the electrons and positive ions produced during ionization of neutral gas atoms, which move under an external electric field. Such a field gives the charge carriers a drift velocity so that a uniform current can persist between the two electrodes. Since the electrons are lighter in mass compared to the ions, they have much larger kinetic energies and are mainly responsible for ionization of atoms. Under the electric field, the electrons drift towards the anode (+ electrode) and the ions drift towards the cathode (- electrode).

Paschen's law[12, 13] explains the initiation of discharge by relating the gas density with pressure. It functions the breakdown of gas by product of the gas pressure and the free path of electrons collisions with gas molecule for uniform field, which in this study attributed to the electrode. In Figure 2.3, more kinetic energy is gained but less collisions occurs between ions during when the gas density is low, but at high gas density, the collisions frequency gets higher but less energy is gained. While the electrolyte temperature is maintained between 70 – 90 °C, vaporized phase pressure will have at least

1 atm. Even gas breakdown in 1 atm region is challenging, needing to have high voltages. If the increase of voltage exceeded the breakdown point, the gas density sparsely thickens and enlarges the accelerating energetic electrons distance. Hence the plasma temperature and excitation energy increases, releasing photon energy.

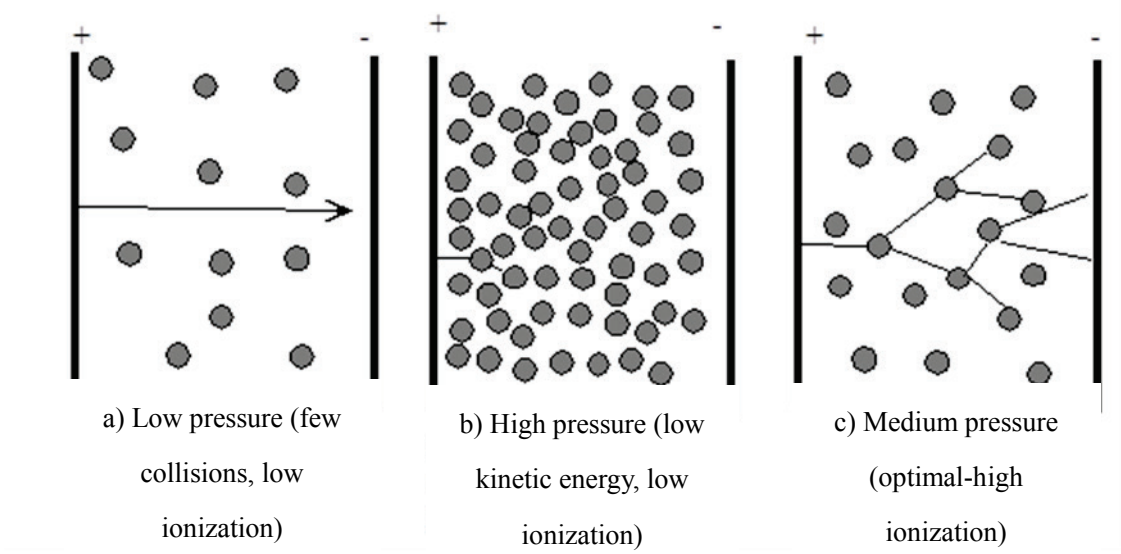

a) Low pressure (few collisions, low ionization)

b) High pressure (low kinetic energy, low ionization)

c) Medium pressure (optimal-high ionization)

Figure 2.3 - The effect of pressure to the ionization of molecules in gas.

In some case, as micro current pass flow is created between the electrode's surface and electrolyte, flashover of white light of arc discharge is extinguished. A low melting point material will rapidly melt at this stage because of the high volume of current. The sequence process of arc discharge plasma occurring is shown in Figure 2.4. 1.5 mm diameter of Ni wire's glow-discharge started at the tip point and addition of cell voltage downstream the white spark on the specimen.

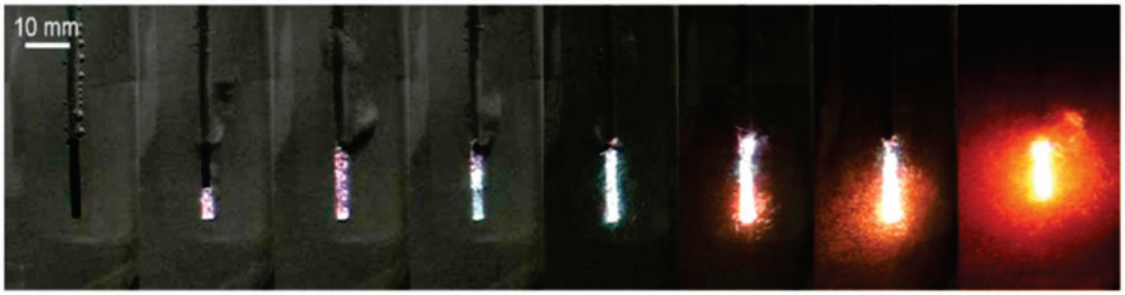

Figure 2.4 – The transition from glow-discharge to arc-discharge. [Ref. 5]

Plasma electrolysis in solids, liquids, gaseous, and plasmas is challenging with many possible control factors. There is still much to be studied until the best optimal condition for plasma occurring is found. In particular, the dynamic condition for glow-discharge to occur relies on the generation of gas sheath on the electrode's surface which the electrode's minimum temperature agreeable to be approximately 100 °C as the electrolyte's temperature increase. The cell voltages increment then stabilize and control the glow-discharge formation.

2.1.2 Factors of plasma glow-discharge motion

Other conditions adhering to glow-discharge is considered in other viewpoints such as the type and concentration of electrolyte, electrical field, and heat conductivity. They are related to power deposition and electrolyte's temperatures, thus can influence the breakdown point.[6, 14] During plasma electrolysis, there are two inputs to the system: heat flux from the plasma channel and injection of current. These inputs then give rise to

the joule heating; the electrode surface is partially melted by the local current concentration induced by electrothermal instability to result nonlinear equilibrium states.[5] Previous analyses of electrothermal instability in noble gas magnetohydrodynamic (MHD) generators have been concerned with fluctuations occurring in plasma region that makes the electrical power output is considerably lower than the theoretical prediction. This then disseminated research to reduce the arc discharge effect to MHD generator's electrode such the heat transfer loss due to arc discharge on the electrode's wall and boundary layer is studied. Figure 2.5 schematically illustrated the structure of electrothermal instability.

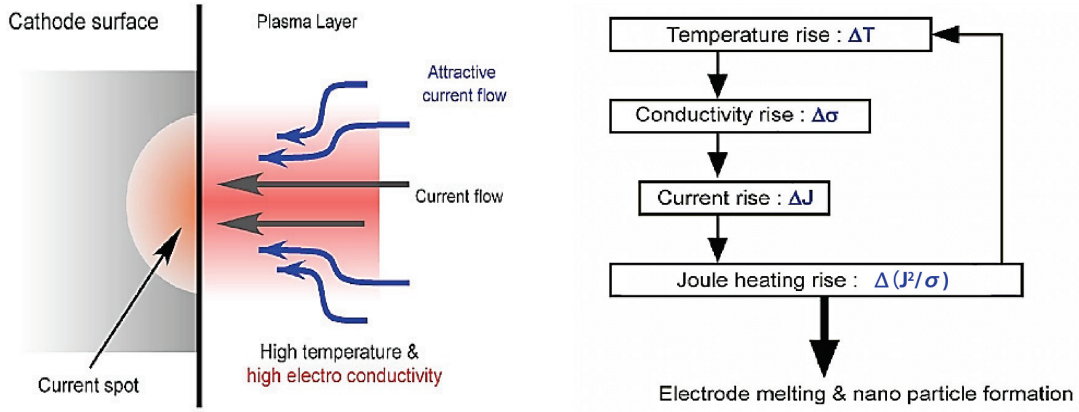

Figure 2.5 – Electrothermal instability structure. [Ref. 5]

The current density, joule heating, plasma temperature and conductivity rise orderly and repetition of this order in very short of time result the current concentration. If the ignition of discharge is stable at atmospheric pressure, the current concentration on the whole electrode's surface is equal. However, due to presence of the surface's

microstructure, the electric fields become uneven and also because of the power deposition stability limit, it is inevitable that fluctuation to exist coinciding voltage and current. In case of plasma electrolysis, the gas layer buildup is only in approximated measurement and due to enhanced electric fields, the generation of gas advance to top direction of the electrode and as the gas pressure and thickness are depending on the flow-rate and gas-dynamics of flow, distribution of current concentration exist. If one local point of concentration increases higher than the ambient current concentration, the joule heating density will increase the same amount of it. Therefore, the current plasma becomes intense as the temperature increases. Plasma conductivity is considered as temperature's coefficient and increases rapidly. The initial point of conductivity is high which the current flow is very fast, thereby increases the current value and this process repeat many times.

The current concentration is significantly sustained by the proportional of heat input from dissipative joule heating and heat scattering. It is well known that when the ambient temperature is low enough, the occurrence and developing frequency of current concentration due to electrothermal instability is very high. In case of plasma electrolysis, even at low applied voltage, the heat acquired due to current concentration is considered as high. It comes to an agreement here that the development of current concentration

originated from electrothermal instability is remarkably fast compare to metallic electrode's heat conduction and meltdown. Suppose that a nanoparticle can be produced from one melting spot, the size of that nanoparticles can be measured by the melted quantity. As current concentration is high at low voltage, diameter size of the nanoparticle will be bigger. Plasma electrolysis experiment performed can be applied to conductive electrodes and considerably can construct diverse oxidative surface of metallic materials.

The type of electrolyte is adequately selected to reduce the effect of hydrogen absorbed to the surface. Due to high heat from plasma, direct thermal decomposition of water molecules occur and as the activation of plasma phase is in high temperature of oxidative atmosphere, oxidation reaction of nanoparticles take place while they are synthesized. Therefore, the type of electrolyte could influence the degree of oxidation. In specific, without use of solution, created plasma region will be non-oxidative, thus project a creation of perfect metallic particles. As the type of electrolyte can control the level of plasma phase electrolysis as well, the current concentration can change too. Finally, the nanoparticle size distribution can also change. However, the energy properties in current concentration do not totally depend on plasma condition, but also the conductivity of the electrode used. In metals' melting and solidification process, heat transfer's properties and surface tension are both very important factors. In the viewpoint of corrosion, the

electrode's properties can affect the chemical reaction potential. This idea was clarified by indifference behavior of Au and Ag particles' generation and the thermal, electrical, chemical behaviors are actually very similar.

Here, inhibiting the electrode to be melted by electrolyte must be put into consideration. In other words, by utilizing the electrolyte at high temperature, to ensure the electrode's physical stability in high heat region, choosing a suitable electrolyte is very important.

2.1.3 Effect of submerged liquid plasma to electrode

The change of plasma motion due to extended discharge time will occur together with the change of electrode's surface area. Therefore, even at this time there is much to study on plasma's controllability, if it is to achieve small production of high quality nanoparticle, possible good controllability can be acquired from discharge time dependency perspective but as long as the electrode's discharge is not stopped, it eventually gives merit to constant production of nanoparticles. The dominating factor of synthesized nanoparticles' characteristic is the cell voltage. The diameter size of nanoparticles will be smaller by higher cell voltage.[5, 15]

Therefore, craters will appear on the electrode's surface during this production of nanoparticles. The typical voltage-current and electrolyte's temperature characteristic

during plasma-discharge on a Zn plate is shown in Figure 2.6. This research focuses on the plasma treatment that creates nanosized bumpy surface on the electrode. Plasma-treated electrode is irradiated with ultraviolet (UV) (λ = 365 nm) wavelength of light

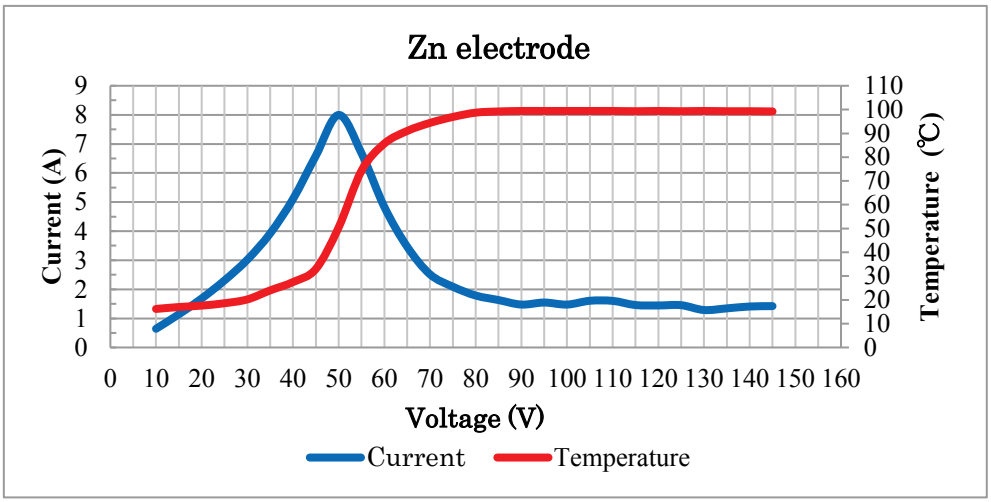

Figure 2.6 – V-I curve and electrolyte's temperature increase on Zn plate.

for certain durations for crystal growing that will be explained in more details in Chapter 3. In the experiment performed, each different material of electrode has a specific range of cell voltages to ignite plasma enough to construct the bumpy surface. As a contrast, the glow-discharge state as partial plasma or complete plasma (arc-discharge) and extension time of the discharge enable the generation of sufficient bumpy surface for following crystal growing purpose. However, as stated before, the constrains to control plasma has not been fully understood yet, thereby the production of nanoparticles as well as bumpy surface is only done by approximate specified measurements. Indeed, investigation for quantification measurement method is extensively being conducted at this time.

Plasma electrolysis is known as new method to synthesis nanoparticles with gas/liquid dual phase interface. If the principal method to control the non-equilibrium process is achieved, the advantages from each gas phase method and liquid phase method can be utilized efficiently and directly project a new reaction process.

2.2 Metal oxides surfaces

2.2.1 Introduction

The physics and chemistry of metal oxide surfaces have led many powerful new techniques for the study of oxides. For decades, oxide surfaces have played a key role in corrosion protection, catalysis, sensors, fuel cells, ceramics, etc. Over the last few years, totally new devices and technologies that rely on the properties of oxide surfaces and interfaces have emerged. This section highlights a few of which one should think about the properties of metal oxides.

2.2.2 Electronic properties of metal oxides

In this research, it is necessary to understand band structure of metal oxides and band gap energy to apprehend the method of UV irradiation on plasma-treated electrode's surface. Valence electrons are responsible for the bonding of atoms. When there are few atoms, the energy values of electrons in orbits are scattered. However, when the number of bonded atoms increases, the values become continuous within a certain range, rather

than being scattered. This range is referred to as “energy band.” The area between two energy bands, where there is no electron energy, is referred to as “forbidden band.” Among the bands filled with electrons, the one with the highest energy level (the electron orbit farthest from the nucleus) is referred to as “valence band” and the band outside of this is referred to as the “conduction band”. The energy width of the forbidden band between the valence band and the conduction band is referred to as “bandgap” (Figure 2.7).[16]

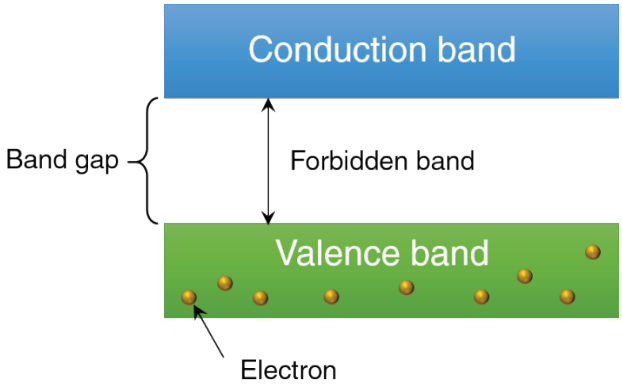

Figure 2.7 – Band gap structure.

The bandgap is like a wall that electrons must jump over in order to become free. The amount of energy required to jump over the wall is referred to as the “bandgap energy.” Only electrons that jump over the wall and enter the conduction band can move around freely. In the case of silicon, the band gap energy is approximately 1.1 eV, which is equal to approximately 1100 nm when converted to the wavelength of light. If titanium oxide (TiO_2) is irradiated with light of 388 nm (3.3 eV) or shorter, respectively, valence band

electrons are able to move up to the conduction band. At the same time, as many positive holes as the number of electrons that have jumped to the conduction band are created.

2.2.3 Crystal structure

Metal oxides crystal structures consist of metal cations coordinated in various ways by oxygen ligands.[17-19] Most common oxides have their cations octahedrally coordinated with six O ions, although in different crystal structures the octahedron will be distorted in different ways. Such structures include rocksalt, rutile, corundum, anatase and molybdenum trioxide. A few metal oxides have tetrahedrally coordinated cations, such as the wurtzite structure of ZnO. The spinel and inverse-spinel structures have a mixture of octahedrally and tetrahedrally coordinated cations. However, the predominance of octahedral and tetrahedral ligand coordination leads to one of the common ways of graphically representing metal oxide crystal structures.

Instead of showing the individual ions, the structure is drawn as a collection of octahedra or tetrahedra, where adjacent polyhedra share common corners, edges or faces;[18] this type of representation is shown in Figure 2.8 for three oxide crystal structures whose cations are octahedrally coordinated. In the rhenium trioxide structure, all octahedra share only comers. In rutile, both corner and edge-sharing are present, and corundum contains a mixture of edge- and face-sharing.

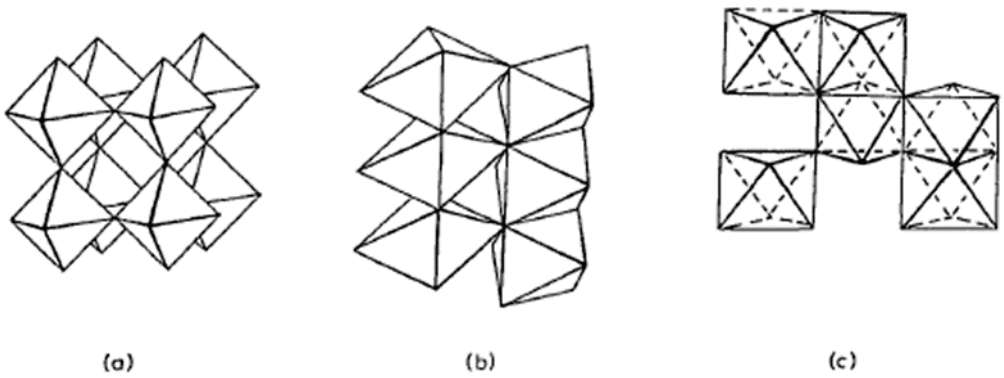

Figure 2.8 - Connected polyhedral representation of the bulk crystal structure of (a), rhenium trioxide, (b), rutile, and (c), corundum. [Ref. 18.]

2.2.4 Electrons transfering on oxide surface

Actual electron transfer does occur in oxidation/reduction, or "redox", reactions. In this type of reaction, there is a change in the oxidation state of the adsorbate. A simple example is the chemisorption of an alkali atom, in which it becomes a + ion, transferring its outer electron to empty electron orbitals of the substrate. It is the large electric dipole moment created by this charge transfer process that lowers the work function of surfaces on which alkali atoms are adsorbed by up to several eV. This type of bonding is generally strong, and it can also be either molecular or dissociative. A unique property of metal oxides is their ability to also exchange O ions with adsorbates; this property makes them very useful as partial oxidation catalysts. Such ion transport is a type of redox reaction in that charge (here in the form of an O^{2-} ion) is really transferred from the substrate to the adsorbate. A simple example of a redox reaction with O ion transfer is the oxidation of

CO:

$$CO + O^{2-}_{lattice} \rightarrow CO_2 + 2e^- \quad (2.1)$$

The oxide surface becomes reduced in this process; if this were a step in a catalytic reaction, some other O-containing species would have to donate an O atom back to the substrate in order for the reaction to continue. Like the other types of reaction, O-transfer adsorption can be either molecular or dissociative.

Photocatalytic process defines the new interest in somewhat different aspect of adsorption and reaction on metal oxides. The interest stems partially from that role that some transition-metal oxides can play in photochemical reactions in the atmosphere. Substantial work for photocatalysis reactions using transition-metal oxides: TiO_2 have been reviewed.[20-22] Its photochemical properties are of interest for several reasons. It determines the stability of pigmented system, the rate at which pollutants can be degraded in systems designed to purify air and water, and are the root cause of poorly understood phenomena such as water photolysis.

References

[1] A. Hickling, M. D. Ingram, Glow-discharge electrolysis. *Journal of Electroanalytical Chemistry (1959)* **8** (1964) 65-81.

[2] A. Hickling, M. D. Ingram, Contact glow-discharge electrolysis. *Transactions of the Faraday Society* **60** (1964) 783-793.

[3] A. Hickling, Electrochemical processes in glow discharge at the gas-solution interface. In *Modern aspects of electrochemistry no. 6*. (Springer US, 1971), chap. 5, pp. 329-373.

[4] H. H. Kellogg, Anode effect in aqueous electrolysis. *Journal of the Electrochemical Society* **97** (1950) 133-142.

[5] Y. Toriyabe, S. Watanabe, S. Yatsu, T. Shibayama, T. Mizuno, Controlled formation of metallic nanoballs during plasma electrolysis. *Applied Physics Letters* **91** (2007) 041501-041503.

[6] G. Saito, S. Hosokai, M. Tsubota, T. Akiyama, Ripple formation on a nickel electrode during a glow discharge in a solution. *Applied Physics Letters* **100** (2012) -.

[7] M. R. M. b. Julaihi, S. Yatsu, M. Jeem, S. Watanabe, Synthesis of stainless steel nanoballs via submerged glow-discharge plasma and its photocatalytic performance in methylene blue decomposition. *Journal of Experimental Nanoscience* (2014) 1-18.

[8] A. Von Engel, *Ionized gases.* (AIP Press, 1994).

[9] S. C. Brown, *Basic data of plasma physics.* (MIT Press, 1994).

[10] A. Marciniak, Non-uniform heating effects during treatment in a glow discharge. *Thin Solid Films* **156** (1988) 337-344.

[11] A. Bogaerts, E. Neyts, R. Gijbels, J. van der Mullen, Gas discharge plasmas and their applications. *Spectrochimica Acta Part B: Atomic Spectroscopy* **57** (2002) 609-658.

[12] F. Paschen, Ueber die zum funkenübergang in luft, wasserstoff und kohlensäure bei verschiedenen drucken erforderliche potentialdifferenz. *Annalen der Physik* **273** (1889) 69-96.

[13] J. E. Almy, The spark discharge in gases and vapors. *Physical Review (Series I)* **24** (1907) 50-59.

[14] G. Saito, T. Akiyama, Nanomaterial synthesis using plasma generation in liquid. *Journal of Nanomaterials* **2015** (2015) 21.

[15] G. Saito, Y. Nakasugi, T. Akiyama, Generation of solution plasma over a large electrode surface area. *Journal of Applied Physics* **118** (2015) 023303.

[16] S. Amemiya, Titanium-oxide photocatalyst. *Three Bond Technical News* (2004).

[17] V. E. Henrich, P. A. Cox, *The surface science of metal oxides.* (Cambridge University Press, 1994).

[18] P. A. Cox, *Transition metal oxides: An introduction to their electronic structure and properties.* (Clarendon Press, 1992).

[19] R. J. Lad, *Handbook of surface science.* (Elsevier, Amsterdam, 1996), vol. 1, pp. 185-228.

[20] A. Fujishima, T. N. Rao, D. A. Tryk, Titanium dioxide photocatalysis. *Journal of Photochemistry and Photobiology C: Photochemistry Reviews* **1** (2000) 1-21.

[21] C. H. Kwon, H. Shin, J. H. Kim, W. S. Choi, K. H. Yoon, Degradation of methylene blue via photocatalysis of titanium dioxide. *Materials Chemistry and Physics* **86** (2004) 78-82.

[22] D. Chen, A. K. Ray, Removal of toxic metal ions from wastewater by semiconductor photocatalysis. *Chemical Engineering Science* **56** (2001) 1561-1570.

CHAPTER 3

A pathway of nanocrystallite fabrication by photo-assisted growth in pure water

3.1 Brief summary

In this chapter, a new production pathway for a variety of metal oxide nanocrystallites via submerged illumination in water: submerged photosynthesis of crystallites (SPSC) is introduced. Similar to the growth of green plants by photosynthesis, nanocrystallites shaped as nanoflowers and nanorods are hereby shown to grow at the protruded surfaces via illumination in pure, neutral water. The process is photocatalytic, accompanied with hydroxyl radical generation via water splitting; hydrogen gas is generated in some cases, which indicates potential for application in green technologies. Together with the aid of *ab initio* calculation, it turns out that the nanobumped surface, as well as aqueous ambience and illumination are essential for the SPSC method. Therefore, SPSC is a surfactant-free, low-temperature technique for metal oxide nanocrystallites fabrication.

3.2 Background

New approaches to manufacturing the nanocrystallites of metallic oxides are desired due to their emerging applications in a wide range of high-technology

applications.[1-8] In the case of liquid-solid phase crystallisation studies, the surface morphology control plays an essential role in influencing the nucleation of nanocrystallites.[9] Recent studies have demonstrated the role of surface chemistry and morphology utilizing various mechanisms gained from polymeric substrates.[10, 11] Achieving those understandings provides a powerful means to widespread reports in nanocrystallites research.

The interest in this work is in the easy feasible design of nanocrystallites fabrication beneficial for the nanotechnology and environment. With regard to obtaining the desired products, a new pathway of production for variety of metal oxides nanocrystallites via SPSC is introduced. I chose various metals (Zn, W, Cu and Ce) to demonstrate the effectiveness of the submerged photosynthesis of crystallites (SPSC) method in obtaining a variety of morphologies of metal oxide nanocrystallites (NCs). The present report primarily focuses on ZnO nanofabrication due to its promising environmental[12] applications and broad range of modern device applications, including light-emitting diodes,[13] photo-detectors,[14] gas sensors,[15] and solar cells.[16]

The functions of these semiconductive ZnO (with a wide bandgap of 3.37 eV) devices are crucially dependent on the nanostructure morphology. Hence, it is important to tune and stabilise the syntheses parameter for improved performance. To this end, there

has been a substantial increase in the number of reports on hydrothermally synthesised ZnO nanostructures,[17, 18] including lasing and the addition of metal-ion impurity[19] techniques. Expanding on these efforts, this study develops a rational and environmentally benign approach to synthesise a plethora of ZnO nanomorphologies.

I employed the initial metal surface treatment based on the utilisation of the submerged liquid plasma process.[20, 21] The reaction of plasma in an aqueous solution facilitates the synthesis of metal oxide powder.[22, 23] Hence, this technique is adopted for the direct (one-step) synthesis of ZnO "seeds". The intention is to create a semiconductive reformed layer with protruding characteristics (nanobumps) on the material. For this purpose, a raw Zn metallic plate was used as the target material for the formation of nanobumps. The NC growth was then completed by a "photosynthesis" reaction, where the irradiation of UV light (typically λ = 365 nm and I = 28 mWcm^{-2}) on the nanobumps inside pure water assisted the growth of ZnO NCs.

The SPSC method is different from previous nanofabrication reports,[24, 25] in which a hydrothermal decomposition process using UV-Vis light irradiation directed the formation of NCs. Instead, it is found that the illumination in ultrapure water induced an apical growth characteristic via water radiolysis, as will be described later. Furthermore, I was able to demonstrate working NC fabrication at room temperature (RT) under

surfactant- and contamination-free conditions by eliminating the need for organometallic or other organic solution phases. Similar to the growth of green plants via botanical photosynthesis, SPSC method requires only light, water and nanobumps (crystallite seeds). Interestingly, the SPSC end products were accompanied by the generation of hydrogen gas, which gives rise to a potential application of this methodology as a green technology for energy, chemistry and nanotechnology.

3.3 Materials and Methods

3.3.1 Surface pretreatment

In the submerged liquid plasma experiment devices (Figure 3.1a),the anode was a φ0.5 x 1 mm platinum wire (Nilaco, Tokyo, Japan) with purity of 99.9% arched into a hemispherical glass mesh (R = 30 mm). The cathode (target material) was a raw metal Zn plate (Nilaco, Japan, 99.5%), cut into a size of 35 x 5 x 1 mm. A 60 mm^2 contact area with a wrapped φ0.5 mm Cu wire (Nilaco, Japan, 99.9%) on the tip of the Zn plate was used to prepare the working electrode. A solution of 0.1 mol/l K_2CO_3 with pH 11.5 was used as the electrolyte. Deionised water was used as the washing solution. Prior to the experiments, both of the electrodes were washed with deionised water, and the electrolyte was preheated to 90 °C. Insulation of the contact area between the Cu wire and Zn plate was achieved by a φ10 mm glass tube, ensuring that the exposed Zn plate length was

approximately 25 mm. Then, both of the electrodes were immersed in the K_2CO_3 solution (300 ml) and separated by distance of 30 mm.

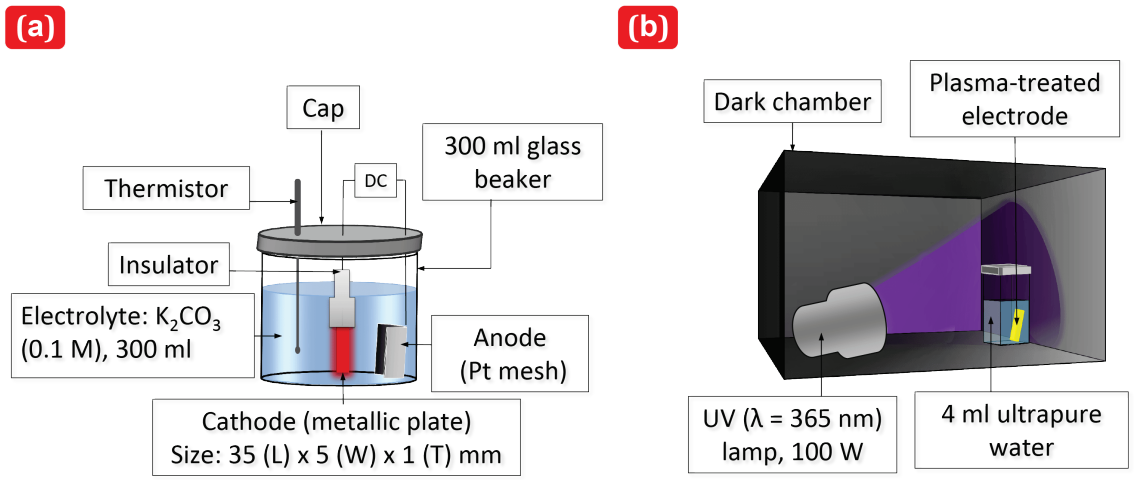

Figure 3.1 – SPSC experimental setups. (a) Submerged liquid plasma experimental setup. (b) Submerged UV irradiation experimental setup.

A discharge voltage of 140 V (current: 1.6 - 1.8 A) was applied across the electrodes using a direct current power supply (KIKUSUI, PWR1600H, Japan). The synthesis of nanobumps using submerged liquid plasma was conducted for a fixed reaction time of 10 min, appreciating the simple and time- and cost-efficient technique. At the end of the plasma reaction, the cathode was collected and washed with deionised water, and the length was cut to 25 mm. A white film surface, confirmed to constitute of ZnO, was obtained on the electrode surface. For further experimentation and analysis, the specimen was allowed to dry at ambient temperature.

3.3.2 SPSC experiment

In the UV irradiation experiment (Figure 3.1b), the plasma-treated Zn plate was inserted into a polymethylmethacrylate (PMMA) cuvette, which was then filled with 4 ml of ultrapure water (Wako Pure Chemical, pH 7-7.5, resistivity 18 MΩ) and capped. Prior experiments, the ultrapure water was degassed to remove the dissolved gas. A UV lamp (UVP, B-100AP, USA) with 100 W longwave UV ($\lambda = 365$ nm, 3.4 eV) was mainly used for SPSC. Visible light irradiation ($\lambda \approx 500$ nm) was employed for Figure 3.12(b) using spot light source (Hamamatsu LightningCure LC8, L9588, Japan). The irradiance orientation was set to the horizontal position, and the distance between the specimen and UV lamp was set to 100 mm. In the typical synthesis of nanocrystallites, the UV irradiation was performed in a dark chamber for a fixed reaction time (24 h) at room temperature. Extended UV irradiation times (48 h and 72 h) were also applied to clarify the NC growth characteristics (Figure 3.2(d), Figure 3.6, and Figure 3.12(d)). At the end of the UV irradiation, the specimen was collected, and the ultrapure water pH change was recorded using a pH meter (Horiba, D-51). For ZnO, the final pH of the water solution exhibited a typical increase to 8.5 in ambient temperature. The final water temperature increase was measured to be less than 10 °C.

3.3.3 Crystallite characterization

The surface morphology and elemental composition analysis of the substrates were monitored using a field emission scanning electron microscopy (FE-SEM, JEOL, JSM-7001FA). The chemical properties analysis was performed using X-ray diffraction (XRD, Rigaku, Tokyo, Japan, RINT2500HLB) with a Cu Kα line of 1.5406 Å and a scanning field of $2.5° \leq 2\theta \leq 100°$. Peak fitting was performed in referenced to JCPDS card 4-0831 and 5-0664. TEM micrographs, SAED patterns and HRTEM micrographs for the NCs were obtained using a double Cs-corrected-TEM (FEI, Titan cubed) operated at 300 kV.

3.4 Results and discussion

3.4.1 Surface morphology and crystallite structure

Figure 3.2a presents a scanning electron microscopy (SEM) image of ZnO nanobumps that were tailored by submerged liquid plasma treatment and depicts the metal surface having average of two or more protrusions per 10 μm^2. The protruded surface exhibits an average diameter of 1 μm or less. The higher-magnified image indicates the small ZnO seeds homogeneously localised on the protruded surface; these seeds have an average diameter of approximately 20 nm. Here, a drastic change in the seed clustering was observed after subsequent UV irradiation in ultrapure water and ambient temperature:

widely spread ZnO NCs covered the metal substrate. The previously localised seeds grew outward to form a bunch of nanorods that formed into nanoflowers (dandelion-like), dendrites (tree-like), and aligned nanorods (lawn grass-like) (Figure 3.2(b-d), respectively).

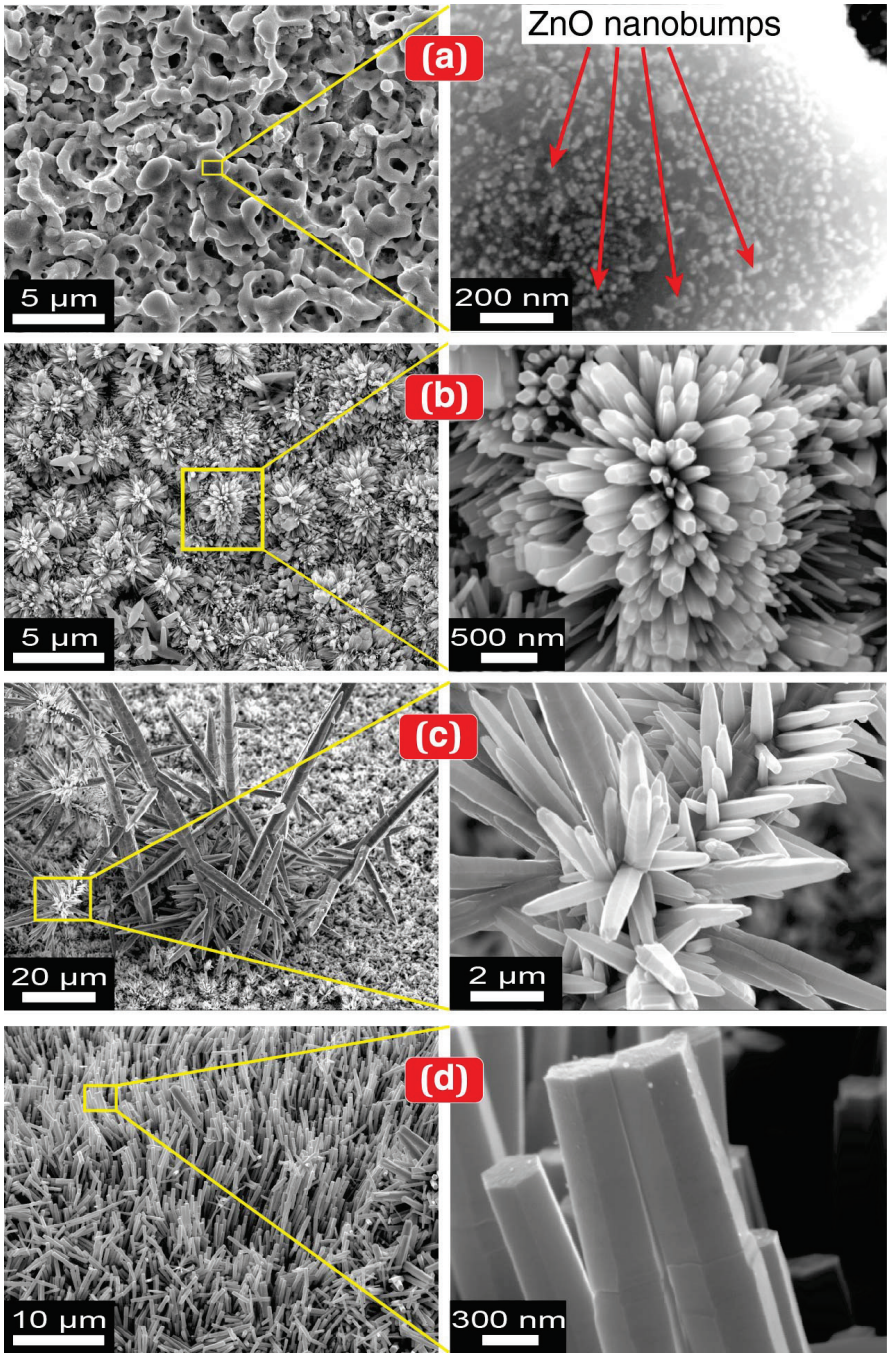

Figure 3.2 - Surface morphology after SPSC on a Zn substrate plate. (a) ZnO nanobumps (plasma 140 V, 10 min, UV_{0h}). (b) ZnO nanoflowers (UV_{24h}). (c) ZnO dendrites (UV_{24h}). (d) ZnO nanorods (UV_{72h}). The right panel images are the respective magnified FE-SEM micrographs. The heterogeneous growth is due to the local morphology variation via the plasma treatment. Typically, a fine structure of NCs can be obtained at room temperature after 24 h of UV irradiation. Extended irradiation increased the size and diameter but terminated the apical growth to yield flat, hexagonal tip ends (at UV_{72h} irradiation, as shown in (d) and Figure 3.3).

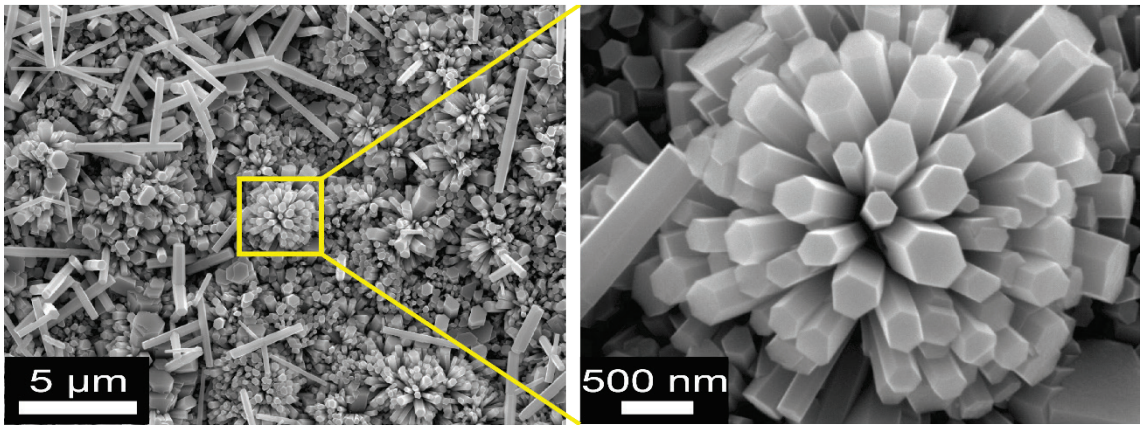

Figure 3.3 – Terminated apical growth of ZnO nanoflowers. A continuous 72 h of UV irradiation in ultrapure water resulted in flat, hexagonal tips of the nanostructures. The right panel is the magnified FE-SEM image.

The SEM-energy-dispersive X-ray spectroscopy (EDS) analysis (Figure 3.4(a-b)) and X-ray diffraction (XRD) analysis (Figure 3.4b) for the ZnO NCs illustrated that the NCs were synthesised on a Zn substrate, which contained Zn and O. As evidenced by the selected area electron diffraction (SAED) pattern and high-resolution transmission electron micrograph (HRTEM) of a nanorod examined along the $[1\bar{1}0]$ axis (Figure 3.4d), the nanorods were single crystallites (a wurtzite structure). The apical growth direction was in the c-axis <001>. This result is consistent with previous ZnO crystal growth reports.[24, 26, 27]

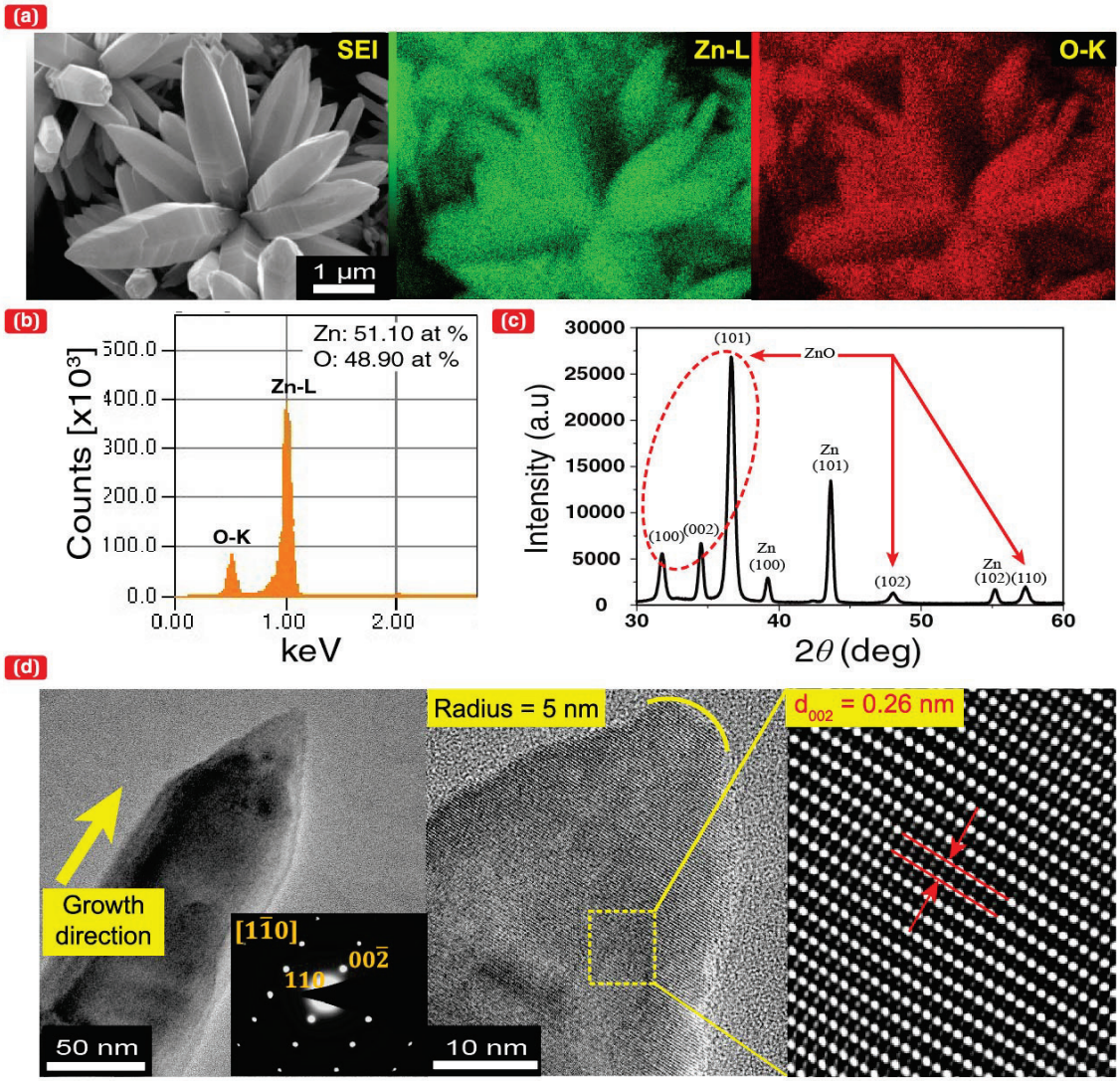

Figure 3.4 - Structural characterisation of ZnO NCs. (a) 2-D EDS map of ZnO nanoflowers (UV_{48h}); the left panel is a secondary electron image of ZnO crystals grown on the Zn substrate, centre: Zn, and right: O. (b) EDS spectrum and quantitative composition of ZnO. (c) XRD pattern of Zn and ZnO NCs. (d) TEM micrograph of a ZnO nanorod on a carbon thin film; the left panel is the TEM image (200 x 200 nm) of the ZnO nanorod, and the inset is the SAED pattern obtained along the $[1\bar{1}0]$ direction; the centre and right panels are the HRTEM image (40 nm × 40 nm) and its magnified image after inversed Fourier transformation, respectively. Figure 3.4d exhibits the apical growth direction of ZnO in the c-axis.

3.4.2 SPSC mechanism discussion by ab initio calculation

To consider the SPSC mechanism (as illustrated in Figure 3.5a) via dissociation

of water molecules (H_2O) on nanobumped ZnO surfaces, the electron density and bond-dissociation energy required to alter H_2O into OH and H radicals were calculated using *ab initio* simulations.[28, 29] To clarify the effect of the apical growth of NCs accompanied by the dissociation of water, the bond-dissociation energy was calculated for the flat surface (Figure 3.5b) and nanobumped surface (Figure 3.5c for curvature radius, R = 0.5 nm).

The simulation models of a flat surface and a nanobumped surface were constructed using Materials Studio® atomic simulation software (Accelrys Software Inc.). The calculations were performed based on density functional theory (DFT).[30, 31] The radii of curvature of the nanobumped surface, shown in Figure 3.5c and Figure 3.6(a-b), were set to 0.5, 1.0, and 2.0 nm, respectively. The grey, red, and white spheres in these figures represent zinc, oxygen, and hydrogen atoms, respectively.

Initially, two free H_2O molecules were placed in positions where strong interatomic forces were not exerted on each atom. The position of each atom in the equilibrated state was obtained using a dynamic simulated annealing method.[28, 29] In this method, the electronic states can be calculated by solving the quantum mechanical equation.

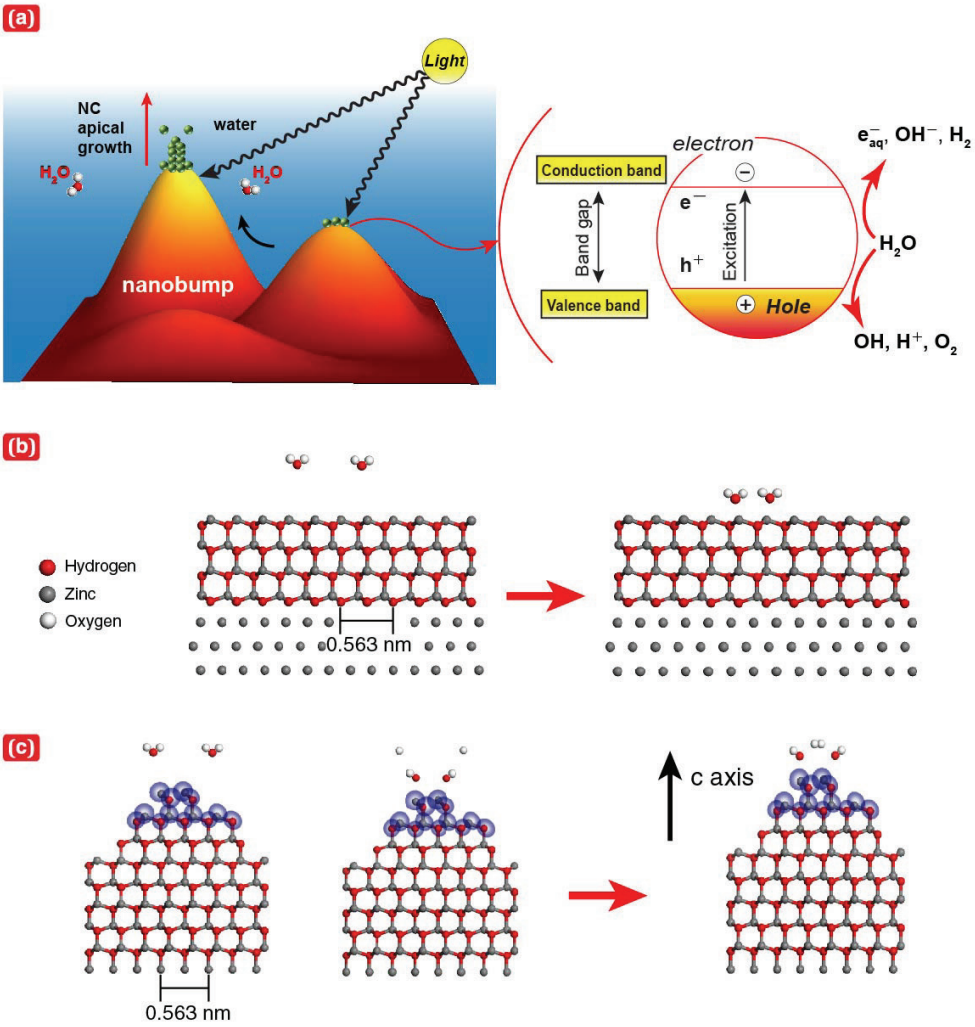

Figure 3.5 - Nanobumped surface effect in the SPSC model and simulation by molecular dynamical *ab initio* calculations. (a) A schematic of SPSC with a nanobumped surface. (b) H_2O molecules with a flat surface of ZnO. Water molecules localise at stable places near the flat surface. (c) Water molecule stabilised on the top of a nanobump (radius of curvature, R = 0.5 nm). Electron density isosurfaces of 2.0 electron/Å^3 (purple coloured) are observed only near the top of a nanobump. The state was relaxed to a state where a H_2 molecule is formed by equilibrating the state with the dissociation of H_2O molecules into OH and H.

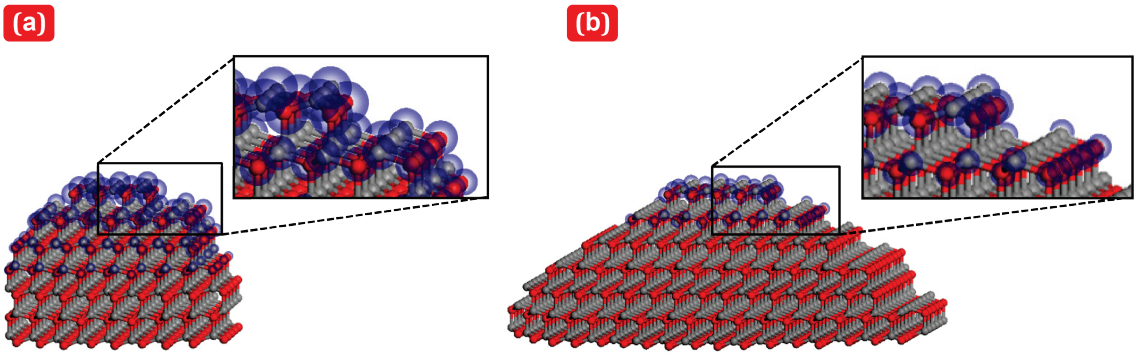

Figure 3.6 - Curvature radius dependence of the 1.7 electron/Å^3 electron density isosurfaces for nanobumped ZnO. (a-b) R = 1.0 and 2.0 nm, respectively. The isosurfaces are indicated by the purple coloured region. The larger radius of curvature resulted in decreased electron density at the apex.

The high electron density appeared to be localised near the top surface of a nanobump (Figure 3.5c). The dissociation energy for each surface was evaluated as the difference in the total energy of the dissociated state with H and OH and that of the equilibrated bonded state of H_2O. The calculated value for the flat surface was 5.03 eV without considering the photoexcitation effect, corresponding to the experimentally measured direct dissociation energy of a water molecule (5.1 eV).[32] In contrast, the dissociation energy for the nanobumped surface model was 0.323 eV when R = 0.5 nm (subsequently, 0.409 eV for R = 1.0 nm and 0.552 eV for R = 2.0 nm).

In the actual experiment for the effect of nanobumps, the reduced dissociation energy of the water molecules can be larger than 0.323 eV because the radius of curvature of the nanobumped (or apical) surfaces might be larger than 0.5 nm (e.g., approximately, 5 nm in Figure 3.4d). However, that value was considered to be considerably smaller than

5.03 eV for the flat surface because the apical radius of the curved surface was still extremely small (typically approximately 10 nm). Additionally, an illumination, e.g., a typical UV light (λ = 350 nm, 3.54 eV), further enhanced the dissociation of water molecules on the nanobumped surface because the photon energy was considerably larger than the dissociation energy for the nanobumped surface (0.323 eV). This energy difference resulted in the localised SPSC reaction increment via a photo-electron excitation effect, namely, the enhancement of equation (3.1) for the generation of additional excited electrons. Therefore, for the dissociated state of water molecules, which was induced by illumination, followed by an equilibration process, we obtained a final state, as shown in Figure 3.5c, in which H_2 molecule (gaseous) formation was predicted.

Overall, the local electron density and dissociation energy reduction at the top of the NC bumps played a key role in the SPSC process.

3.4.3 SPSC mechanism discussion by photochemical reaction

The mechanism for photosynthesised NCs in water via the SPSC process (Figure 3.5a) can, *in principle,* be described by the following photo-induced reactions:

The mechanism starts with water splitting into ion species in the vicinity of a semiconductive (SC) surface:

$$SC + h\nu \rightarrow SC(e^- + h^+) \quad \text{[via band gap excitation]} \tag{3.1}$$

$$H_2O + h^+ \rightarrow OH + H^+ \quad \text{[water dissociation]} \tag{3.2}$$

$$OH + e^-_{aq} \rightarrow OH^- \quad \text{[via hydrated electron: } e^- \rightarrow e^-_{aq}\text{]} \tag{3.3}$$

Hence, the water splits into ions by photoinduction (1) - (3):

$$H_2O + h\nu \rightarrow OH^- + H^+ \quad \text{[water splitting]} \tag{3.4}$$

The formation of transient species (H, OH, e^-_{aq}) and other molecular byproducts (H_2, H_2O_2) (see Figure 3.5c for $H + H \rightarrow H_2$) can be well understood as water radiolysis in radiation chemistry.[33] These reactions occur in short times of less than micro-second-order. Presumably, assisted by the aforementioned morphology effect, H^+ and OH^- at an apical hill in equation (3.3) throughout a protruded surface. Otherwise, H_2O will be immediately reproduced in the reverse of equation (3.4).Such locality-assigned ion production gives rise to a local pH imbalance: alkaline at the hill and acidic near the valley. Therefore, one can expect NC growth at a hill in association with hydrothermal reactions for ZnO generation in an alkaline solution:[26, 27]

$$Zn^{2+} + 2OH^- \rightarrow ZnO + H_2O \quad \text{[metal oxide growth]} \tag{3.5}$$

The metal may resolve into an ion at the valley:

$$Zn + H_2O \rightarrow Zn^{2+} + 2OH + H_{2(g)} \quad \text{[metal dissolution]} \tag{3.6}$$

Hence, the net SPSC reaction is completed with

$$ZnO + H_2O + h\nu \rightarrow ZnO + H_{2(g)} \qquad (3.7)$$

Similarly to known hydrothermal mechanism, NC growth by equations (3.5) – (3.6) might be accompanied by aggregation and recrystallisation processes of metal oxide nanoparticles. Thus, the SPSC is completed with three *principles*. Firstly, a photo-induced water splitting process. Secondly, separation of H^+ and OH^- ions due to nanobumps protruded surface. Finally, aggregation and recrystallisation of metal oxide nanoparticles (superimposed hydrothermal reactions) result in the nanocrystallites growth.

3.4.4 Photoexcitation and hydrothermal processes

Light, water, and the nanobumps favoured an essential meaning in the photo-synthesis process of metal oxides crystallites. As been discussed in the previous section, interfacing a photoexcitation process and hydrothermal (thermal oxidation in water) concurrently occur in room temperature condition.

In general, hydrothermal reactions in equations (3.5) and (3.6) are known to occur in alkaline solutions at higher temperatures.[18, 26, 27] Noting this, SPSC process was tested at two different water temperatures (10 °C and 60 °C) (Figure 3.7) other than room temperature. Growth rate of NC was accelerated when the UV_{6hr} irradiation experiment was brought into elevated temperature (Figure 3.7c). Nonetheless, the overall SPSC process is to occur assumed in a pure, neutral water environment rather than in acidic or

alkaline aqueous solutions. And despite this condition, one can observe the pH dependence or impurity additive influence on the final NC morphology.

Moreover, the photocorrosion effect,[34] e.g., $ZnO + 2h^+ \rightarrow Zn^{2+} + \frac{1}{2}O_2$, causes ZnO to redissolve into Zn ions or $Zn(OH)_2$ or $Zn(OH)_4^{2-}$ (equation (3.5)) and $Zn(OH)_2^{2-}$ (equation (3.6)). They may suppress the reaction processes and thus reduce the yield of SPSC in equation (3.7). However, the re-dissolution effect results in the possibility of ZnO recrystallisation at the initial fine nanocrystallites to regrow into thicker and wider NCs by re-precipitation, as shown in Figure 3.2(b-d).

The role of light for photoexcitation process is highlighted here, in comparison aspects of growth rate and growth characteristic with the hydrothermal effect. Although the obtained result highlighted the variation of temperature effects, UV illumination role must be concluded for the SPSC; which is the crystallites apical growth characteristic. The direct comparison in the case of UV and NO UV is presented in Figure 3.8.

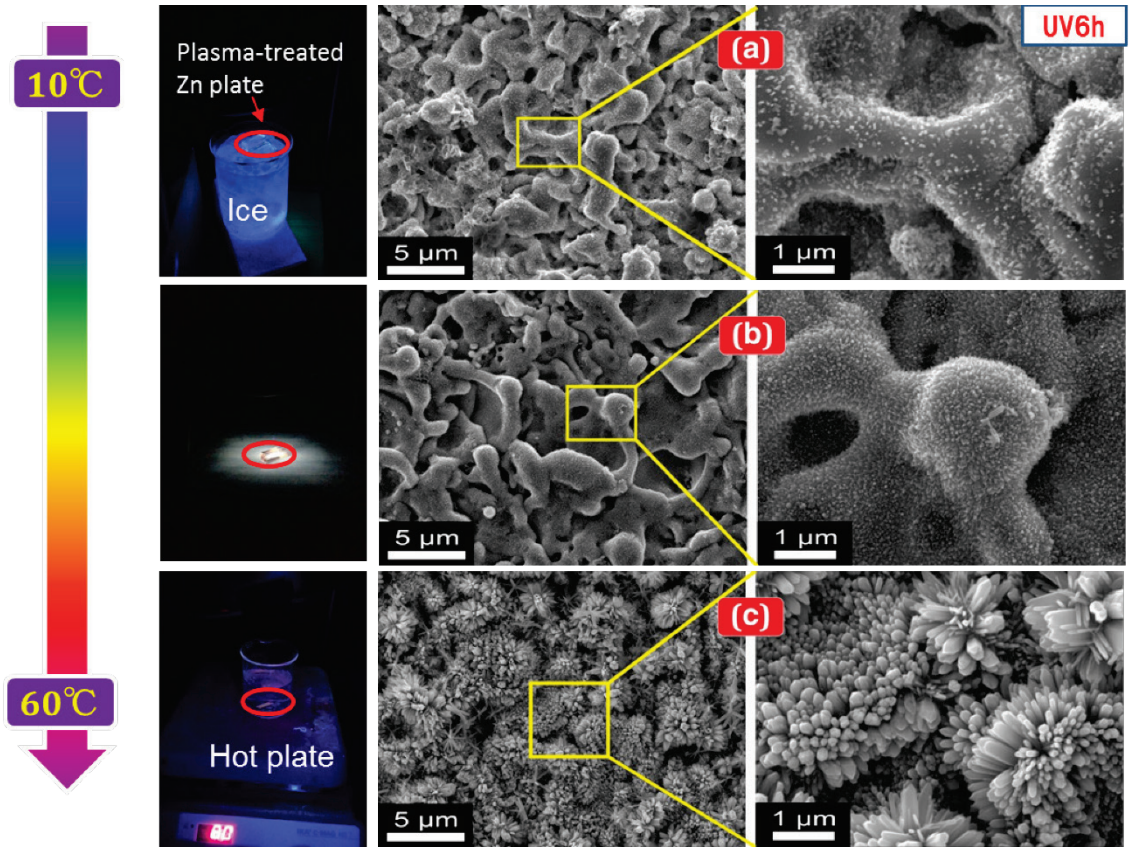

Figure 3.7 - Water temperature effect in ZnO crystallites growth under UV_{6hr} irradiation. (a) Low-temperature (~10 °C). (b) Room temperature (~25 °C). (c) High-temperature (~60 °C).

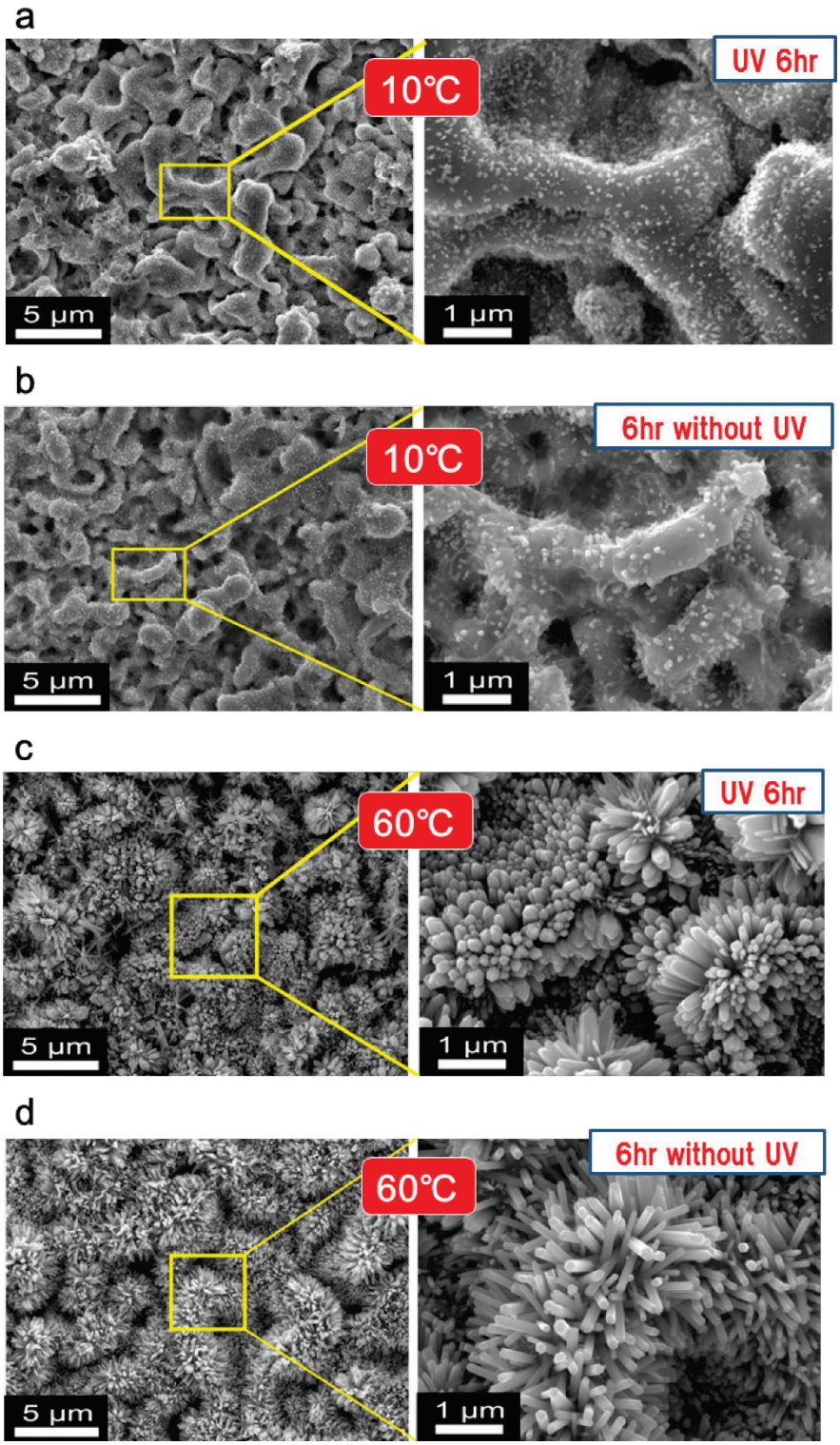

Figure 3.8 - Crystallites growth under UV and without UV conditions at elevated temperatures. (a) Zn UV_{6h} (Plasma 140 V, 10 min, T ≈ 10 °C). (b) Zn without UV6h (Plasma 140 V, 10 min, T ≈ 10 °C). (c) Zn UV_{6h} (Plasma 140 V, 10 min, T ≈ 60 °C). (d) Zn without $UV6_h$ (Plasma 140 V, 10 min, T ≈ 60 °C).

3.4.5 Nanobumps effect

The formation of crystallites is promoted inside alkaline condition, while the medium of growth is pure, neutral water. Despite of that, nanobumps encompasses the required condition in surface structure dependent manner.

i) Smooth surface morphology change on Zn plate

Smooth surface of Zn electrode (after plasma 140 V, 10 min) was tailored by focused ion beam system (FIB) (JEM-9320FIB). The processed smooth surface morphology images were recorded by FE-SEM. Then, UV irradiation for 6 hours in ultrapure water of that specimen was carried out. The result of surface morphology change is displayed in Figure 3.9.

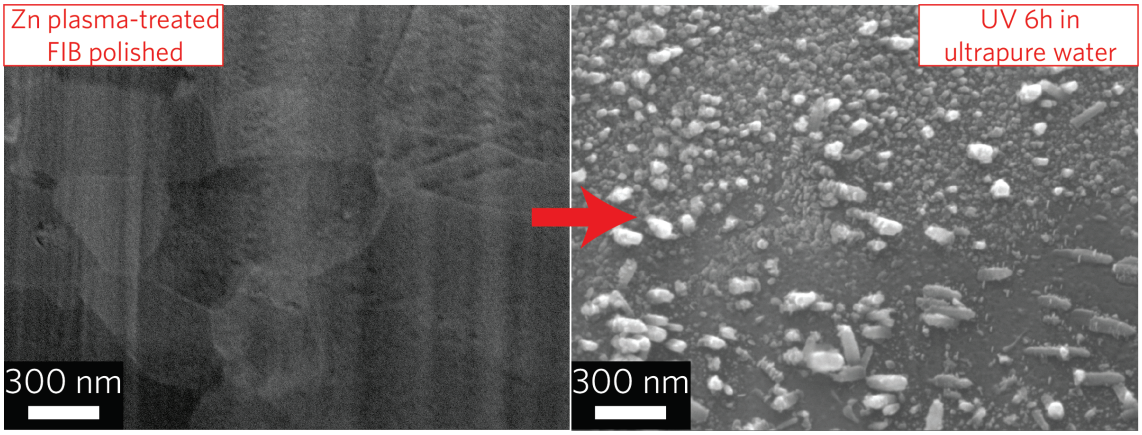

Figure 3.9 - Smooth surface morphology change on Zn (UV_{6h}).

ii) Surface morphology change of nanobumps on Zn

Surface morphology change of nanobumps on the same specimen in (i) was observed. Images of initial surface morphology also were recorded and 6 hours of UV irradiation

SEM observation result is shown in Figure 3.10.

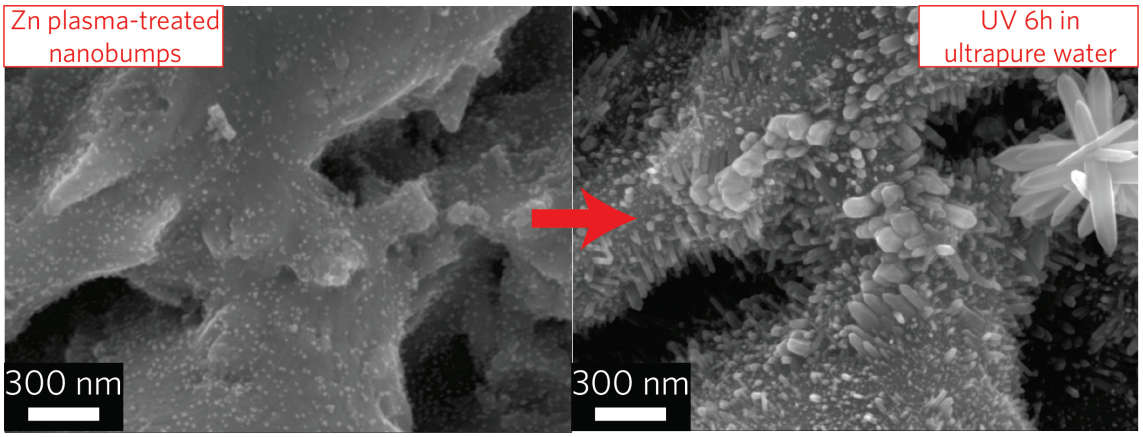

Figure 3.10 - Nanobumps surface morphology change on Zn (UV_{6h}).

Comparing the results from (i) and (ii), the nanobumps exhibited stronger texture of crystalline surface. EDS analysis results indicated the composition as ZnO. Smooth surface obtained from FIB processing turned out, to result also a crystalline surface after UV irradiation. This was due to the reduced (oxidized) size of surface by means of the beam irradiation (source is Gallium) of FIB, indirectly manufactured smaller size of nanobumps. Nonetheless, diffusion and re-deposition rate in (ii) was much faster, by simply observing the size of crystallites, and some single clustered nanorods on the surface.

3.4.6 Hydrogen gas and OH radical detection

The SPSC process characteristically predicts hydrogen gas ($H_{2(g)}$) and hydroxyl radicals (OH) as intermediate products (see Figure 3.11). To confirm the model, H_2 gas detection was conducted by using gas chromatography (GC) after the SPSC experiment.

The gas captured after UV_{120h} of six plasma-treated Zn substrates was used for GC analysis. The analysis of H_2 and O_2 gases was performed using a Shimadzu GC 8-A (thermal conductivity detector, molecular sieve 13X, N_2 carrier for H_2, and He carrier for O_2). For H_2 gas detection, 100% H_2 gas (100 µl) was injected into the GC using a microsyringe, and the calibration curve was plotted. Then, 100 µl of the captured gas was injected into the GC, and its concentration was compared with the calibration curve. The same steps were repeated when recording the O_2 concentration.

The obtained result gives in the H_2/O_2 ratio of 10. The value is five times more than two in the case of normal water splitting. Here, H_2 gas can also be produced by a typical photocatalytic reaction[12] ($2H + 2e^- \rightarrow H_2$), as well as via water radiolysis (with hydrogen radicals, Figure 3.5c) and hydrothermal reaction (equation (3.6)).

In the present study, OH radical generation was also investigated (Figure 3.11(a-d)) by monitoring the bleaching of *p*-nitrosodimethylaniline (PNDA) as the intensity of the characteristic absorption peak at λ = 440 nm decreased.[35, 36] During the UV light irradiation of the plasma-treated Zn plate, 4 ml of PNDA with a concentration of 1.5 mg/l was used as a scavenger in OH radical detection. Based from estimated O_2 production in Figure 3.11e, the greater factor of ~24 from the experiment results can neglect the dissolved gas effect in generated radicals: photo-induced water splitting governed the OH

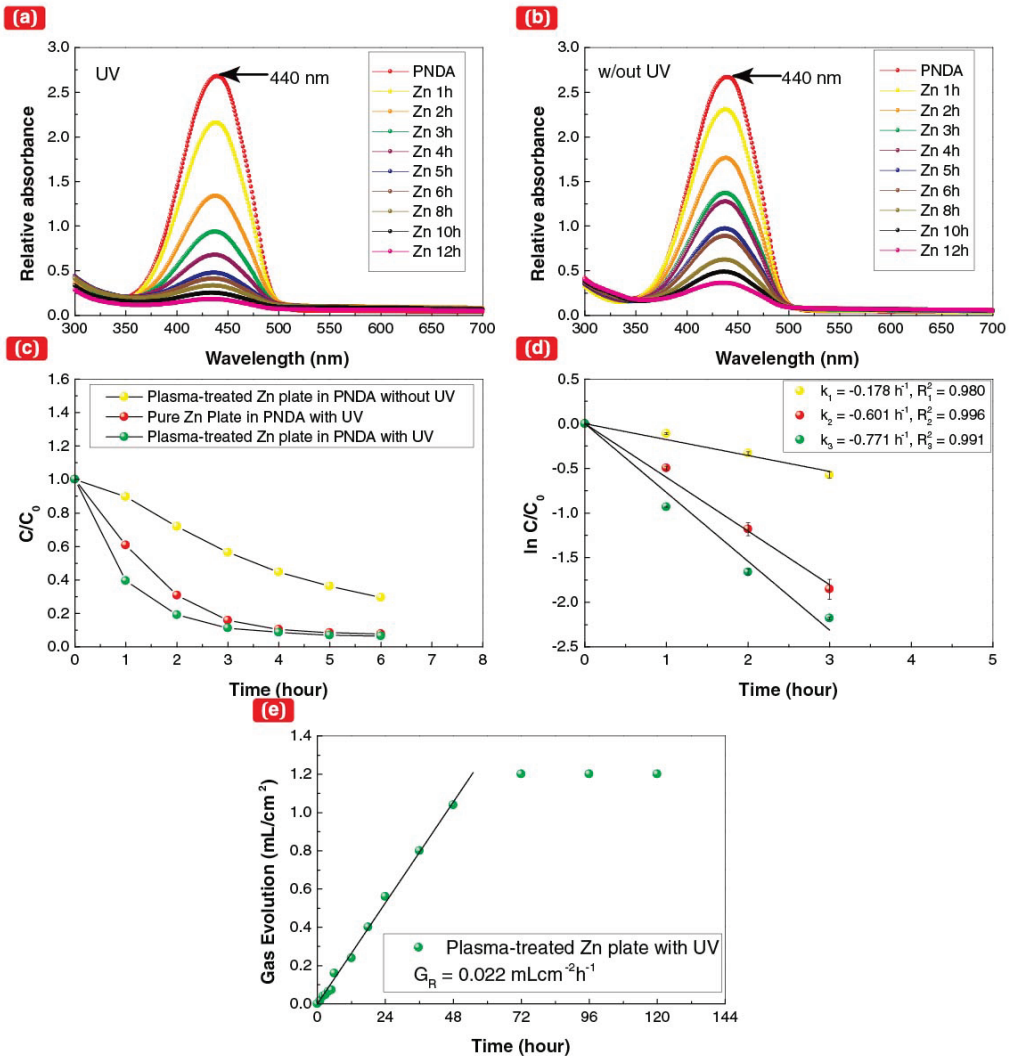

Figure 3.11 - Detection of OH radicals and measurement of gas evolution. (a-b) PNDA peak intensity decrease at λ = 440 nm to observe the effect of UV irradiation. (a) Plasma-treated Zn plate (UV). (b) Plasma-treated Zn plate (No UV). (c-d) Decomposition trend for PNDA by evaluating the concentration change at the λ = 440 nm peak. (e) Time dependence of the gas evolution on extended UV-irradiated, plasma-treated Zn. The gas volume increase slowed down after UV_{72h}, which is consistent with the terminated apical growth of a nanorod in Figure 3.2d.

radical production. The absorption spectra before and after UV irradiation were compared: the concentration of PNDA was measured using a JASCO V-630 UV-Vis spectrophotometer. Then, the time vs. exponential decay was plotted, and the first-order reaction rate (k) was calculated.

These results confirm the photochemical reactions proposed for the SPSC process, in which H_2 gas and OH radicals were generated during the photo-assisted growth of ZnO nanorods.

3.4.7 SPSC tuning

With a slight modification of reactions in equations (3.5) - (3.7), the SPSC method can also be applied to derive a wide variety of metal oxide NCs (e.g., metals of Cu, Ce, and W, as shown in Figure 3.12). These modifications revealed the difference in the SPSC morphology, resulting in various NCs. In this work, submerged liquid plasma technique is typically employed as an initial surface nanostructure treatment of natively oxidised NC seeds. Nevertheless, other possible alternative seeding methods can also be applied, including laser processing, ion irradiation, and tribological, mechanical scratching.

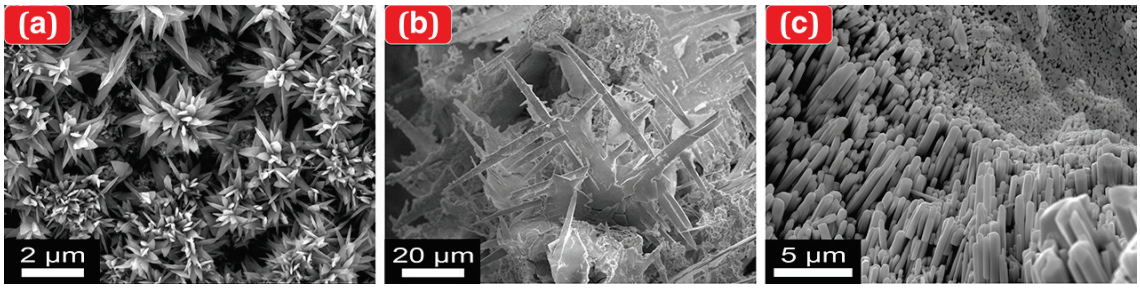

Figure 3.12 - Various nanostructures of metallic oxides produced by the SPSC method. (a) CuO nanoflowers (UV_{24h}). (b) CeO_2 dendrites (Vis_{24h}, $\lambda \approx 500$ nm). (c) WO_3 nanorods (UV_{48h}).

Such approach has been conducted by using ion irradiation as shown in Figure 3.13.

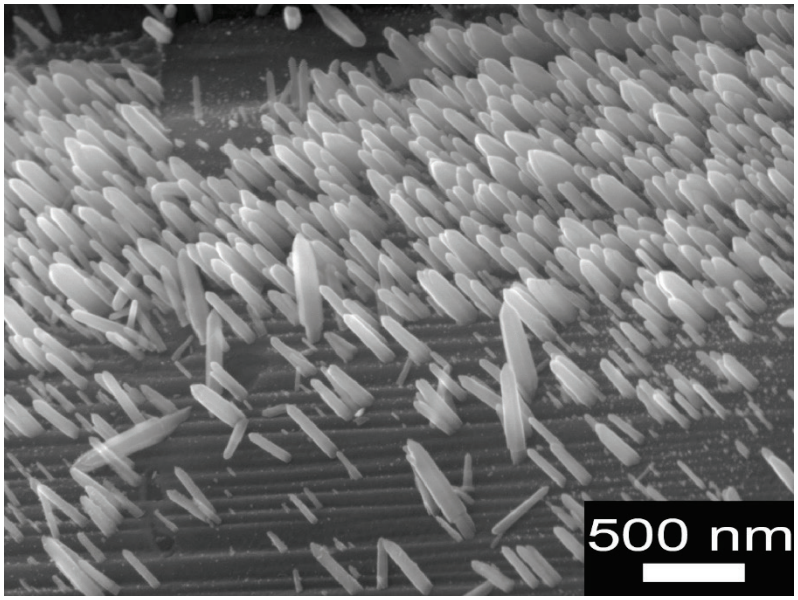

Figure 3.13 – ZnO nanorods array (UV_{24h}).

The ZnO (confirmed by EDS analysis) nanorods array were produced via SPSC method, but the nanobumps were tailored by ion irradiation (source: Ga in FIB system). The arrays are in parallel-alignment, and the grown ZnO nanorods exhibited average diameter of ~100 nm. This result gave an insight into oxides surface modification field for functional surface-applied nanotechnology development purpose.

Other approaches that would contribute into crystallites growth control is the introduction of specific dopants (Figure 3.14). As alteration of shape and chemical composition will determine the electrical, optical, etc. properties of the crystallites.[37-40]

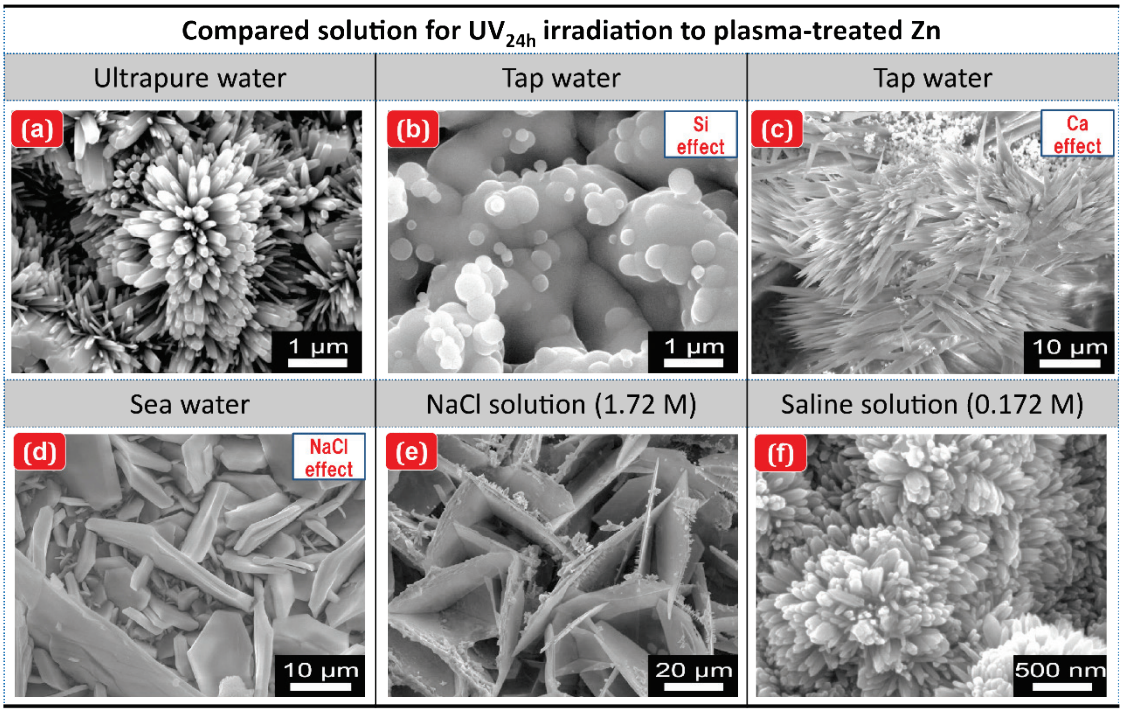

Figure 3.14 – Summary of different ions effect in the aqueous solution onto shape change of crystallites – Zn system (UV_{24h}).

Together with pH sensitivity explanation before, the introduction of dopants into the growth system generated a meaningful wider synthetic theme for SPSC. It directly provides an attractive and effective strategy for fabricating not only ZnO, but possibly other metal oxides crystallites with interesting compositional complexity.

3.5 Summary

In summary, SPSC requires *light*, ranging from UV to visible (as shown in Figure 3.12b), to assist the apical growth of NCs. Secondly, the use of *water* (specifically, ultrapure water) will deliver a fine structure of NCs. Because the NC morphology is

sensitive to pH changes and water impurities, the additive effect resulted in different morphologies. For example, Si from tap water resulted in sphere-like crystallites and NaCl from natural seawater resulted in plate-like crystallites (Figure 3.14d). These results are presumably caused by the alteration of the electronic state of the apical surfaces. Finally, metal oxide surface nanobumps act as the NC *seeds* and enclose the nucleation for the apical growth reaction.

References

[1] M. H. Huang, S. Mao, H. Feick, H. Yan, Y. Wu, H. Kind, E. Weber, R. Russo, P. Yang, Room-temperature ultraviolet nanowire nanolasers. *Science* **292** (2001) 1897-1899.

[2] X. Wang, J. Zhuang, Q. Peng, Y. Li, A general strategy for nanocrystal synthesis. *Nature* **437** (2005) 121-124.

[3] A. M. Morales, C. M. Lieber, A laser ablation method for the synthesis of crystalline semiconductor nanowires. *Science* **279** (1998) 208-211.

[4] Y. Kubota, K. Watanabe, O. Tsuda, T. Taniguchi, Deep ultraviolet light-emitting hexagonal boron nitride synthesized at atmospheric pressure. *Science* **317** (2007) 932-934.

[5] Z. W. Pan, Z. R. Dai, Z. L. Wang, Nanobelts of semiconducting oxides. *Science* **291** (2001) 1947-1949.

[6] Q. Huo, D. I. Margolese, U. Ciesla, P. Feng, T. E. Gier, P. Sieger, R. Leon, P. M. Petroff, F. Schuth, G. D. Stucky, Generalized synthesis of periodic surfactant/inorganic composite materials. *Nature* **368** (1994) 317-321.

[7] R. R. Salunkhe, J. Lin, V. Malgras, S. X. Dou, J. H. Kim, Y. Yamauchi, Large-scale synthesis of coaxial carbon nanotube/$Ni(oh)_2$ composites for asymmetric supercapacitor application. *Nano Energy* **11** (2015) 211-218.

[8] J. Lin, L. Zhao, Y.-U. Heo, L. Wang, F. H. Bijarbooneh, A. J. Mozer, A. Nattestad, Y. Yamauchi, S. X. Dou, J. H. Kim, Mesoporous anatase single crystals for efficient $Co^{(2+/3+)}$-based dye-sensitized solar cells. *Nano Energy* **11** (2015) 557-567.

[9] A. L. Briseno, S. C. B. Mannsfeld, M. M. Ling, S. Liu, R. J. Tseng, C. Reese, M. E. Roberts, Y. Yang, F. Wudl, Z. Bao, Patterning organic single-crystal transistor arrays. *Nature* **444** (2006) 913-917.

[10] Y. Diao, M. E. Helgeson, A. S. Myerson, T. A. Hatton, P. S. Doyle, B. L. Trout, Controlled nucleation from solution using polymer microgels. *Journal of the American Chemical Society* **133** (2011) 3756-3759.

[11] Y. Diao, A. S. Myerson, T. A. Hatton, B. L. Trout, Surface design for controlled crystallization: The role of surface chemistry and nanoscale pores in heterogeneous nucleation. *Langmuir* **27** (2011) 5324-5334.

[12] A. Fujishima, K. Honda, Electrochemical photolysis of water at a semiconductor electrode. *Nature* **238** (1972) 37-38.

[13] N. Saito, H. Haneda, T. Sekiguchi, N. Ohashi, I. Sakaguchi, K. Koumoto, Low-temperature fabrication of light-emitting zinc oxide micropatterns using self-assembled monolayers. *Advanced Materials* **14** (2002) 418-421.

[14] W. Tian, T. Zhai, C. Zhang, S. L. Li, X. Wang, F. Liu, D. Liu, X. Cai, K. Tsukagoshi, D. Golberg, Y. Bando, Low-cost fully transparent ultraviolet photodetectors based on electrospun ZnO-SnO_2 heterojunction nanofibers. *Advanced Materials* **25** (2013) 4625-4630.

[15] N. Golego, S. A. Studenikin, M. Cocivera, Sensor photoresponse of thin‐film oxides of zinc and

titanium to oxygen gas. *Journal of the Electrochemical Society* **147** (2000) 1592-1594.

[16] K. Keis, E. Magnusson, H. Lindström, S. E. Lindquist, A. Hagfeldt, A 5% efficient photoelectrochemical solar cell based on nanostructured ZnO electrodes. *Solar Energy Materials and Solar Cells* **73** (2002) 51-58.

[17] K. Govender, D. S. Boyle, P. B. Kenway, P. O'Brien, Understanding the factors that govern the deposition and morphology of thin films of ZnO from aqueous solution. *Journal of Materials Chemistry* **14** (2004) 2575-2591.

[18] D. Lincot, Solution growth of functional zinc oxide films and nanostructures. *MRS Bulletin* **35** (2010) 778-789.

[19] Z. R. Tian, J. A. Voigt, J. Liu, B. McKenzie, M. J. McDermott, M. A. Rodriguez, H. Konishi, H. Xu, Complex and oriented ZnO nanostructures. *Nat Mater* **2** (2003) 821-826.

[20] Y. Toriyabe, S. Watanabe, S. Yatsu, T. Shibayama, T. Mizuno, Controlled formation of metallic nanoballs during plasma electrolysis. *Applied Physics Letters* **91** (2007) 041501-041503.

[21] M. R. M. b. Julaihi, S. Yatsu, M. Jeem, S. Watanabe, Synthesis of stainless steel nanoballs via submerged glow-discharge plasma and its photocatalytic performance in methylene blue decomposition. *Journal of Experimental Nanoscience* **10** (2014) 965-982.

[22] S. Sōmiya, R. Roy, Hydrothermal synthesis of fine oxide powders. *Bulletin of Materials Science* **23** (2000) 453-460.

[23] M. J. Lee, C. B. Lee, D. Lee, S. R. Lee, M. Chang, J. H. Hur, Y. B. Kim, C.-J. Kim, D. H. Seo, S. Seo, U. I. Chung, I. K. Yoo, K. Kim, A fast, high-endurance and scalable non-volatile memory device made from asymmetric Ta_2O_{5-x}/TaO_{2-x} bilayer structures. *Nat Mater* **10** (2011) 625-630.

[24] L. Shi, K. Bao, J. Cao, Y. Qian, Sunlight-assisted fabrication of a hierarchical ZnO nanorod array structure. *CrysEngComm* **11** (2009) 2009-2014.

[25] J. M. Wu, Y. R. Chen, Ultraviolet-light-assisted formation of ZnO nanowires in ambient air: Comparison of photoresponsive and photocatalytic activities in zinc hydroxide. *The Journal of Physical Chemistry C* **115** (2011) 2235-2243.

[26] J. H. Jang, J. H. Park, S. G. Oh, Effects of dodecyl sulfate anionic surfactants on the crystal growth of ZnO through hydrothermal process. *Journal of Ceramic Processing Research* **10** (2009) 783-790.

[27] R. Shi, P. Yang, J. Wang, A. Zhang, Y. Zhu, Y. Cao, Q. Ma, Growth of flower-like ZnO via surfactant-free hydrothermal synthesis on ITO substrate at low temperature. *CrystEngComm* **14** (2012) 5996-6003.

[28] R. Car, M. Parrinello, Unified approach for molecular dynamics and density-functional theory. *Physical Review Letters* **55** (1985) 2471-2474.

[29] M. D. Segall, J. D. L. Philip, M. J. Probert, C. J. Pickard, P. J. Hasnip, S. J. Clark, M. C. Payne, First-principles simulation: Ideas, illustrations and the CASTEP code. *Journal of Physics: Condensed Matter* **14** (2002) 2717.

[30] W. Kohn, L. J. Sham, Self-consistent equations including exchange and correlation effects. *Physical Review* **140** (1965) A1133-A1138.

[31] P. Hohenberg, W. Kohn, Inhomogeneous electron gas. *Physical Review* **136** (1964) B864-B871.

[32] N. G. Petrik, A. B. Alexandrov, A. I. Vall, Interfacial energy transfer during gamma radiolysis of water on the surface of ZrO_2 and some other oxides. *The Journal of Physical Chemistry B* **105** (2001) 5935-5944.

[33] S. Le Caër, Water radiolysis: Influence of oxide surfaces on H_2 production under ionizing radiation. *Water* **3** (2011) 235-253.

[34] J. Domenech, A. Prieto, Stability of zinc oxide particles in aqueous suspensions under UV illumination. *The Journal of Physical Chemistry* **90** (1986) 1123-1126.

[35] J. H. Baxendale, A. A. Khan, The pulse radiolysis of p-nitrosodimethylaniline in aqueous solution. *International Journal for Radiation Physics and Chemistry* **1** (1969) 11-24.

[36] M. E. Simonsen, J. Muff, L. R. Bennedsen, K. P. Kowalski, E. G. Søgaard, Photocatalytic bleaching of p-nitrosodimethylaniline and a comparison to the performance of other AOP technologies. *Journal of Photochemistry and Photobiology A: Chemistry* **216** (2010) 244-249.

[37] D. J. Norris, A. L. Efros, S. C. Erwin, Doped nanocrystals. *Science* **319** (2008) 1776-1779.

[38] Y. Cui, C. M. Lieber, Functional nanoscale electronic devices assembled using silicon nanowire building blocks. *Science* **291** (2001) 851-853.

[39] Y. Yang, Y. Jin, H. He, Q. Wang, Y. Tu, H. Lu, Z. Ye, Dopant-induced shape evolution of colloidal nanocrystals: The case of zinc oxide. *Journal of the American Chemical Society* **132** (2010) 13381-13394.

[40] X. Peng, L. Manna, W. Yang, J. Wickham, E. Scher, A. Kadavanich, A. P. Alivisatos, Shape control of CdSe nanocrystals. *Nature* **404** (2000) 59-61.

CHAPTER 4

Tuning opto-electrical properties of ZnO nanorods with excitonic defects via submerged illumination

4.1 Brief summary

When applied in opto-electronic devices, a ZnO semiconductor dominantly absorbs or emits ultraviolet light because of its direct electron transition through a wide energy bandgap. On the contrary, crystal defects and nanostructure morphology are the chief key factors for indirect, interband transitions of ZnO opto-electronic devices in the visible light range. By ultraviolet illumination in ultrapure water, a conceptually unique approach to tune the shape of ZnO nanorods from tapered to capped-end via apical surface morphology control is demonstrated. Oxygen vacancy point defects activated by excitonic effects near the tip-edge of a nanorod is shown to serve as an opto-electrical hotspot for the light-driven formation and tunability of the opto-electrical properties. A double increase of electron energy absorption on near band edge energy of ZnO was observed near the tip-edge of tapered nanorod. The opto-electrical hotspot explanation rivals that of conventional electrostatics, impurity control and alkaline pH control associated mechanisms. Thus, it highlights a new perspective to understanding light-driven nanorods formation in pure neutral water.

4.2 Background

Morphology and defects are key determinants of the opto-electrical properties of materials used in cutting-edge optics and photonics applications. In this field of study, researchers no longer focus on the abundant variety of materials available, but have creatively designed unprecedented opto-electrical properties in metallic oxide nanostructures that support surface plasmons.[1-3] Light can be manipulated on the quantum level, enabling the exploration of surface plasmon properties and the fabrication of plasmonic devices. Proper geometry and phase tuning of the nanostructures can increase light absorption and emission, which in turn improve the nanostructures' performance in applications such as photovoltaics[4] and sensors.[5]

Zinc oxide (ZnO) has a wide direct band gap (E_g = 3.37 eV) and a high exciton binding energy (~60 meV), which can facilitate high carrier concentrations to probe the localized surface plasmon (LSP) via interband transitions. ZnO nanostructures, especially nanorods (NRs), have been widely used in various solar-driven energy and environmentally benign technologies.[6, 7] To modify and increase the NRs performance, researchers have continuously engaged in efforts to control the morphology of NRs, including controlling the pH[8] or adding nonmetal impurities.[8, 9] Doping and alteration of ZnO NRs or nanowire growth at the (002) top-plane and the (100) side-plane through

electrostatics can also enhance optical features.[9]

Recent studies have shown that a decrease in the size of Ag nanoparticles (NPs) induces an energy blue-shift of exciton-LSP coupling (plexiton) in ZnO nanowires.[10] The coupling was demonstrated through the study of LSP spatial distribution and ZnO excitations (near-band-edge (NBE) and exciton emission) using electron energy loss spectroscopy (EELS) combined with scanning transmission electron microscopy (STEM). STEM-EELS enables us to gain a new perspective to understanding the growth action by ZnO nanostructures through their optical excitation, which is defined by the electronic energy levels in the conduction and valence bands. The energy levels are discrete in several dimensions because of the quantum confinement effect and can be tuned by size and shape as well as by atomic defects.[11] At present, electrostatics in alkaline hydrothermal synthesis provide an essential mechanistic explanation toward NRs control.[9] However, the literature contains only a few reports regarding the effect of atomic defects, particularly in pure neutral solution, on the NRs growth mechanism.

Here, I developed an alternative and simple approach to engineer the opto-electrical properties of ZnO NRs: Tapered and capped NRs are fabricated via NRs time-dependent apical growth control. This behavior is explained by the opto-electrical hotspot concept that will be described later.

4.3 Materials and methods

4.3.1 Surface pretreatment

Surface pretreatment of a Zn plate was performed using the submerged liquid plasma technique, as described in our previous reports.[12, 13] The raw Zn plate (99.5%) used as the target material was procured from Nilaco, Tokyo. The plate used as a cathode in the submerged liquid plasma setup it was cut to 35 × 5 × 0.5 mm. Then, a direct-current voltage of 130 V and current of ~2.0 A was applied to initiate glow-discharge; these conditions were maintained for 5 min to construct the nanobumps on the surface.

4.3.2 Fabrication of ZnO NRs via SPSC

The submerged photosynthesis of crystallites (SPSC) for fabricating ZnO NRs was performed using room-temperature UV (λ = 365 nm) light illumination in a dark chamber.[12] The plasma-treated Zn was submerged into a 4 mL polymethylmethacrylate (PMMA) cuvette filled with ultrapure water. Ultrapure water was procured from Wako Pure Chemical with pH 7-7.5 and resistivity of 18 MΩ. The UV lamp illuminated the cuvette with a horizontal 10 cm gap to achieve the UV light intensity of 28 mW/cm^2. Prior to illumination, the ultrapure water was degassed by boiling. For the purpose of tracking the NR morphology change, the Zn SPSC specimens were independently illuminated for designated durations.

4.3.3 pH-T measurements

The pH-T trend of the ultrapure water during SPSC was recorded using a portable D-72 pH/ORG meter (Horiba, Japan). The pH-T reading was obtained using a micro pH electrode (9618S-10D) with the ability to read pH-T in 50 μL of solution.

4.3.4 Surface microstructure analyses

The NR morphology changes were recorded by a FESEM instrument (JEOL, JSM-7001FA) operated at 15 kV. XRD survey patterns of the specimens were obtained using an X-ray diffractometer (Rigaku, Tokyo, RINT2500HL) equipped with a Cu Kα source operated at 1.5406 Å at 50 kV; samples were scanned over the range $5° \leq 2\theta \leq 100°$. Peak fitting was performed in referenced to International Centre for Diffraction Data (ICDD) based no. 4-0831 for Zn, no. 36-1451 for ZnO, and no. 38-0385 for $Zn(OH)_2$. XPS data were collected using the JPS-9200 (JEOL) X-ray photoelectron spectrometer with a nominal energy resolution of 0.65 eV. Measurements were performed in an ultrahigh vacuum chamber with a base pressure less than 1.0×10^{-7} Pa. Spectra were acquired using a monochromated Al-Kα source ($h\nu = 1486.6$ eV) operated at 12 kV. Data were collected at room temperature.

4.3.5 Optical properties evaluation

The room-temperature PL spectra collected under excitation by a 325 nm He-Cd

continuous-wave laser operated at its maximum output of 16 mW. The PL spectra were recorded using an Acton SP2150 imaging spectrograph (Princeton Instruments) with a nominal resolution of 0.4 nm. Raman spectroscopy was carried out at room temperature using an XploRA PLUS (Horiba) with 532 nm laser excitation.

4.4 Results and discussion

4.4.1 ZnO nanorods characterization

In their bunched form, the fabricated ZnO NRs appear as nano-flowers (Figure 4.1a). The NRs were fabricated by submerged photosynthesis of crystallites (SPSC), which only utilizes light and pure neutral water, and does not require the incorporation of impurity precursors.[12] Using submerged liquid plasma[13] to create nanobumps to act as the NRs oxide seeds, I grew and controlled the NRs via SPSC by utilizing UV (λ = 365 nm) light. Samples irradiated for 24 h (UV_{24h}) and 72 h (UV_{72h}) exhibited distinct finely tapered and capped morphologies, respectively, compared with the other samples (Figure 4.1a and Figure 4.4).

During SPSC, the NRs size increased from approximately 250 nm (tapered) to 500 nm (capped) in diameter. NRs will grow longer by effect of UV light while the diameter increased (section 4.4.2 and Figure 4.2). Typical NR length after UV72h is ~1 μm. Then, a 24 h re-irradiation of UV_{72h} NRs in fresh ultrapure water reconstructed the

apical shape into tapered-end ($UV_{72h+24h}$ tapered NRs). Room-temperature photoluminescence (PL)

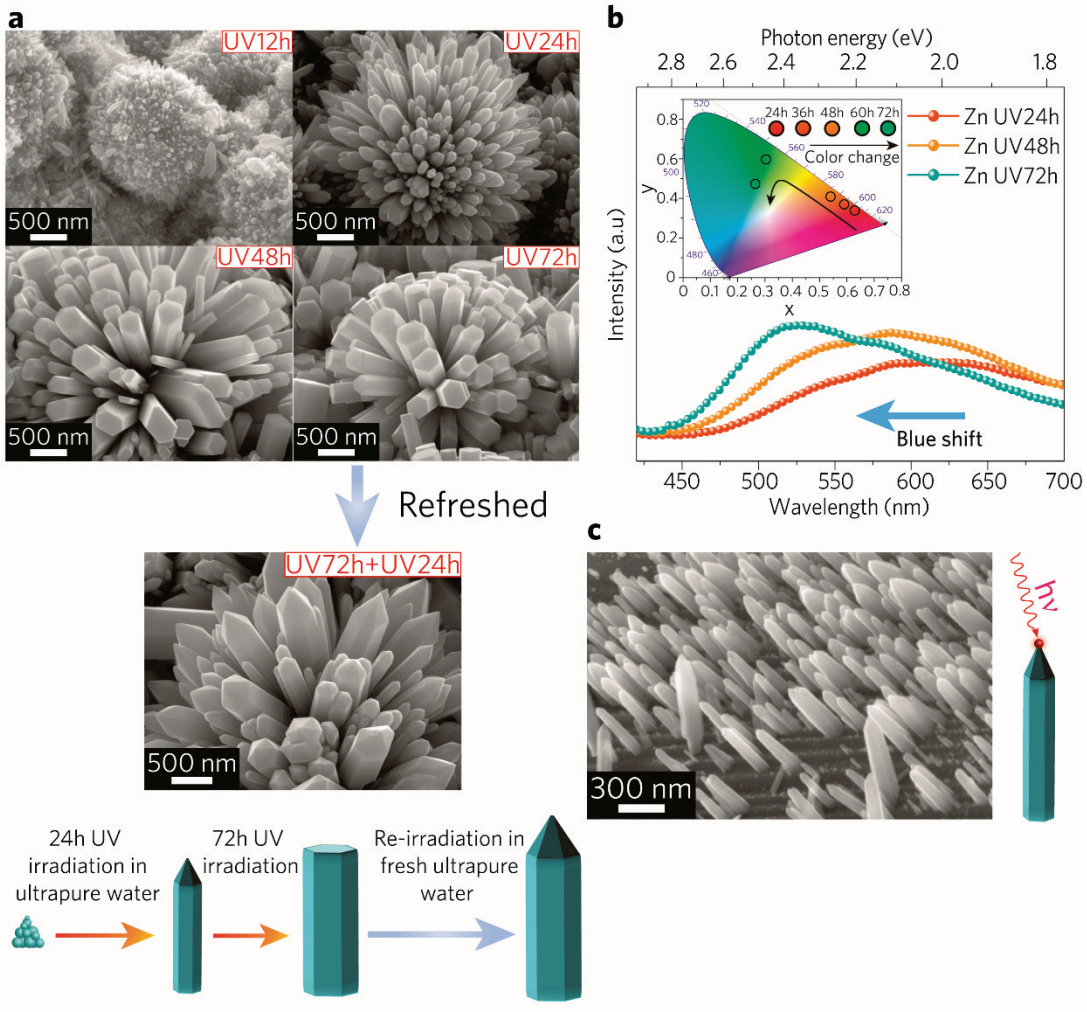

Figure 4.1 - Apical growth control of NRs and their opto-electronic tuning via SPSC. (a) Field-emission scanning electron microscopy (FESEM) images of continuous UV_{72h} irradiation in ultrapure water, demonstrating the construction of the NRs in shapes ranging from tapered to capped. Capped NRs were reconstructed into tapered ends after UV_{24h} re-irradiation in fresh ultrapure water. A schematic of apical growth control is also shown below the $UV_{72h+24h}$ image. (b) Blue-shift in PL peak emission from UV_{24h} to UV_{72h} (24 h intervals) with an inset color chromaticity diagram showing the color change from red to greenish-blue (UV 12 h interval). (c) ZnO growth NRs array patterning on the protruded inline surface prepared by focused ion beam (FIB). On the far right is a schematic of light interaction at the tip of a NR, resulting in a hotspot area where the photoinduced radical reactions mainly occur.

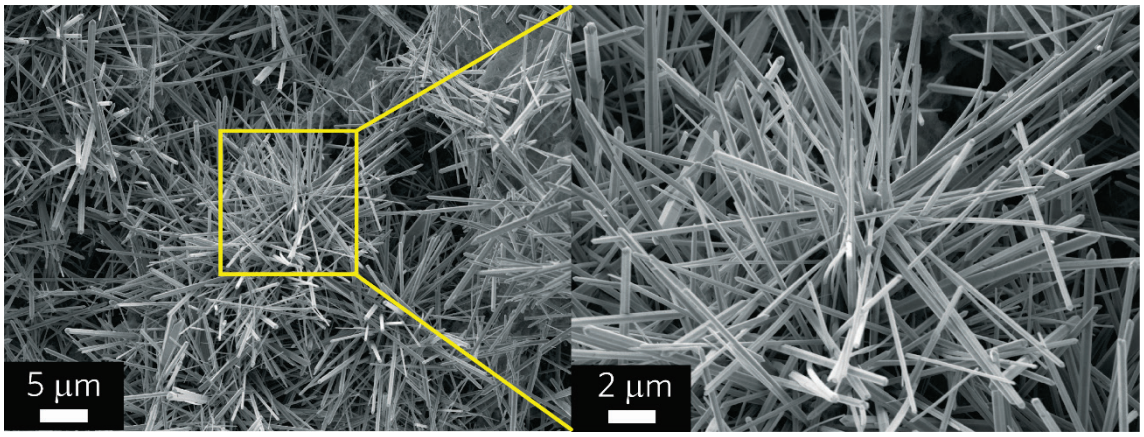

Figure 4.2 – FESEM images of plasma-treated Zn surface after underwent 21 days of UV irradiation.

analysis dictated a blue-shift in the visible light range, with the tapered NRs showing a PL peak at 605 nm, whereas the capped NRs exhibited a PL peak at 523 nm (Figure 4.1b). The 523 nm peak shifted to 587 nm in $UV_{72h+24h}$ tapered NRs (Figure 4.4). Although the dominant bulk NRs on the surface may be the origin of the optical excitation behavior, as been discussed in Chapter 3, the apical morphology manifested essential properties to consider; the photoinduced water splitting process attributed to the protruding surface effect.[12] While maintaining SPSC concept, it is also feasible to control the protruding surface using other than submerged liquid plasma in order to realize NRs array patterning (Figure 4.1c).

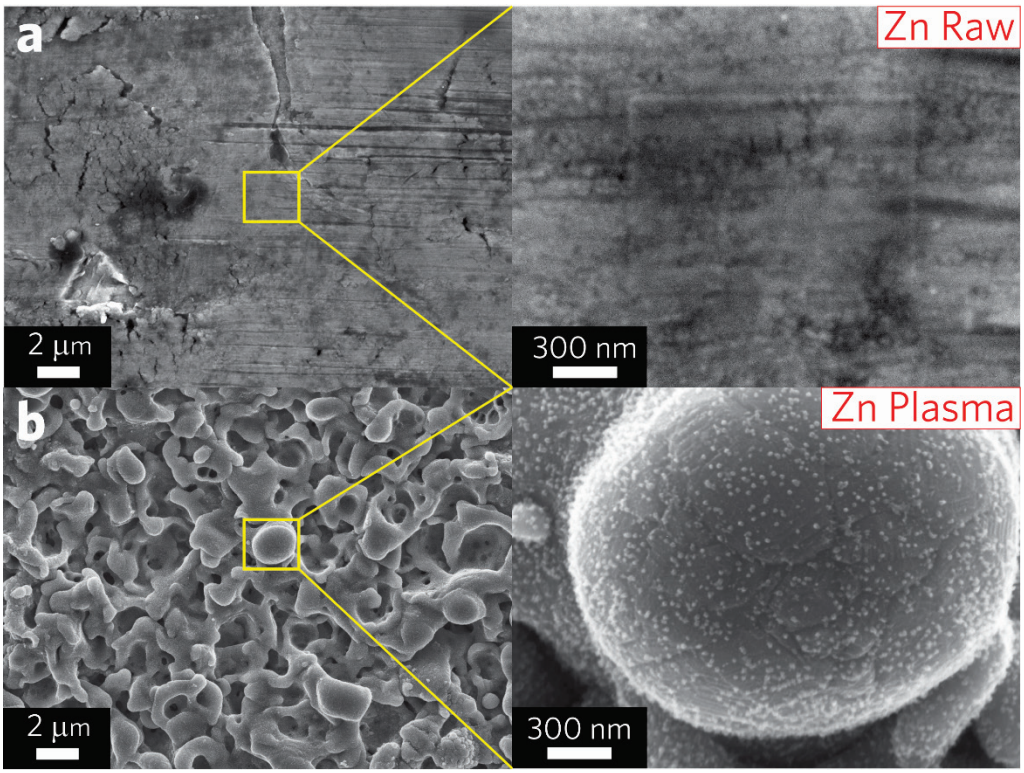

Figure 4.3 - FESEM images of raw and plasma-treated Zn specimen surface. Right panel displays their respective magnified images. (a) Raw Zn. A roughly flat surface can be observed. (b) Plasma-treated Zn. An average 1µm protruding surface with localized ZnO nanoparticles (nanobumps) can be observed. Their average size is less than 30 nm.

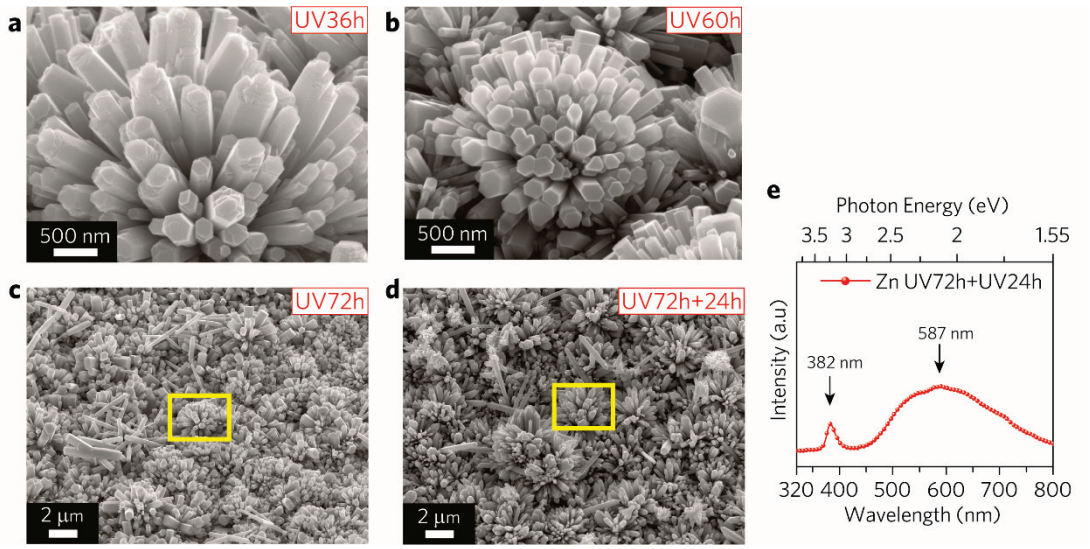

Figure 4.4 - FESEM images of ZnO NRs. (a) UV_{36h} NRs; the NRs have corroded surfaces due to the dissolution of Zn. (b) UV_{60h} NRs with the capped shape. (c-d) Low magnification images of UV_{72h} capped NRs and $UV_{72h+24h}$ tapered NRs, respectively. The yellow rectangle marks the recorded images

displayed in Figure 1a. (e) Room-temperature photoluminescence spectra of $UV_{72h+24h}$ tapered NRs.

4.4.2 UV light effect during SPSC

The optical excitation behavior of ZnO NRs is known to be caused by intrinsic point defects and surface defects such as oxygen vacancies, anti-site defects, and hydroxyl groups incorporated into the crystal lattice.[14-17] In particular, the incorporation rate of OH^- into a ZnO crystal determines the tapered or capped morphology, which will eventually influence the NRs native defects. On the other hand, deposition (crystallization) and dissolution of ZnO favored by the photochemical process are responsible for the reaction equilibria. We did study the NRs growth behavior under dark and UV light illumination conditions (Figure 4.5).

Here, Zn metal itself can dissolute in water both under dark (hydrothermal) and UV illumination (photochemical + hydrothermal) conditions to give rise to the following reaction:

$$Zn + H_2O \rightarrow Zn^{2+} + 2OH^- + H_2 \quad (4.1)$$

However, on the basis of my observation, NRs formation under dark condition is relatively low compare with UV illuminated condition (Figure 4.5). Rather, I observed $Zn(OH)_2$ as dominant formation under dark condition. It is distinguishable as dark fibrous film on the specimen surface (Figure 4.5a) and detected by XPS analysis.

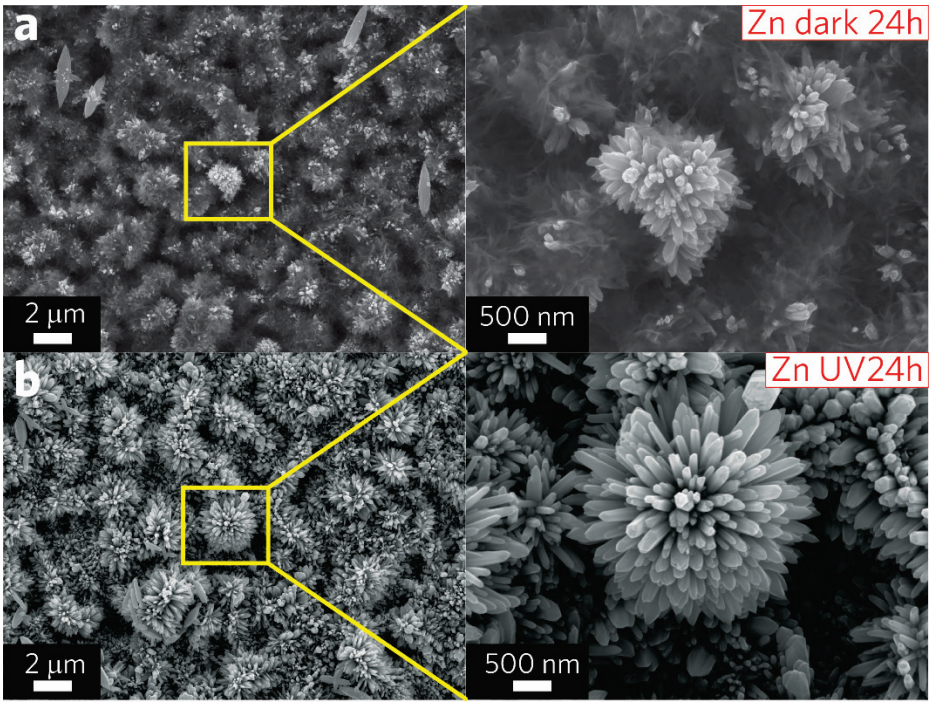

Figure 4.5 - FESEM images of plasma-treated Zn specimens after been submerged in pure water for 24 h. (a) Dark condition without UV illumination. (b) UV illuminated condition for SPSC. The right panel displays the magnified images.

The effect of UV illumination towards the NRs formation is clearly evidenced by Figure 4.5b; the protruded surface is covered by long and fine tapered shape NRs, which is the main focus in this chapter. I deduce that UV light induces the apical growth of NRs.

In concern with $Zn(OH)_2$ formation (Figure 4.5a), it is realized by Zn^{2+} reaction with OH^- (equation (4.2)) and do not dehydrate to form ZnO (equation (4.3)) because of UV light absence.

$$Zn^{2+} + 2OH^- \rightarrow Zn(OH)_2 \quad (4.2)$$

$$Zn(OH)_2 \rightarrow ZnO + H_2O \quad (4.3)$$

In detail, the role of UV light and the equation (4.1)[12] has been discussed in

Chapter 3. UV light gives photo-induced water splitting process. The result is OH radical production, which detected by monitoring the bleaching of *p*-nitrosodimethylaniline (PNDA). OH radical react with hydrated electron (e^-_{aq}) to form OH^- at the hill of nanobump surface. This also permits Zn dissolution.[18] Subsequently, re-precipitation of metal oxide and dehydration of $Zn(OH)_2$ (equation (4.3)) occur and contribute to the re-growth of ZnO NRs with apical growth characteristic.

Hence, OH^- production by photo-induced water splitting at nanobumps result in enhancement of local alkaline environment. Together with induced apical growth, aggregation and recrystallization of ZnO nanoparticles (superimposed hydrothermal reactions)[12] occur to generate ZnO NRs.

4.4.3 OH^- detection by pH-T monitoring and XPS analysis

As been discussed in section 4.4.2, the role of UV light during SPSC is to enhance photocorrosion of ZnO and induce apical growth of the NRs based on the formation of $Zn(OH)_2$. Here, pH-T monitoring (Figure 4.6a) allowed the tracking of the entire process. A high pH (~10) and temperature at ~40 °C enabled a high concentration of Zn^{2+} at UV_{3h}, which coordinated with OH^- to form $Zn(OH)_2$[12] until UV_{12h}. At UV_{12h}, only small NRs were grown on the specimen (Figure 4.1a). Tapered NRs formed at UV_{24h} because of a rich supply of OH^- from H_2O. In pure neutral water, OH^- is generated near the tip of

a nanobump through the reaction of a hydroxyl radical (OH) with a hydrated electron (e^-_{aq}). Consequently, a locally alkaline region is established near the tip.[12] This behavior pushes the reaction toward the deposition of ZnO through the dehydration of $Zn(OH)_2$ and imparts it with apical growth characteristics.[18] At this stage, I observed a weight increase (~100 μg/cm^2) of the specimens. Additionally, bromothymol blue (BTB) solution changed color from yellow to blue when Zn specimens initially immersed into the water, indicating the water pH was greater than 7.6. Thus, the initial SPSC process to yield ZnO was completed at UV_{24h} according to the transformation: Zn → $Zn(OH)_2$ → ZnO.

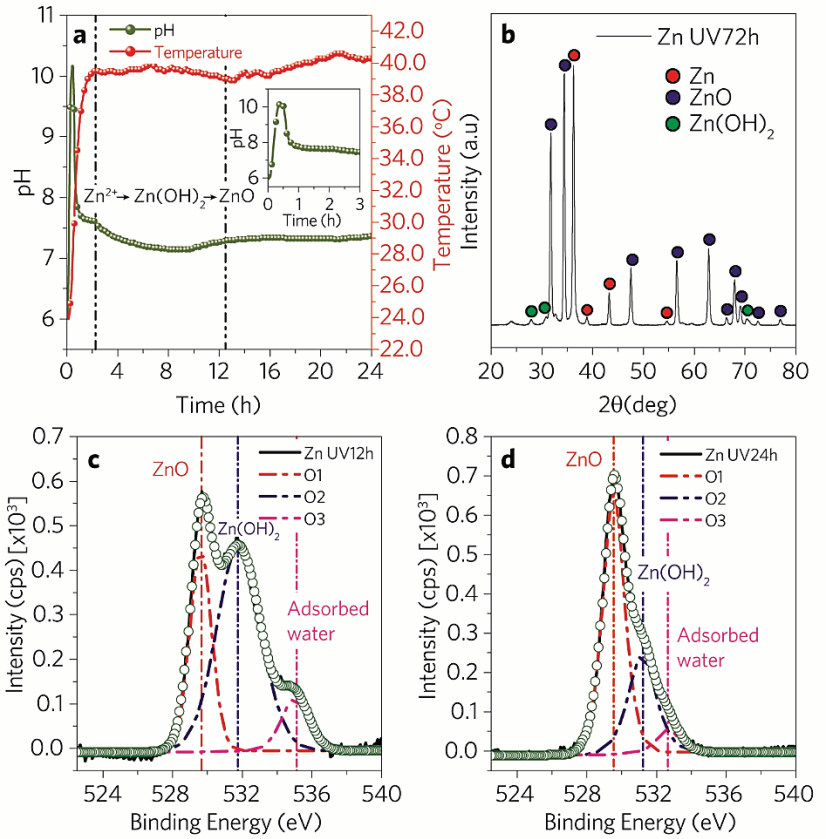

Figure 4.6 - SPSC photoreaction mechanism and surface structure analysis. (a) pH-T graph of UV_{24h} SPSC of ZnO NRs. The inset is a magnified view of the pH change in the ultrapure water over a period of 3 h. (b) XRD patterns of UV_{72h} specimen. (c-d) XPS O 1*s* peak of Zn UV_{12h} and UV_{24h} specimens deconvoluted into three Gaussian-Lorentzian peaks.

The OH^- supply decreased upon longer UV irradiation, resulting in capped NRs. Notably, ZnO deposition and dissolution occurred simultaneously to sustain the equilibrium. Therefore, $Zn(OH)_2$ was still detectable in highly crystalline wurtzite ZnO NRs via X-ray diffraction (XRD) analysis (Figure 4.6b). I used X-ray photoelectron spectroscopy (XPS) (Figure 4.6c-d) to quantify the O/Zn ratio (Table 4.1). The quantification was performed using the broad O 1*s* spectra deconvoluted into ZnO, $Zn(OH)_2$, and adsorbed water peaks (see also Figure 4.7).

Table 4.1 - Quantitative XPS analysis of ZnO NRs on the basis of their O 1*s* spectra. The O/Zn ratio was calculated by integrating the ZnO component area with total of their O 1*s* components.

NRs specimen	O 1*s* peak components						O/Zn ratio
	ZnO		$Zn(OH)_2$		Adsorbed water		
	Peak (eV)	FWHM	Peak (eV)	FWHM	Peak (eV)	FWHM	
UV_{12h}	529.6	0.7	531.8	1.5	535.0	0.9	0.59
UV_{24h}	529.5	0.7	531.2	1.0	532.7	0.8	0.87
UV_{36h}	529.6	0.7	531.0	1.3	535.9	1.1	0.74
UV_{48h}	529.5	0.7	531.2	1.0	532.7	0.8	0.77
UV_{60h}	529.6	0.7	531.2	0.9	532.4	0.7	0.89
UV_{72h}	529.7	0.8	531.3	0.8	532.5	0.8	0.99

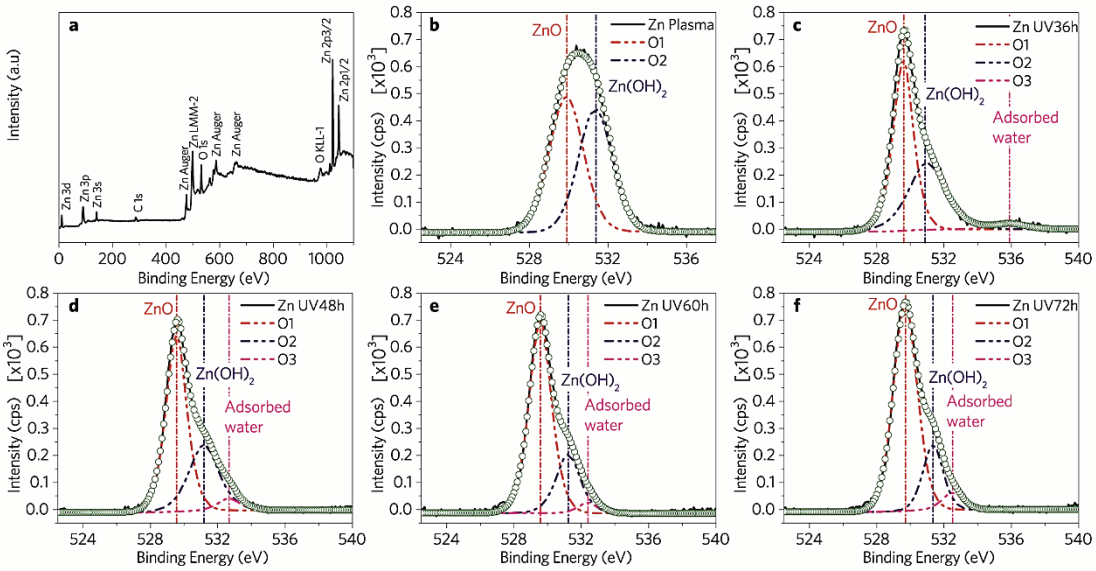

Figure 4.7 - (a) Typical XPS wide survey spectrum of the Zn SPSC specimens. (b) Zn Plasma UV_{0h}. (c) Zn UV_{36h}. (d) Zn UV_{48h}. (e) Zn UV_{60h}. (f) Zn UV_{72h}.

A drastic decrease in the $Zn(OH)_2$ peak after UV_{12h} is in agreement with NRs formation shown in Figure 4.1a. As a result of the continuous deposition and dissolution processes, the O/Zn ratio inconsistently increased. Nevertheless, I deduced that UV_{72h}

resulted in ZnO with a stoichiometric ratio of ~1.

4.4.4 Optical properties based on PL and Raman results

The O/Zn ratio change governed defect conversion in the NRs. The results of room-temperature PL measurements under 325 nm He-Cd laser excitation are indeed consistent with the XPS results. The blue-shift in the PL peaks from 605 nm to 523 nm occurs gradually as a function of the UV irradiation time (Figure 4.8a). The 605 nm (2.05 eV) peak is attributed to ZnO oxygen vacancies (V_o).[19] The 523 nm (2.37 eV) peak is attributed to oxygen anti-site defects.[20] V_o acted as non-radiative centers to suppress the band edge emission[21] and this is particularly occur at the tip of NRs. As the defect type changed, i.e., the V_o disappeared, the ZnO crystal quality is improved. Subsequently, the band edge emission is enhanced. This is in agreement with our XPS analysis result, which UV_{72h} NRs has stoichiometry ratio of ~1 (Table 4.1) and strongest band edge emission intensity (Figure 4.8a). All the ZnO NRs exhibited a NBE emission at 380 ± 2 nm (3.3 eV), indicating that the bandgap energy for direct transition was unchanged. In the case of raw and plasma-treated specimens (Figure 4.3), no obvious emission on visible light range was observed. In addition, Raman spectroscopy results also revealed that the V_o peak intensity at 562 cm^{-1} (Figure 4.8b) decreased with increasing UV irradiation time. The Raman spectra of all of the NRs exhibit wurtzite ZnO Raman modes at 326 cm^{-1}, 371

cm^{-1}, 433 cm^{-1}, 562 cm^{-1}, 657 cm^{-1}, and 1111 cm^{-1}.[22, 23]

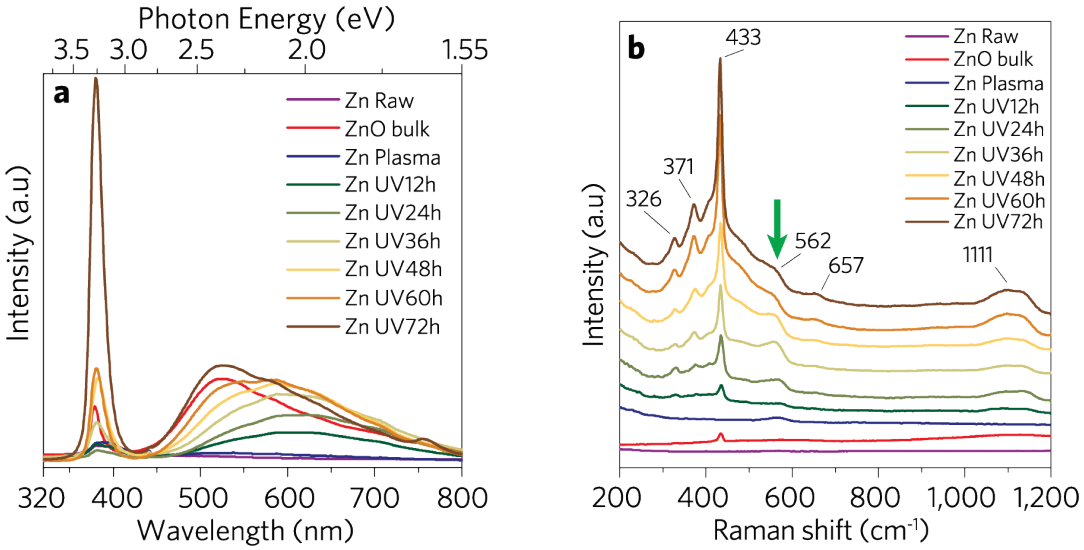

Figure 4.8 - Optical properties of fabricated ZnO NRs. (a) Room-temperature PL spectra of ZnO specimens. All specimens exhibited NBE emission at 380 ± 2 nm. A blue-shift occurred from 605 nm to 523 nm. The 523 nm peak matches the peak of a procured ZnO bulk specimen grown in the <001> direction. (b) Raman spectra of the Zn SPSC specimens.

4.4.5 Oxygen vacancy study by STEM observation

I anticipated that SPSC reaction determinant in the inherent opto-electrical hotspot could be understood by V_o at the tip of NRs. PL results are reliably apprised of the V_o existence because of its high energy resolution (< 1 meV). However, it is lack of spatial resolution versus the STEM/STEM-EELS technique, which can reach sub-angstrom resolution. On the basis of high-resolution annular-bright-field STEM (ABF-STEM) observations, I detected locally oxygen-deficient atomic columns near the tapered NR tip-edge (Figure 4.9). As the NR in Figure 4.9 was subjected to 300 kV

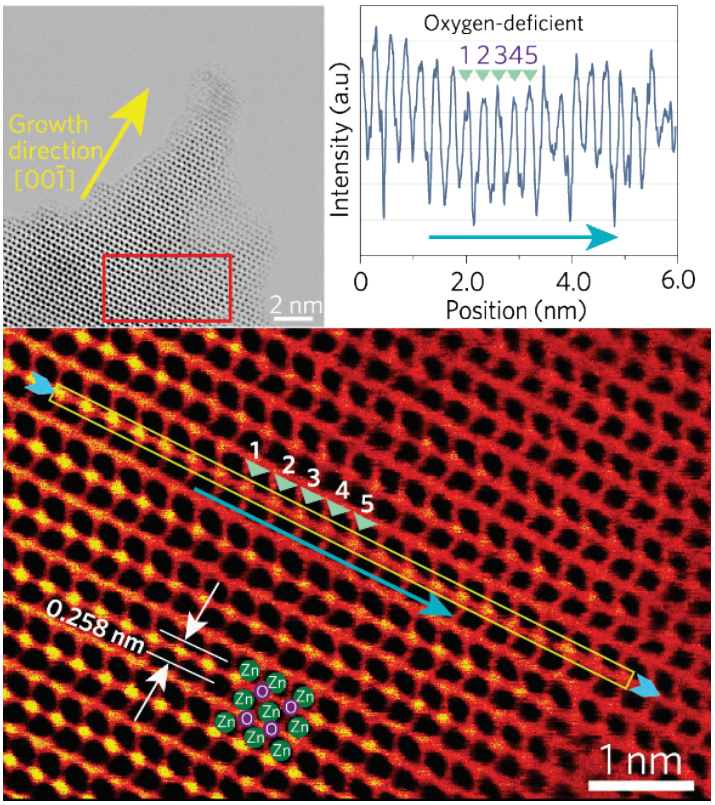

Figure 4.9 - High-resolution ABF-STEM image of a tapered NR tip-edge. The red rectangle indicates the magnified atomic image below, where black and yellow dots are Zn and O atomic columns, respectively. The right upper graph is the line density plot over the O column of the magnified area. The oxygen-deficient region is indicated by numbers 1-5.

STEM-EELS mapping, I manage to measure its thickness by the log-ratio method using Digital Micrograph (TM) (GATAN) software.[24] As a result, the estimated thickness is 8.29 nm. I am aware of the local thickness variation on the tip of the nanorod. Therefore I also tracked oxygen-deficient atomic columns in the interior part (Figure 4.10b-c) excluding the thin tip-edge region (Figure 4.10a). Energy dispersive X-ray spectroscopy (EDS) mapping in STEM also revealed that the tapered NR tip-edge was oxygen-deficient compared with the capped NR (Figure 4.11). On the basis of line profile plot, oxygen-deficient atomic columns were also detected in interior part of the tip-edge.

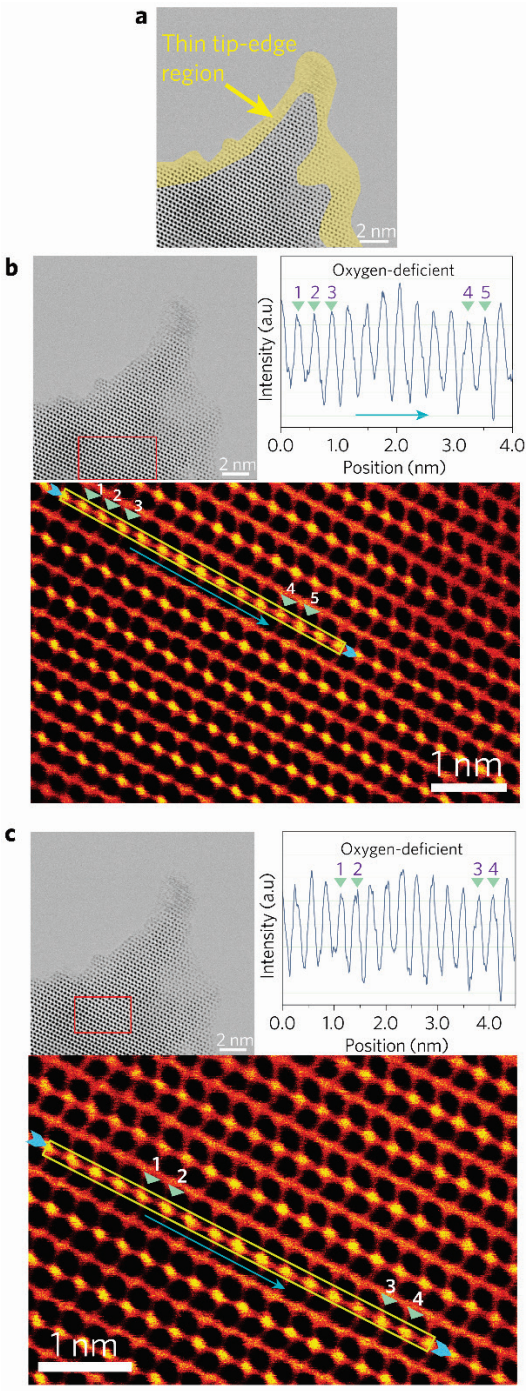

Figure 4.10 - Detection of oxygen-deficient columns in high resolution ABF-STEM image of tapered ZnO NR. (a) A yellow mask highlight the thin tip-edge region near vacuum. The region is excluded from oxygen-deficient tracking. (b-c) Red rectangle on the interior part of nanorod highlight the magnified image at the bottom. Line profile was traced and plotted on the right upper graph for oxygen-deficient columns detection, as indicated by no. 1-4/5.

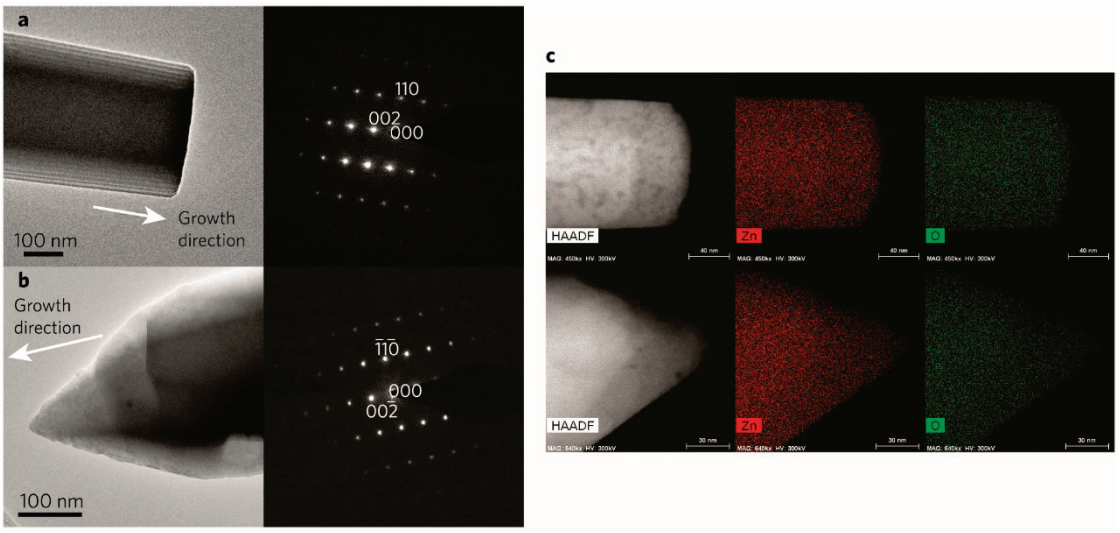

Figure 4.11 - (a-b) TEM micrographs of capped and tapered NRs. The right panel is their selected-area electron diffraction (SAED) pattern obtained along the $[1\bar{1}0]$ direction. The growth direction is along the c-axis with a $(00\bar{1})$ O-terminated polar surface. (c) 300 kV STEM-EDS elemental mapping images of the capped (top) and tapered (bottom) tips. The atomic percentage [at. %] ratio of O: Zn is 49.4: 50.6 and 42.1:57.9 for capped and tapered tips, respectively.

4.4.6 NRs opto-electrical properties study by STEM-VEELS

Taking advantage in its attainable high spatial resolution, I conducted valence EELS (VEELS), i.e., low energy loss analysis, on the tapered NR. It is essential in order to give correspondence with the PL results.

The EELS measurements were carried out using a double-Cs-corrected transmission electron microscope (FEI, Titan Cubed) equipped with a Schottky electron source and operated in STEM mode. The STEM was operated at monochromated 60 kV for all measurements. A Wien-type monochromator was used to disperse the electron beam energy. A Gatan Quantum EELS detector was used for the EEL spectroscopy. The

energy resolution achieved in the measurements was 0.1 eV, with a spectral dispersion of 0.01 eV per channel at a convergence semi angle of 13 mrad and a collection semi angle of 8.447 mrad. When probing the tapered NR from the interior to its tip-edge (Figure 4.12), the VEEL spectra changed shape in a systematic way. KKA routines were performed on the spectra[24-28] to obtain the optical properties.

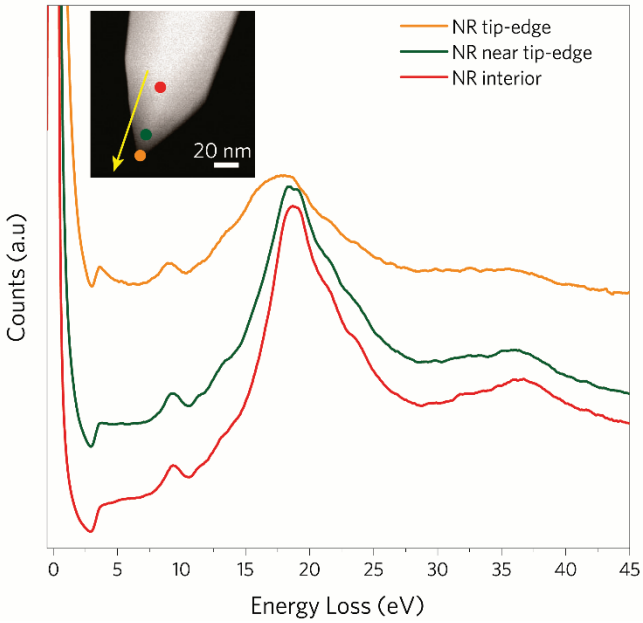

Figure 4.12 - A series of raw STEM-EEL spectra of tapered ZnO NRs acquired from the interior to the tip-edge, with the colored circles indicating the positions in the corresponding HAADF image of the NR (inset).

The pre-analyses of EEL spectra were carried out using the Digital Micrograph (TM) (GATAN) software as follows:

1. Calibration of the EEL spectra (re-zero the ZLP).

2. Removal of the ZLP peak using the fitted logarithm tail method.

3. Removal of the plural scattering of spectra using Fourier log deconvolution.

KKA were performed on the deconvoluted EEL spectra to obtain the optical properties; the convergence semi-angle was 13 mrad, the collection semi-angle was 8.447 mrad, and the optical refractive index of ZnO was 1.922.[25]

ELF information was inherited from the acquired EEL spectra. The ELF can be described as

$$\mathrm{Im}\left(\frac{-1}{\varepsilon}\right)=\frac{\varepsilon_2}{\varepsilon_1^2+\varepsilon_2^2} \tag{4.4}$$

Here, a Kramers-Kronig transformation is used to derive the function Re(1/ε) from Im(-1/ε):

$$\mathrm{Re}\left[\frac{1}{\varepsilon(E)}\right]=1-\frac{2}{\pi}\mathcal{P}\int_0^\infty \mathrm{Im}\left[\frac{-1}{\varepsilon(E')}\right]\frac{E'dE'}{E'^2-E^2} \tag{4.5}$$

After evaluating Re(1/ε(E)), we obtain the dielectric function from

$$\varepsilon(E)=\varepsilon_1(E)+i\varepsilon_2(E)=\frac{\mathrm{Re}\left[1/\varepsilon(\mathrm{E})\right]+i\,\mathrm{Im}\left[-1/\varepsilon(\mathrm{E})\right]}{\left\{\mathrm{Re}\left[1/\varepsilon(E)\right]\right\}^2+\left\{\mathrm{Im}\left[-1/\varepsilon(E)\right]\right\}^2} \tag{4.6}$$

Knowing the dielectric function, I calculated the refractive index and the optical absorption coefficient α:

Refractive index

$$\begin{aligned}\tilde{n}&=\sqrt{\varepsilon}=n+i\kappa\\ \tilde{n}^2&=n^2-\kappa^2+2in\kappa\end{aligned} \tag{4.7}$$

Thus,

$$n = \sqrt{\frac{1}{2}\left(\varepsilon_1 + \sqrt{\varepsilon_1^2 + \varepsilon_2^2}\right)}$$
$$\kappa = \sqrt{\frac{1}{2}\left(\sqrt{\varepsilon_1^2 + \varepsilon_2^2} - \varepsilon_1\right)} \tag{4.8}$$

Optical absorption coefficient

$$\alpha = \frac{2\kappa\omega}{c} = \frac{E}{\hbar c}\sqrt{2\sqrt{\varepsilon_1^2 + \varepsilon_2^2} - 2\varepsilon_1} \tag{4.9}$$

From the KKA results, the imaginary part, Im(ε), of the complex dielectric function ($\varepsilon = \varepsilon_1 + i\varepsilon_2$) can be translated to the energy absorption in the NR. Compared with interior part (Figure 4.13a), the characteristic of having V_o on the tip-edge of the NR resulted in about two times increase of ε_2 on the NBE (Figure 4.13b).

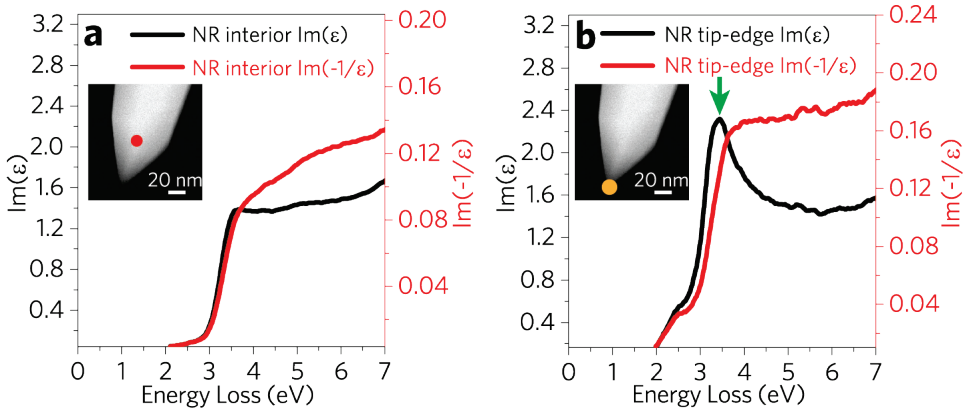

Figure 4.13 - (a-b) The imaginary part, Im(ε), of the dielectric function and energy-loss function (ELF, Im(-1/ε)) calculated by KKA of 60 kV monochromated STEM-VEEL point spectra obtained for the tapered NR interior and tip-edge parts.

On the basis of equations (4.8) – (4.9), KKA results for refractive index and optical absorption coefficient α (Figure 4.14) also highlighted the tapered NR tip-edge high-electron-density absorption at the NBE region.

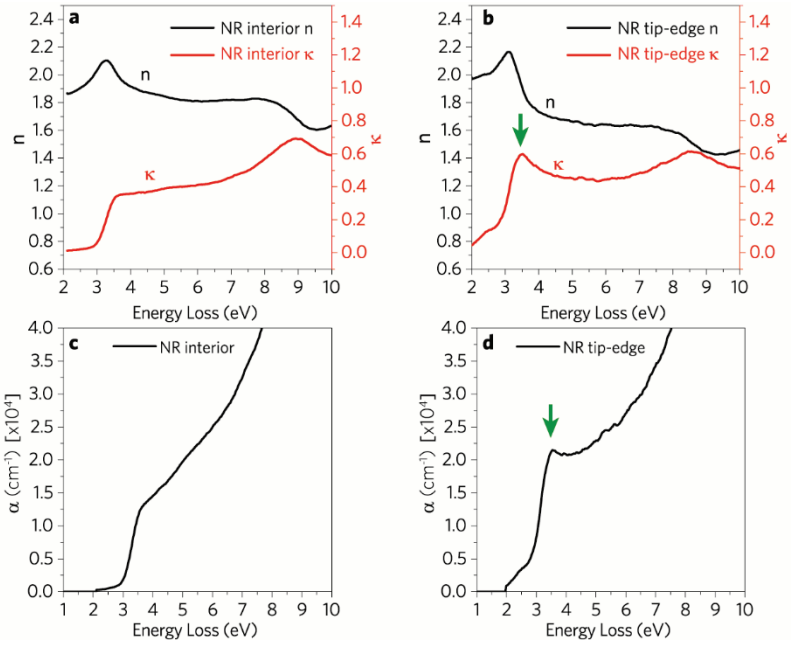

Figure 4.14 - Experimental evaluation by KKA. (a-b) Refractive index corresponding to the interior and tip-edge parts, respectively. (c-d) α of the interior and tapered parts, respectively. Both κ and α of the tip-edge displayed a substantial peak at 3.3 eV (NBE), as indicated by the green arrow.

Therefore, the optical absorption confined at the tip-edge (Figure 4.14) to create the opto-electrical hotspot and subsequently enhanced the SPSC apical growth.

4.4.7 NRs opto-electrical properties study by ab initio calculation

To further confirm the experimental results showing the change in the opto-electrical properties of the oxygen-deficient NRs, I calculated the energy band structures using *ab initio* simulations.[29-31] Firstly, I constructed bulk ZnO and ZnO + V_o models, as

shown in Figure 4.15a. Then, together with optical properties evaluation of the crystals, CASTEP code[32] was utilized for the simulation.

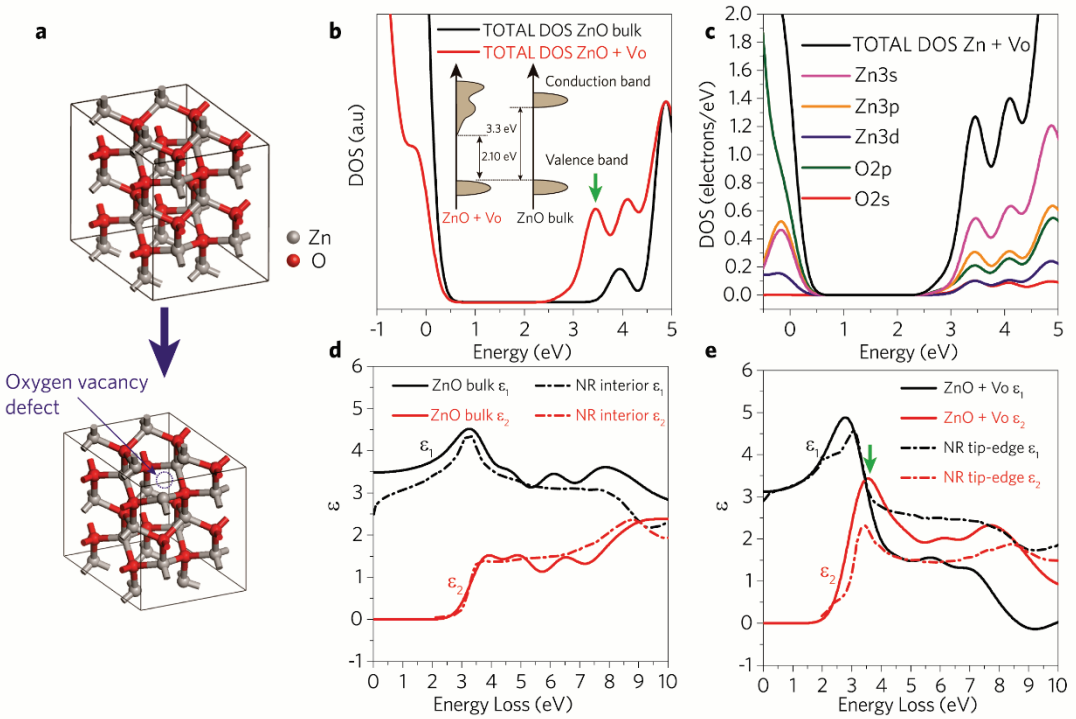

Figure 4.15 - Comparison of the opto-electrical experimental results with *ab initio* energy-band structural calculations assuming oxygen-deficient ZnO. (a) Schematic for modeling ZnO bulk and ZnO + V_o defects. (b) Calculated total density of state (DOS) of ZnO bulk and ZnO + V_o. The inset is a schematic comparing the DOS for the two states. The valence band maximum energy is taken to be zero. The green arrow points to the V_o energy band in the crystal. (c) The decomposition of ZnO + V_o total DOS into partial DOS of the Zn and O orbitals. (d-e) Dielectric function comparison between experimental KKA calculation results based on EELS data and the *ab initio* calculation. Dielectric function of tapered NR interior and tip-edge match with ZnO bulk and ZnO + V_o, respectively.

In CASTEP code, a hexagonal ZnO crystal with lattice parameters $a = b = 0.3249$ nm, $c = 0.5205$ nm was modeled, as in Figure 4.15a. In the perfect ZnO bulk, the hexagonal calculation cell has 16 Zn atoms and 16 O atoms; ZnO + V_o has 16 Zn atoms and 15 O atoms. The model optimizations were performed using the ultrasoft

pseudopotential plane-wave method. The generalized gradient approximation (GGA) of Perdew-Burke-Ernzerhof (PBE) was then adopted to describe the exchange and correlation (XC).

I used the scissors operator[29] to give the best approximation of the optical properties from EELS measurements. The approximation was implemented by fitting the ELF spectra. As a result, I employed the scissors operator value of 2.37 eV to the ZnO bulk and 0.97 eV to ZnO + V_o to shift the calculated conduction bands upward (Figure 4.16a-b).

To calculate the optical properties, integrations in the Brillouin zone (equation (4.10)) were performed using special k points generated with a 4 × 4 × 2 mesh parameters grid. Polarization was set to the [100] direction, and periodic boundary conditions were applied in all directions of the lattice parameters.

$$\varepsilon = \varepsilon_1 + i\varepsilon_2$$
$$\varepsilon_2(\omega) = \frac{4\pi^2 e^2}{m_o^2 \omega^2} \sum_{v,c} \int_{BZ} \frac{2d^3\boldsymbol{k}}{(2\pi)^3} \left| \boldsymbol{u} \cdot \boldsymbol{M}_{cv} \right|^2 \delta(\mathrm{E}_k^c - \mathrm{E}_k^v - \mathrm{E})$$
where (4.10)
$$\boldsymbol{u} \cdot \boldsymbol{M}_{cv} = \left\langle \Psi_k^c \left| \boldsymbol{u} \cdot \boldsymbol{p} \right| \Psi_k^v \right\rangle$$
$$= \boldsymbol{u} \cdot \int_{cry.vol} d^3\boldsymbol{r} \Psi_k^{c\dagger} \left(-i\hbar\nabla \right) \Psi_k^v$$

Here, $\boldsymbol{u}$ is the unit vector, which defines the polarization of the incident electromagnetic field with the incident photon energy, $E = \hbar\omega$; e and m_0 are the charge

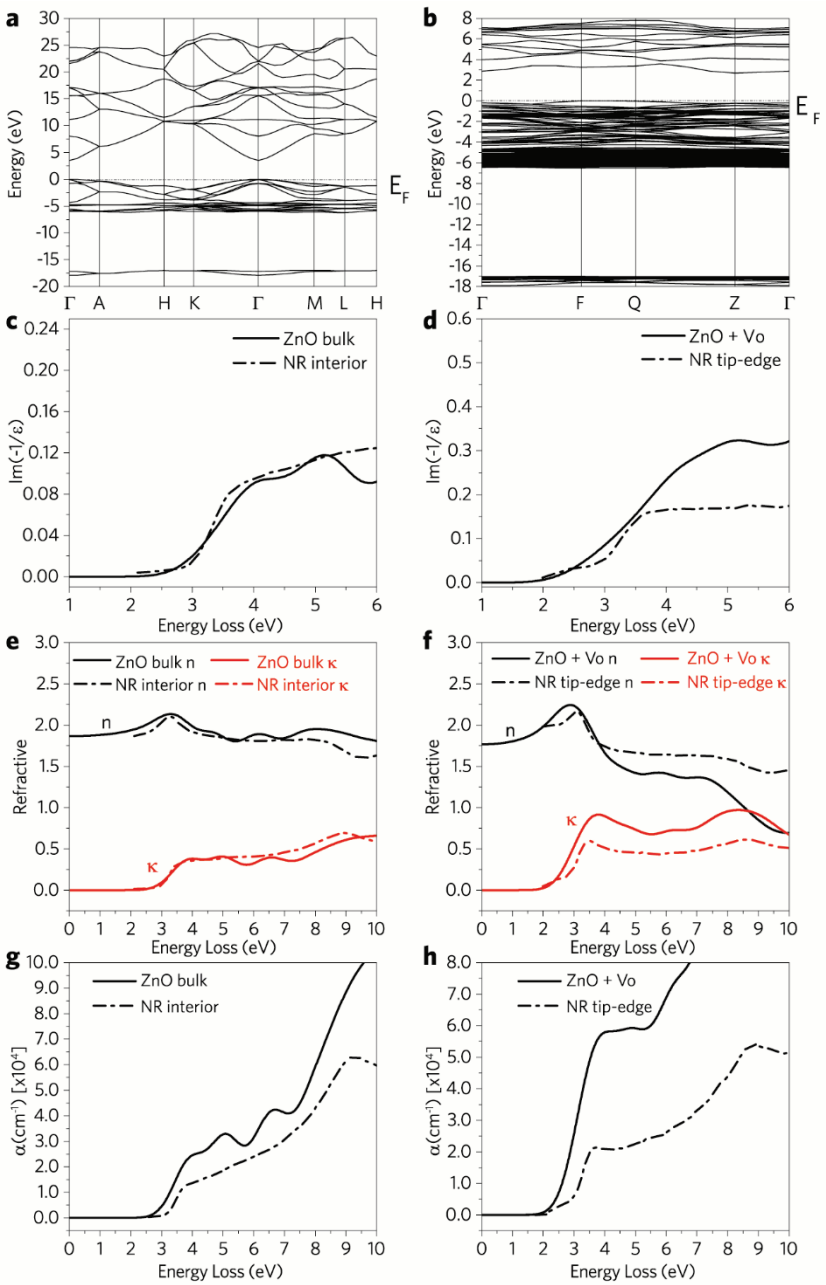

Figure 4.16 - ZnO energy band structure and optical properties comparison result. (a-b) *Ab initio* calculation for energy band structure of ZnO bulk and ZnO + V_o, respectively. (c-d) ELF comparison: the solid line is the *ab initio* calculation result, and the dash line is the experimental result. (e-f) Refractive comparison: the solid line is the *ab initio* calculation result, and the dashed line is the experimental result. (g-h) α comparison: the solid line is the *ab initio* calculation result, and the dash line is the experimental result.

and mass of a bare electron, respectively. Ψ_k^c and Ψ_k^v are the unoccupied and occupied state eigenfunctions of the system, respectively, and E_k^c and E_k^v are their corresponding

band energies. The derivation of ε_1 is performed using the Kramers-Kronig dispersion relation[31] on ε_2.

Figure 4.15b shows the calculated DOS of the two ZnO models in Figure 4.15a. A mid-gap state at approximately 2.10 eV appears in the ZnO + V_o compared with the bulk ZnO. On the basis of its partial DOS, this mid-gap state is due to Zn 3*s* and Zn 3*p* orbitals (Figure 4.15c). The optical properties were then calculated and compared to the experimental results. Both model simulations matched well with the experimentally measured dielectric function of the tapered NR interior and tip-edge (Figure 4.15d-e). In the plot of the ε_2 of ZnO + V_o, a significant peak is observed at ~3.3 eV, as indicated by the green arrow (Figure 4.15e). The intra-band energy then shifted from a direct transition of 3.3 eV (NBE of ZnO bulk) to an indirect transition of 2.10 eV (V_o) (Figure 4.15b).

In addition to the dielectric function results, the calculation results for other optical properties (e.g., refractive index and optical absorption) also matched well with the experimental results (Figure 4.16). In particular, a similar peak at 3.3 eV (Figure 4.15e) also appears at optical extinction coefficient κ and optical absorption coefficient α (Figure 4.16).

As the 523 nm (2.37 eV) peak in the PL emission observed on capped NR (UV_{72h}) and procured ZnO bulk specimen (Figure 4.8a) was related to oxygen anti-site defects

(O_{Zn}),[20] I performed *ab initio* calculations as described for ZnO + V_o. I modeled the ZnO crystal to have Zn-O sites exchanged (Figure 4.17a). ELF fitting gave a scissors operator value of 1.604 eV to shift the conduction band upward (Figure 4.17b). The partial DOS (Figure 4.17c) was then generated to enable deriving the transitions corresponding to peaks appearing in the EELS. Here, the intraband energy shifted from a direct transition of 3.3 eV (NBE) to an indirect transition of 2.47 eV.

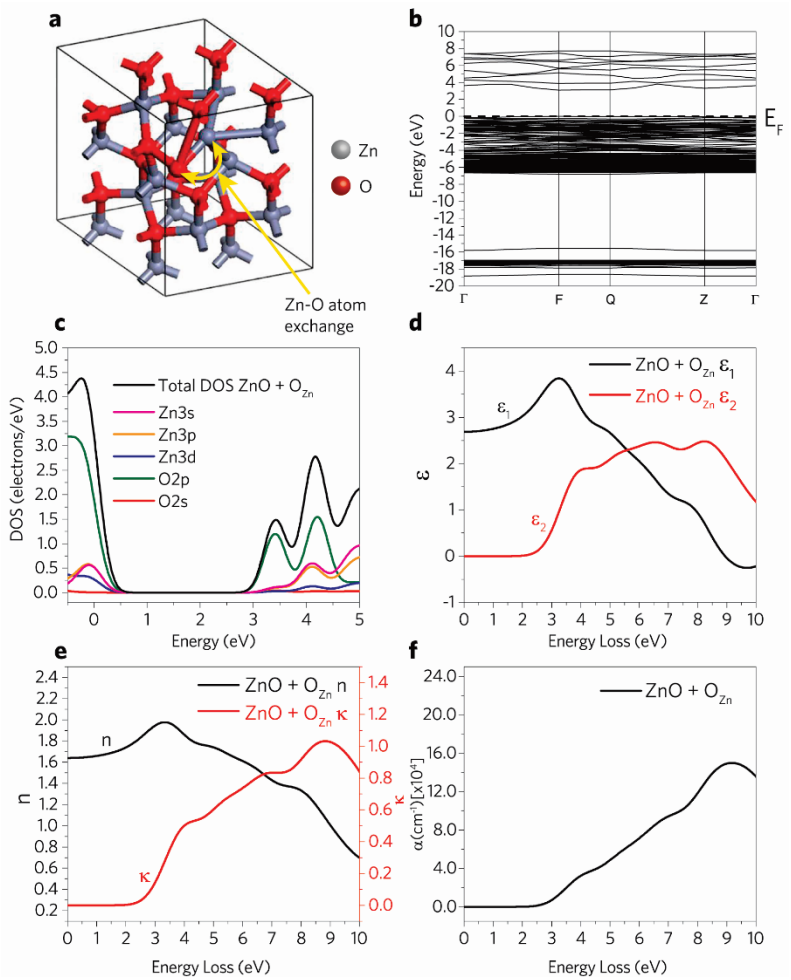

Figure 4.17 - *Ab initio* calculation result for ZnO + O_{Zn}. (a) Schematic for modeling ZnO + O_{Zn}. (b) Simulated band structure. (c) Total DOS of ZnO + O_{Zn} with partial DOS at the Zn and O orbitals. (d) Dielectric function. (e) Refractive index. (f) Optical absorption coefficient.

The calculated optical properties of our ZnO + O_{Zn} crystal model (Figure 4.17d-f) were compared to those of the experimental tapered NR interior. However, the model optical properties approximation did not match the experimental results. Thus, I concluded that the 2.47 eV interband transition corresponds to the 523 nm peak.

Herein, the simulation results are consistent with the blue-shift of the PL (2.05 eV to 2.37 eV) (Figure 4.1b and Figure 4.8a) as well as with the VEELS results.

4.5 Summary

In summary, the scenario of SPSC photochemical reactions can be explained as follows: Incident light, especially with NBE accumulates at the NRs tip, which is derived from an oxygen-deficient state. Then, water splitting process occurred by light irradiation. The light induces apical growth of a nanorod by the photochemical reaction of ZnO crystallization from zinc hydroxide ($Zn(OH)_2$) or the zincate ion ($Zn(OH)_4^{2-}$). At this time, polarization can be maintained between the positively charged Zn^{2+} ion and the alkaline environment rich with OH^- near the tip. The tapered NRs is then realized, and this feature is lost when a capped NRs is formed. The tip-edge of a tapered NR exhibited a double increase of electron energy absorption on NBE of ZnO. Hence, we can tune the NRs opto-electrical properties by controlling the tip morphology and intrinsic defects.

References

[1] J. A. Fan, C. Wu, K. Bao, J. Bao, R. Bardhan, N. J. Halas, V. N. Manoharan, P. Nordlander, G. Shvets, F. Capasso, Self-assembled plasmonic nanoparticle clusters. *Science* **328** (2010) 1135-1138.

[2] R. F. Oulton, V. J. Sorger, T. Zentgraf, R. M. Ma, C. Gladden, L. Dai, G. Bartal, X. Zhang, Plasmon lasers at deep subwavelength scale. *Nature* **461** (2009) 629-632.

[3] B. J. Lawrie, K. W. Kim, D. P. Norton, R. F. Haglund, Jr., Plasmon-exciton hybridization in ZnO quantum-well al nanodisc heterostructures. *Nano Letters* **12** (2012) 6152-6157.

[4] H. A. Atwater, A. Polman, Plasmonics for improved photovoltaic devices. *Nat Mater* **9** (2010) 205-213.

[5] M. W. Knight, H. Sobhani, P. Nordlander, N. J. Halas, Photodetection with active optical antennas. *Science* **332** (2011) 702-704.

[6] S. Shoaee, J. Briscoe, J. R. Durrant, S. Dunn, Acoustic enhancement of polymer/ZnO nanorod photovoltaic device performance. *Advanced Materials* **26** (2014) 263-268.

[7] X. W. Sun, J. Z. Huang, J. X. Wang, Z. Xu, A ZnO nanorod inorganic/organic heterostructure light-emitting diode emitting at 342 nm. *Nano Letters* **8** (2008) 1219-1223.

[8] K. S. Kim, H. Jeong, M. S. Jeong, G. Y. Jung, Polymer-templated hydrothermal growth of vertically aligned single-crystal ZnO nanorods and morphological transformations using structural polarity. *Advanced Functional Materials* **20** (2010) 3055-3063.

[9] J. Joo, B. Y. Chow, M. Prakash, E. S. Boyden, J. M. Jacobson, Face-selective electrostatic control of hydrothermal zinc oxide nanowire synthesis. *Nat Mater* **10** (2011) 596-601.

[10] J. Wei, N. Jiang, J. Xu, X. Bai, J. Liu, Strong coupling between ZnO excitons and localized surface plasmons of silver nanoparticles studied by STEM-EELS. *Nano Letters* **15** (2015) 5926-5931.

[11] A. P. Alivisatos, Semiconductor clusters, nanocrystals, and quantum dots. *Science* **271** (1996) 933-937.

[12] M. Jeem, M. R. M. bin Julaihi, J. Ishioka, S. Yatsu, K. Okamoto, T. Shibayama, T. Iwasaki, T. Kato, S. Watanabe, A pathway of nanocrystallite fabrication by photo-assisted growth in pure water. *Scientific Reports* **5** (2015) 11429.

[13] Y. Toriyabe, S. Watanabe, S. Yatsu, T. Shibayama, T. Mizuno, Controlled formation of metallic nanoballs during plasma electrolysis. *Applied Physics Letters* **91** (2007) 041501-041503.

[14] L. Xu, Y. Guo, Q. Liao, J. Zhang, D. Xu, Morphological control of ZnO nanostructures by electrodeposition. *The Journal of Physical Chemistry B* **109** (2005) 13519-13522.

[15] K. H. Tam, C. K. Cheung, Y. H. Leung, A. B. Djurišić, C. C. Ling, C. D. Beling, S. Fung, W. M. Kwok, W. K. Chan, D. L. Phillips, L. Ding, W. K. Ge, Defects in ZnO nanorods prepared by a hydrothermal method. *The Journal of Physical Chemistry B* **110** (2006) 20865-20871.

[16] M. Lucas, Z. L. Wang, E. Riedo, Combined polarized Raman and atomic force microscopy: In situ study of point defects and mechanical properties in individual ZnO nanobelts. *Applied Physics Letters*

95 (2009) 051904.

[17] Y. J. Kim, H. Shang, G. Cao, Growth and characterization of [001] ZnO nanorod array on ITO substrate with electric field assisted nucleation. *Journal of Sol-Gel Science and Technology* **38** (2006) 79-84.

[18] X. G. Zhang, Electrochemical thermodynamics and kinetics. In *Corrosion and electrochemistry of zinc*. (Springer US, Boston, MA, 1996), pp. 19-63.

[19] A. B. Djurisic, Y. H. Leung, K. H. Tam, Y. F. Hsu, L. Ding, W. K. Ge, Y. C. Zhong, K. S. Wong, W. K. Chan, H. L. Tam, K. W. Cheah, W. M. Kwok, D. L. Phillips, Defect emissions in ZnO nanostructures. *Nanotechnology* **18** (2007).

[20] S. K. Mishra, S. Srivastava, R. K. Srivastava, A. C. Panday, S. G. Prakash, Photoluminescence and ultraviolet photoresponse in ZnO nanophorsphors prepared by thermal decomposition of zinc acetate. *Advanced Materials Letters* **2** (2011) 298-302.

[21] Z. Q. Chen, S. Yamamoto, M. Maekawa, A. Kawasuso, X. L. Yuan, T. Sekiguchi, Postgrowth annealing of defects in ZnO studied by positron annihilation, x-ray diffraction, rutherford backscattering, cathodoluminescence, and hall measurements. *Journal of Applied Physics* **94** (2003) 4807-4812.

[22] N. Xu, Y. Cui, Z. Hu, W. Yu, J. Sun, N. Xu, J. Wu, Photoluminescence and low-threshold lasing of ZnO nanorod arrays. *Optics Express* **20** (2012) 14857-14863.

[23] X. Q. Wei, B. Y. Man, M. Liu, C. S. Xue, H. Z. Zhuang, C. Yang, Blue luminescent centers and microstructural evaluation by XPS and Raman in ZnO thin films annealed in vacuum, N_2 and O_2. *Physica B: Condensed Matter* **388** (2007) 145-152.

[24] R. F. Egerton, *Electron energy-loss spectroscopy in the electron microscope.* (Springer US, New York, 3 ed., 2011), pp. 491.

[25] Z. H. Zhang, X. Y. Qi, J. K. Han, X. F. Duan, Investigation on optical properties of ZnO nanowires by electron energy-loss spectroscopy. *Micron* **37** (2006) 229-233.

[26] M. Stoger-Pollach, H. Franco, P. Schattschneider, S. Lazar, B. Schaffer, W. Grogger, H. W. Zandbergen, Cerenkov losses: A limit for bandgap determination and Kramers-Kronig analysis. *Micron* **37** (2006) 396-402.

[27] M. Stöger-Pollach, Optical properties and bandgaps from low loss EELS: Pitfalls and solutions. *Micron* **39** (2008) 1092-1110.

[28] R. F. Egerton, Electron energy-loss spectroscopy in the TEM. *Reports on Progress in Physics* **72** (2009).

[29] M. Yiming, O. Hidefumi, I. Shuichi, Electronic structures and optical properties of ZnO, SnO_2 and In_2O_3. *Japanese Journal of Applied Physics* **38** (1999) 3453.

[30] A. Schleife, C. Rodl, F. Fuchs, J. Furthmuller, F. Bechstedt, Optical and energy-loss spectra of MgO, ZnO, and CdO from *ab initio* many-body calculationsw. *Physical Review B* **80** (2009).

[31] *Density functional theory of molecules, clusters, and solids.* D. E. Ellis Ed., (Springer Netherlands,

Dordrecht, 1 ed., 1995).

[32] M. D. Segall, J. D. L. Philip, M. J. Probert, C. J. Pickard, P. J. Hasnip, S. J. Clark, M. C. Payne, First-principles simulation: Ideas, illustrations and the CASTEP code. *Journal of Physics: Condensed Matter* **14** (2002) 2717.

CHAPTER 5

Summary

5.1 General conclusion

The work of this thesis focused on ZnO nanostructures fabrication, eventually on its nanorod morphology because of high research interest on the compound. It has a wide bandgap energy of 3.37 eV and high exciton binding energy of 60 meV. This properties promote ZnO for application in opto-electronic devices. A facile method to synthesis ZnO nanobumps, which is the crystal seeds is achieved through submerged liquid plasma technique. Then, inspired by photo-synthesis of green plants, submerged photo-synthesis of crystallites (SPSC) is introduced to grow ZnO nanorods under UV illumination in pure, neutral water.

In Chapter 2, I developed the understanding of submerged liquid plasma mechanism toward its effect to synthesis metallic nanoparticles as well as to a metallic electrode surface. In order to fabricate nanobumps on a Zn plate, a glow-discharge state must be optimized. In this case, applied voltage of 130 – 140 V and current of 1.9 – 2.0 A are necessary parameters to achieve this state.

In Chapter 3, the process and mechanism related to ZnO nanorods fabrication via SPSC is described. By using SPSC, ZnO nanorods (forming into nanoflowers and

dendrites can be obtained. Other than ZnO, SPSC technique also can be utilized to fabricate CuO nanoflowers, CeO_2 dendrites, and WO_3 nanorods. The growth process is photocatalytic, with hydroxyl radical via water splitting and hydrogen were detected. Nanobumps are essential for this photocatalytic process to occur. *Ab initio* calculation verified that a flat surface will yield 5.03 eV to dissociate H_2O molecule. In contrast, nanobump surface with curvature of R = 0.5 nm gives energy of 0.323 eV. By changing the type of dopants in additive solvents during SPSC; Si elements gives spherical shape, Ca elements gives whiskers-like shape, and NaCl gives hexagonal plate shape transformation of ZnO nanorods.

In Chapter 4, the apical characteristic of ZnO nanorods is systematically controlled. Tapered nanorods form into capped nanorods after continuous 72h UV irradiation. During this shape evolution, a blue shift in PL spectra was observed. This shift is due to oxygen vacancy defect changed to oxygen anti-site defect. STEM observation result revealed that local oxygen-deficient region exist at the tip-edge of a tapered nanorod. Through STEM-VEELS analysis done at the tip-edge, a double increase of Im(ε) on NBE of ZnO was observed. *Ab initio* simulation concluded that Zn 3*s* and Zn 3*p* orbitals are responsible for this increase.

5.2 Future outlook

While important steps have been made, as with all scientific research, many interesting, many opportunities were opened through the work performed in this thesis. In this section, some ideas based on observations seen throughout this research are introduced.

5.2.1 Cathodoluminescence analysis

The study of optical properties in ZnO nanorods in this work was performed by using PL and Raman spectroscopy analyses. Cathodoluminescence (CL) technique approach is necessary in order to analyze local oxygen-deficient region on the nanorods. Although STEM observation has confirmed the oxygen-deficient region at the tip-edge of tapered nanorod, there is still lack of knowledge about those defects on the local interior surface.

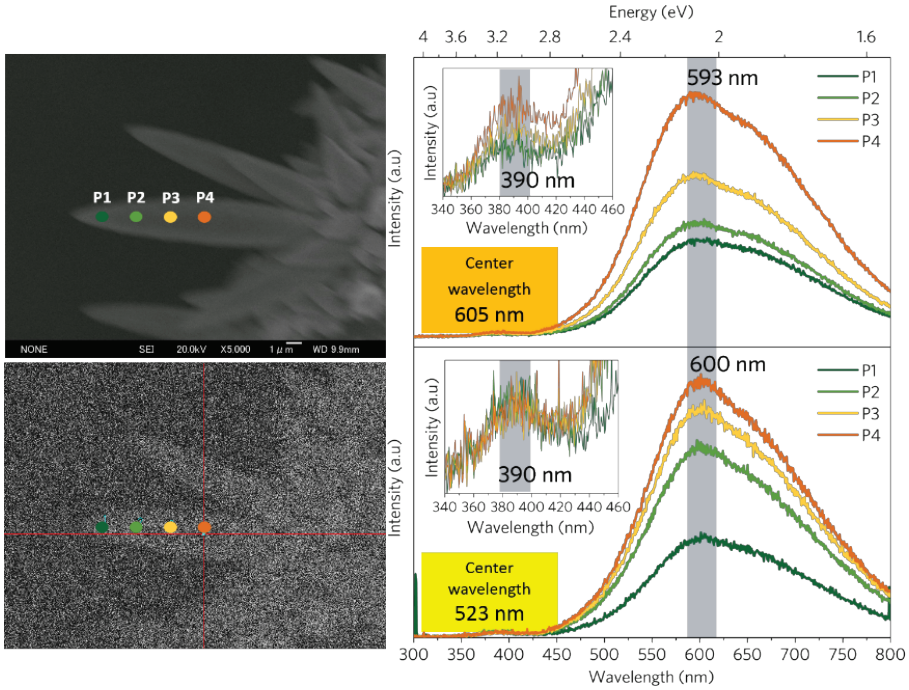

Figure 5.1 – Cathodoluminescence spectra obtained along vertical *c*-axis of a ZnO nanorod.

An example of CL spectra obtained on a ZnO nanorod is shown in Figure 5.1. On the basis of PL data, oxygen vacancy peak was at 605 nm while oxygen anti-site defect was at 523 nm. In order to match the data obtained from PL, 605 nm ($c.w_{605nm}$) and 523 ($c.w_{523nm}$) nm were set as center wavelength in the CCD camera, which has a broad wavelength detection range (200 – 1100 nm). Four data collection points (P1-P4) was placed starting from tip-edge to interior of the nanorod.

From P1-P4, a 390 nm (3.18 eV) peak, which corresponds to ZnO direct bandgap energy was observed on both wavelength centers. No peak shift was observed although there was a significant peak increase in $c.w._{605nm}$. In the visible light region, the spectra intensity significantly increased from P1-P4 on both wavelength centers. However, there

was no blue shift observed. A range of 593 - 600 nm is determined as defect driven peak, i.e. oxygen vacancy on the nanorod surface. For the purpose of CL blue shift observation in visible light region, the bulk nanorod with diameter ~2.5 μm was not adequately small for the CL system. In addition, the nanorod surface roughness indicated a considerable amount of zincate ions, e.g. $Zn(OH)_2$ on the lattice. Thus, together with nanorods array patterning in Figure 3.13, this issue shall be solved in order to develop their opto-electronic devices application.

5.2.2 Antimicrobial activity

All of the nanocrystallites fabrications using SPSC technique was implemented towards many metals; Zn, Cu, Mo, Ce, W, and Fe. In the case of ZnO, the target is to find its applications for opto-electronic devices. Other than that, insights in antimicrobial applications have given us motivation to develop the methods due to the fact that those oxides are non-toxic. Among the large family of metal oxides, cupric oxide (CuO) is an interesting multifunctional material because of its promising applications in magnetic storage media, solar energy transformations and catalysis. It is known that reactive oxygen species (ROS), e.g. O_2^-, OH radical, and H_2O_2 can cause disruptions to amino acid syntheses, resulting in bacterial death.[1, 2] Thus, by maintaining the same fashion of SPSC method, antibacterial experiments were conducted using CuO nanoflowers (section

3.4.7).[3] Types of bacteria are: Gram-positive (*Staphylococcus aureus*) bacteria and Gram-negative (*Escherichia coli* K12) bacteria. A raw Cu, CuO-plasma, CuO-annealed 700 °C, and CuO-SPSC specimens were prepared. For antimicrobial activity observation, the specimens were incubated with the bacteria inside a petri dish (Figure 5.2). The incubation was set at 37 °C for 24 hours under fluorescent light.

During incubation, a dark shallow ring will form around the specimens, indicating the bacterial growth inhibition zones. Larger inhibition zones translate to high antimicrobial activity. As indicated in Table 5.1, plasma-treated and SPSC-treated

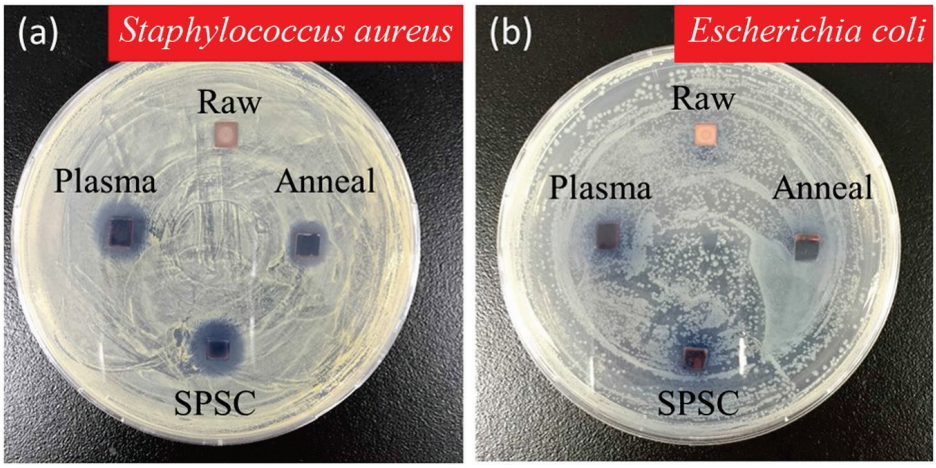

Figure 5.2 – Antibacterial activity test using Cu plates under varied treatments. (a) Gram-positive (*Staphylococcus aureus*) bacteria and (b) Gram-negative (*Escherichia coli* K12) bacteria. (Ref. 3)

specimens demonstrated higher antimicrobial activity. A black surface (CuO-plasma, CuO-annealed, and CuO-SPSC specimens) implies CuO, which could excite electron-hole pairs by mean of photosemiconductive reaction to generate Cu^{2+} through photocorrosion process ($CuO + H_2O + 2h^+ \rightarrow Cu^{2+} + 2OH$). Despite the same composition

Table 5.1 – Average inhibition zones for Cu specimens in *Staphylococcus aureus* and *Escherichia coli* K12 (Ref. 3).

	Average inhibition zones (cm)	
Specimens	*Staphylococcus aureus*	*Escherichia coli* K12
Raw Cu	0	0
CuO-plasma	1.2	1.1
CuO-annealed 700 °C	1.0	1.0
CuO-SPSC	1.2	1.1

of CuO, the CuO-plasma and CuO-SPSC demonstrated higher antimicrobial activity than CuO-annealed on the basis of their inhibition zones (Table 5.1). This is due to high specific surface area owned by the former.[3] Higher specific surface area will enhance DNA damage following the reactions below:[4]

$$Cu^{2+} + 2e^{-} + O_2 \rightarrow Cu^{+} + O_2^{-} \quad (5.1)$$

$$2O_2^{-} + 2H_2O \rightarrow H_2O_2 + O_2 + 2OH^{-} \quad (5.2)$$

$$Cu^{+} + H_2O_2 \rightarrow Cu^{2+} + OH^{-} + OH \quad (5.3)$$

$$OH + \text{DNA} \rightarrow \text{DNA damage} \quad (5.4)$$

In summary, the CuO-SPSC exhibited significant high antimicrobial activity. This result represented the future outlook antimicrobial application using ZnO as well as other

metallic oxide crystallites.

5.3 Final remarks

Overall, the concept of submerged photo-synthesis of crystallite has been covered in this thesis (Figure 5.3). Though there is still more to explore for its applications in

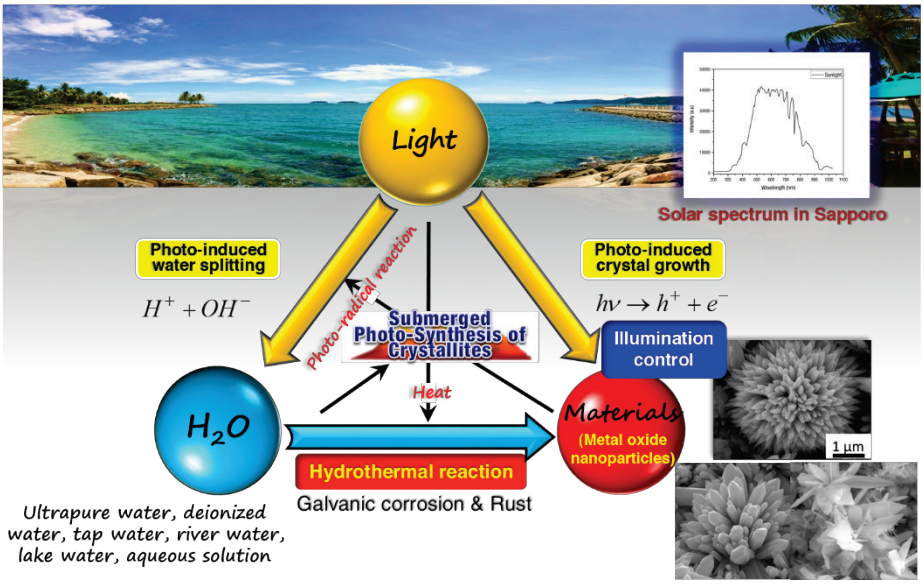

Figure 5.3 – SPSC concept.

semiconductor technology, incorporation of scientific advances to open new perspectives in understanding light interaction with matter has been done. An important point learned from this work is that even well-known materials, if they are applied in in different way, can result in exciting breakthroughs.

Reference

[1] N. Ekthammathat, T. Thongtem, S. Thongtem, Antimicrobial activities of CuO films deposited on Cu foils by solution chemistry. *Applied Surface Science* **277** (2013) 211-217.

[2] G. Applerot, J. Lellouche, A. Lipovsky, Y. Nitzan, R. Lubart, A. Gedanken, E. Banin, Understanding the antibacterial mechanism of CuO nanoparticles: Revealing the route of induced oxidative stress. *Small* **8** (2012) 3326-3337.

[3] F. Nishino, M. Jeem, L. Zhang, K. Okamoto, S. Okabe, S. Watanabe, Formation of CuO nano-flowered surfaces via submerged photo-synthesis of crystallites and their antimicrobial activity. *Scientific Reports* **7** (2017) 1063.

[4] O. Bondarenko, A. Ivask, A. Käkinen, A. Kahru, Sub-toxic effects of CuO nanoparticles on bacteria: Kinetics, role of Cu ions and possible mechanisms of action. *Environmental Pollution* **169** (2012) 81-89.

List of publications

[1] M. Jeem, L. Zhang, J. Ishioka, T. Shibayama, T. Iwasaki, T. Kato, S. Watanabe, Tuning optoelectrical properties of ZnO nanorods with excitonic defects via submerged illumination. *Nano Letters* 17 (**2017**) 2088-2093.

[2] M. Jeem, M. R. M. bin Julaihi, J. Ishioka, S. Yatsu, K. Okamoto, T. Shibayama, T. Iwasaki, T. Kato, S. Watanabe, A pathway of nanocrystallite fabrication by photo-assisted growth in pure water. *Scientific Reports* 5 (**2015**) 11429.

[3] F. Nishino, M. Jeem, L. Zhang, K. Okamoto, S. Okabe, S. Watanabe, Formation of CuO nano-flowered surfaces via submerged photo-synthesis of crystallites and their antimicrobial activity. *Scientific Reports* 7 (**2017**) 1063.

[4] J. Ishioka, K. Kogure, K. Ofuji, K. Kawaguchi, M. Jeem, T. Kato, T. Shibayama, S. Watanabe, In situ direct observation of photocorrosion in ZnO crystals in ionic liquid using a laser-equipped high-voltage electron microscope. *AIP Advances* 7 (**2017**) 035220.

Others

[1] M. R. M. b. Julaihi, S. Yatsu, M. Jeem, S. Watanabe, Synthesis of stainless steel nanoballs via submerged glow-discharge plasma and its photocatalytic performance in methylene blue decomposition. *Journal of Experimental Nanoscience* 10 (**2014**) 965-

982.

ACKNOWLEDGEMENT

First and foremost, I would like to thank my advisor, Professor Seiichi Watanabe, for taking a chance on me, and supporting me over the last five years. Professor Watanabe has managed to create a research group which does cutting edge research, while maintaining an enjoyable collaborative environment. I never once dreaded heading to work. Without his constant positive attitude and support, completing this dissertation would not have been possible.

Additionally, I would like to thank the rest of my dissertation committee, including Professor Tamaki Shibayama and Professor Mikito Ueda for their diligent support and constant follow up regarding my research. I am thankful to Associate Professor Noriyuki Okinaka for his positive comments in my work and the enjoyable working environment. I also thank secretary Ms. Kaori Mitomo and Ms. Mariko Kondo for their attention and care regarding office matters. Before starting my thesis work, my knowledge of materials was minimal, but by collaborating with Assistance Professor Shigeo Yatsu and Dr. Muhammad Rafiq Mirza, I was able to learn incredible amount of skills and knowledge.

I am thankful to Dr. Lihua Zhang for her untiring efforts collaborating in the same field of work, especially in the pH-T measurement. I am grateful to Dr. Junya Ishioka, Mr.

Kenji Ohkubo, and Mr. Ryo Ohta for sharing of their expertise regarding microstructural analysis using the TEM. I am thankful to Professor Norihiko Sakaguchi and Dr. Genki Saito for their professional opinions and discussion in STEM-VEELS analysis. For OH radical and gas analyses, I want to dedicate special thanks to Assistance Professor Kazumasa Okamoto and Mr. Yukiyasu Yamakoshi for their genuine participation in idea contributions and technical assistance.

A big part of thesis work was done through collaboration with Hitachi Research Laboratory group; Dr. Takahiko Kato and Dr. Tomio Iwasaki. I am truly grateful for Dr. Takahiko Kato's assistance in XRD measurement, motivation and comments in doing my experiments. Though I have never met him in person, I have to give high credits to Dr. Tomio Iwasaki for his help in conducting *ab initio* calculation and invaluable follow-up comments. I am also thankful to fellow mature doctoral student, Mr. Shuichiro Adachi of Hitachi Chemical for his support in providing materials for our collaborative research.

I am thankful to Mr. Keita Suzuki for his guidance in using the XPS machine, Mr. Mori of Engineering Workshop to help in cutting the electrodes, Professor Junichi Kaneko and Mr. Takanori Hanada for the support in cathodoluminescence measurement.

Realization of the thesis would not be possible in the absence of help from HVEM staffs, members of the Laboratory of Quantum Energy Conversion Materials and

Laboratory of Photon and Thermal Energy Conversion Materials. Dr. Ruixuan Yu, Fumika Nishino, Kana Yamada, Dai Takai, Shoichi Takei, Chuchen Duan, Shuntaro Murakami, Yuki Takahashi, Yu Tanase, Tomoya Goto, Junichi Mizuno, Kento Hiraiwa, Takuya Moriyama, and Atsuki Toda have provided me a good, calm, and enjoyable working environment.

I am grateful with the financial aids from Monbukagakusho Honors Scholarship (Gakushu-shorei-hi) and Mitsubishi UFJ Trust Scholarship Foundation. The work was supported by the “Nanotechnology Platform” from the Ministry of Education, Culture, Sports, and Technology (MEXT).

Finally, I would like to extend my highest gratitude to my parents for keep believing in me and my close Malaysian friends in Sapporo.

Above all, I owe it all to Almighty God for granting me the wisdom, health, and strength to undertake this research task and enabling me to its completion. Words cannot truly express my gratitude.